# Unified Position Sensorless Solution with Wide Speed Range Capabilities for IPM Synchronous Motor Drives

# UNIFIED POSITION SENSORLESS SOLUTION WITH WIDE SPEED RANGE CAPABILITIES FOR IPM SYNCHRONOUS MOTOR DRIVES

BY

YINGGUANG SUN, B.Sc., M.Sc.

A THESIS

SUBMITTED TO THE DEPARTMENT OF ELECTRICAL & COMPUTER ENGINEERING

AND THE SCHOOL OF GRADUATE STUDIES

OF MCMASTER UNIVERSITY

IN PARTIAL FULFILMENT OF THE REQUIREMENTS

FOR THE DEGREE OF

DOCTOR OF PHILOSOPHY

Doctor of Philosophy (2016) McMaster University

(Electrical & Computer Engineering) Hamilton, Ontario, Canada

| | |
|---|---|
| TITLE: | Unified Position Sensorless Solution with Wide Speed Range Capabilities for IPM Synchronous Motor Drives |
| AUTHOR: | Yingguang Sun<br>M.Sc. in Electrical Engineering<br>Illinois Institute of Technology, Chicago, US<br>B.Sc. in Electrical Engineering<br>Hebei University of Technology, Tianjin, China |
| SUPERVISOR: | Dr. Ali Emadi, Fellow IEEE,<br>Canada Excellence Research Chair in Hybrid Powertrain<br>Director, McMaster Institute for Automotive Research and Technology (MacAUTO), McMaster University |
| CO-SUPERVISOR: | Dr. Shahin Sirouspour, Professor, Department of Electrical and Computer Engineering, McMaster University |
| NUMBER OF PAGES: | xxiv, 167 |

*To My Father, Qi Sun,*

*My Mother, Li Zhao,*

*My Wife, Xiaoying Wang.*

# Abstract

This thesis presents a unified nonlinear optimization based speed and position estimation method in position sensorless control of interior permanent magnet synchronous motor (IPMSM) drives at wide speed range including standstill.

The existing electromotive force (EMF) based sensorless methods are suitable for medium and high speed operation, but they can't be applied at low speed and standstill condition due to the reduced EMF values. The conventional saliency tracking based sensorless methods usually employ the continuous voltage or current injection at low speed including standstill condition. However, these methods degrade at high speed by introducing higher loss and torque ripples caused by the injection. Additionally, the initial rotor position needs to be detected at the machine startup to avoid the reverse rotation and to guarantee the delivery of the expected torque. Therefore, different position estimation techniques need to be combined in the controller at wide speed range, which increases the control system complexity.

Hence, a unified nonlinear optimization based speed and position estimation method is proposed. At startup and standstill conditions, three steps are employed for initial position estimation. Step I employs pulse voltage injection in the stationary reference frame and a cost function which contains the knowledge of initial rotor position. The rotor position can be estimated by minimizing the cost function with injected voltage

and induced current. Since the estimation results in Step I have an ambiguity of 180°, a generalized approach to magnetic polarity detection which exploits asymmetries in machine specific differential inductance profiles is employed as Step II. In order to improve the estimation accuracy, continuous sinusoidal voltage is injected in estimated rotor reference frame in Step III. A modified cost function is minimized based on the injected voltage and resulting current. At running state, cost functions which employ both speed and position as decision variables are proposed and utilized for estimation. The speed and position estimation can be delivered by minimizing the proposed cost functions based on the measurements of the stator voltage and current. Since only one position estimator exists in the drive system, the speed and position estimation is unified at wide speed range. The feasibility of the proposed estimation algorithms is validated with the prototype 5 KW IPMSM drives test bench.

In order to benchmark the proposed estimation method, the performance of the proposed method was compared with existing sensorless control methods on the same prototype IPMSM drives test bench. Under the same test conditions, the proposed method outperforms with improved transient performance and steady state accuracy. Moreover, the proposed method is capable of delivering estimation with different voltage injection types and involving the nonlinear motor parameters, which makes this method more flexible in practice. Additionally, the capability of estimating speed and position with low sampling frequency also makes the application of the proposed method promising in high power AC motor drive systems.

# Acknowledgements

First of all, I would like to express my sincere gratitude to my supervisor, Dr. Ali Emadi for offering me an opportunity to work in a research group with so many brilliant people who have super enthusiasm in providing new knowledge to the electrical engineering industry. It is him who make it possible for me to be involved in many high level industrial projects which help me grow up as an electrical engineer and a researcher. Thanks for all his guidance, suggestion and encouragement.

I am also indebted to Dr. Shahin Sirouspour, who co-supervised my Ph.D. work during the past three years. He gave me numerous insights when I was not clear about the research direction at the beginning of my Ph.D. His cautious attitude towards study and research will be the criterion for me to evaluate my research and work in the future.

I would like to express my appreciation to Dr. Matthias Preindl as well. To me, he is like a teacher as well as a good friend. I will never forget the time we spent together in developing new ideas and solutions to the problems I encountered. Thanks for all his patience, suggestions and support.

I also would like to express my gratitude to Dr. Babak Nahid-Mobarakeh and Dr. Mohamed Bakr for being my supervisory committee. Thanks for all the suggestions they gave me during the committee meetings.

Moreover, this research was undertaken, in part, thanks to funding from the Canada Excellence Research Chairs Program.

I am also grateful to my friends and lab colleagues, Jing Guo, Ran Gu, Michael Eull, Berker Bilgin, Fei Peng, Deqiang Wang, Weisheng (James) Jiang, Hao Ge, Yu Miao, Shamsuddeen Nalakath, Alan Callegaro, Ben Danen, Michael Kasprzak and Romina Rodriguez, etc. I will never forget the great time I spent with them. I sincerely hope they will obtain great achievements in their future career.

I am at the dearth of words to express my gratitude and love to my parents for their endless support and generous love in the past 28 years. I feel sorry for not being with them for the past a few years. The have sacrificed so much in order to support my study. Without their selfless love and support, I will never achieve what I have.

At last, I want to show my deepest love to my wife, Xiaoying Wang. We knew each other when I came to Canada three years ago and she has been always accompanied with me since then. It is her endless love that encourages me to overcome any difficulty I met in my life. Thanks for supporting me unconditionally and I will always love her with all my heart.

# Notation and abbreviations

| | |
|---|---|
| $d$-$q$ frame | Rotor reference frame |
| $\alpha$-$\beta$ frame | Stationary reference frame |
| $\delta$-$\gamma$ frame | Estimated rotor reference frame |
| $\theta$ | Rotor position |
| $\hat{\theta}$ | Estimated rotor position |
| $\tilde{\theta}$ | Position estimation error |
| $u_{abc}$ | Three-phase voltages |
| $u_{dq}$ | Voltages in rotor reference frame |
| $u_{\alpha\beta}$ | Voltages in stationary reference frame |
| $u_{\delta\gamma}$ | Voltages in estimated rotor reference frame |
| $i_{abc}$ | Three-phase currents |
| $i_{dq}$ | Currents in rotor reference frame |
| $i_{\alpha\beta}$ | Currents in stationary reference frame |
| $i_{\delta\gamma}$ | Currents in estimated rotor reference frame |
| $\lambda_{dq}$ | Flux linkages in rotor reference frame |
| $\lambda_{pm}$ | Permanent magnet flux linkage |
| $R_s$ | Phase resistance |
| $\omega_e$ | Synchronous speed |

| | |
|---|---|
| $\hat{\omega}_e$ | Estimated synchronous speed |
| $L_{dq}$ | Inductances in rotor reference frame |
| $\ell_{dd}\big(i_{dq}(t)\big)$ | $d$ axis differential self-inductance profile |
| $\ell_{qq}\big(i_{dq}(t)\big)$ | $q$ axis differential self-inductance profile |
| $\ell_{dq}\big(i_{dq}(t)\big)$ | $d$ axis differential cross-coupling inductance profile |
| $\ell_{qd}\big(i_{dq}(t)\big)$ | $q$ axis differential cross-coupling inductance profile |
| $C_{\alpha\beta}$ | Clark transformation |
| $T_{dq}$ | Park transformation |
| $T_e$ | Electromagnetic torque |
| $p$ | Differential operator |
| $P$ | Number of pole pairs |
| $V_{dc}$ | DC linkage voltage |
| $E_{ext}$ | Extended EMF |
| $e_{\delta\gamma}$ | Extended EMFs in estimated rotor reference frame |
| $L_{\delta}^{diff}$ | Calculated differential inductance |
| $G_i$ | Cost function used in Step I |
| $G_l$ | Cost function used in Step III and low speed |
| $G_r$ | Cost function used for medium and high speed |
| $J$ | Partial derivative of the cost function |
| $H$ | Hessian of the cost function |
| IPMSM | Interior Permanent Magnet Synchronous Machine |
| IPM | Interior Permanent Magnet |
| PMSM | Permanent Magnet Synchronous Machine |
| FOC | Field Oriented Control |

| | |
|---|---|
| DTC | Direct Torque Control |
| EMF | Electromotive Force |
| DC | Direct Current |
| AC | Alternating Current |
| VSI | Voltage Source Inverter |
| IGBT | Insulated Gate Bipolar Transistor |
| MOSFET | Metal-Oxide-Semiconductor-Field Effect Transistor |
| PLL | Phase Locked Loop |
| MTPA | Maximum Torque-per-ampere |
| PWM | Pulse Width Modulation |
| SPWM | Sinusoidal Pulse Width Modulation |
| SVPWM | Space Vector Pulse Width Modulation |
| LPF | Low-pass Filter |
| BPF | Band-pass Filter |
| LUT | Look-up Table |
| UNOP | Unified Nonlinear Optimization Based Method |
| PSVI | Pulsating Sinusoidal Voltage Injection Based Method |
| EEMF | Extended EMF Based Method |

# Contents

**Abstract** **iv**

**Acknowledgements** **vi**

**Notation and abbreviations** **viii**

**1 Introduction** **1**

1.1 Motivation . . . . . 1

1.2 Contributions . . . . . 5

1.3 Outline of the Thesis . . . . . 6

**2 Interior Permanent Magnet Synchronous Motor Drives and Control** **10**

2.1 Introduction . . . . . 10

2.2 Fundamentals of Interior Permanent Magnet Synchronous Motor . . . 11

2.2.1 Stator Voltage Equations . . . . . 11

2.2.2 Flux, Inductance and Torque . . . . . 14

2.3 Inverter Control and Pulse Width Modulation . . . . . 16

2.4 Position Sensors and Interface . . . . . 23

2.4.1 Resolver and Its Interface . . . . . 23

2.4.2 Encoder and Its Interface . . . . . 26
2.5 Control of Interior Permanent Magnet Synchronous Motor . . . . . 30
2.6 Conclusions . . . . . 34

**3 Existing Sensorless Control Methods of IPM Motor Drives 36**
3.1 Introduction . . . . . 36
3.2 EMF Based Speed and Position Estimation . . . . . 37
3.3 Saliency Tracking Based Speed and Position Estimation . . . . . 42
3.4 Speed and Position Estimation at Wide Speed Range . . . . . 46
3.5 Initial Position Estimation . . . . . 49
3.5.1 Short Pulse Voltage Injection for Initial Position Estimation . 50
3.5.2 Magnetic Polarity Detection . . . . . 53
3.6 Conclusions . . . . . 54

**4 Novel Nonlinear IPM Motor Model 57**
4.1 Introduction . . . . . 57
4.2 Novel Nonlinear Model of the Prototype IPM Motor . . . . . 58
4.2.1 Nonlinear Flux Linkage and Inductance Profiles . . . . . 58
4.2.2 Measurements of the Nonlinear Look-up Tables . . . . . 60
4.2.3 Nonlinear IPM Motor Model with Inverted LUTs . . . . . 61
4.3 Experimental Test Bench of Prototype IPM Motor Drives . . . . . 65
4.3.1 Silicon Carbide MOSFET Inverter . . . . . 66
4.3.2 MicroAutoBox II . . . . . 67
4.3.3 Dyno Machine Controller . . . . . 68
4.3.4 High Accuracy Position Sensor . . . . . 69

4.4 Conclusions . . . . . 70

**5 Proposed Nonlinear Optimization Based Initial Position Estimation at Startup and Standstill 71**

5.1 Introduction . . . . . 71

5.2 Pulse Voltage Injection for Position Estimation . . . . . 73

5.3 Generalized Polarity Detection Method . . . . . 78

5.4 Continuous Sinusoidal Voltage Injection for Position Estimation . . . 83

5.5 Simulation Verifications . . . . . 85

5.6 Experimental Verifications . . . . . 88

5.6.1 Experimental Results on Initial Position Estimation . . . . . 88

5.6.2 Accuracy Comparison Between Pulse Voltage Injection and Continuous Sinusoidal Injection . . . . . 92

5.7 Conclusions . . . . . 92

**6 Proposed Nonlinear Optimization Based Speed and Position Estimation at Running State 94**

6.1 Introduction . . . . . 94

6.2 Optimization Based Sensorless Algorithm for Medium and High Speed Operation . . . . . 96

6.3 Modification of the Cost Function at Low Speed Operation . . . . . 99

6.4 Variable Magnitudes Sinusoidal Voltage Injection . . . . . 101

6.5 Observer Implementation . . . . . 104

6.6 Experimental Verifications . . . . . 106

6.7 Parameter Sensitivity Analysis . . . . . 114

6.8 Conclusions . . . . . 118

**7 Comparative Assessment of the Proposed Sensorless Approach 119**

7.1 Introduction . . . . . 119

7.2 Improvements in Initial Position Estimation . . . . . 120

7.2.1 Dynamic Performance in Initial Position Estimation . . . . . 121

7.2.2 Magnetic Polarity Detection . . . . . 122

7.2.3 Involvement of Machine Nonlinearity in Initial Position Estimation . . . . . 124

7.3 Improvements in Speed and Position Estimation at Running State . . 127

7.3.1 Dynamic Performance at Low Speed . . . . . 127

7.3.2 Dynamic Performance at High Speed . . . . . 132

7.3.3 Switch Between Low Speed and High Speed . . . . . 137

7.4 Capability of Speed and Position Estimation with Multiple Injection Types . . . . . 140

7.5 Capability of Speed and Position Estimation with Low Sampling Frequency . . . . . 142

7.6 Computational Burden Analysis . . . . . 146

7.7 Conclusions . . . . . 149

**8 Conclusions and Future Work 150**

8.1 Conclusions . . . . . 150

8.2 Future Work Suggested . . . . . 152

8.3 Publications . . . . . 153

8.3.1 Journal Papers . . . . . 153

8.3.2 Conference Papers . . . . . 154

# List of Figures


1.1 The modern electric motor drive system. . . . . 3

2.1 Clark and Park Transformations. . . . . 12

2.2 Different rotor configurations of PMSM machines. . . . . 14

2.3 The *d*-*q* axes flux paths in PMSMs. . . . . 15

2.4 Voltage Source Inverter. . . . . 17

2.5 Sinusoidal pulse width modulation. . . . . 18

2.6 Voltage vectors in SVPWM . . . . . 19

2.7 Switching pattern in Sector I. . . . . 21

2.8 Comparison between SPWM and SVPWM. . . . . 22

2.9 Resolver and its interface. . . . . 24

2.10 Variable reluctance resolver. . . . . 25

2.11 Speed and position extraction from the resolver interface. . . . . 26

2.12 BEI incremental encoder. . . . . 27

2.13 Absolute and incremental encoders. . . . . 28

2.14 Quadrature output in incremental encoder. . . . . 29

2.15 The working theory of the incremental encoder interface. . . . . 30

2.16 Block diagram of the FOC in IPM motor drives. . . . . 31

2.17 Optimal IPM motor operation with voltage and current limits and torque-speed curve. . . . . 32
3.1 Different reference frames in IPMSM drives. . . . . 38
3.2 State observer for extended EMF in $\delta$ axis. . . . . 40
3.3 Extended EMF based position estimator. . . . . 42
3.4 Demodulation based position estimator. . . . . 46
3.5 Linear blending algorithm for speed and position combination. . . . . 48
3.6 Block diagram of the sensorless control system with combined algorithms. 48
3.7 Applied voltage vectors for initial position estimation. . . . . 51
3.8 Dual voltage injection based method for magnetic polarity detection. 55
3.9 Framework of the dual voltage pulse injection based method . . . . . 55
4.1 Experimental measured $d$ axis flux linkage profile $\lambda_d(i_{dq})$ under different $i_d$ and $i_q$. . . . . 61
4.2 Experimental measured $q$ axis flux linkage profile $\lambda_q(i_{dq})$ under different $i_d$ and $i_q$. . . . . 62
4.3 Flowchart of look-up table inversion algorithm . . . . . 63
4.4 Inverted look-up tables: (a) The inverted profile $i_d(\lambda_{dq})$; (b) The inverted profile $i_q(\lambda_{dq})$. . . . . 64
4.5 Block diagram of the nonlinear machine model dynamics with inverse LUTs. . . . . 65
4.6 Prototype IPMSM drives test bench. . . . . 66
4.7 Prototype SiC MOSFET inverter. . . . . 67
4.8 RTI Blockset in Simulink. . . . . 68
4.9 Experimental software ControlDesk Next Generation. . . . . 69

5.1 Block diagram of the proposed optimization based initial position estimator. . . . . 72
5.2 Screenshot of the scope, voltage injection procedures in initial position estimation. . . . . 73
5.3 Voltage vectors applied for injection in Step I. . . . . 75
5.4 Injected voltages and resulting currents in $\alpha$-$\beta$ axes. . . . . 75
5.5 Plot of $G_i(\hat{\theta})$ versus position estimation errors at different initial positions for $m = 1$ based on experimental data. . . . . 77
5.6 Experimental obtained $d$ axis differential inductance profile $\ell_{dd}(i_d, 0)$. 79
5.7 Injected voltages and resulting currents in $\delta$ axis for magnetic polarity detection. . . . . 80
5.8 Framework of the proposed polarity detection method. . . . . 81
5.9 Contour plot of the cost function (5.9) at standstill condition. . . . . 84
5.10 Simulation results on initial position estimation at 41.5°: (a) actual and estimated positions; (b) position estimation error; (c) $c_1$ and $c_2$ in polarity detection. . . . . 86
5.11 Simulation results on initial position estimation at 250°: (a) actual and estimated positions; (b) position estimation error; (c) $c_1$ and $c_2$ in polarity detection. . . . . 87
5.12 Simulation results on integration of speed and position estimation at standstill and low speed: (a) actual and estimated positions; (b) position estimation error; (c) actual and estimated speeds. . . . . 88

5.13 Experimental results on initial position estimation at 41.5°: (a) measured and estimated positions; (b) position estimation error; (c) $c_1$ and $c_2$ in polarity detection. . . . . 89
5.14 Experimental results on initial position estimation at 250°: (a) measured and estimated positions; (b) position estimation error; (c) $c_1$ and $c_2$ in polarity detection. . . . . 90
5.15 Experimental results on integration of speed and position estimation at standstill and running state: (a) measured and estimated positions; (b) position estimation error; (c) measured and estimated speeds. . . 91
5.16 Experimental results, position estimation errors of pulse voltage injection and continuous sinusoidal voltage injection. . . . . 92
6.1 Block diagram of the proposed nonlinear optimization based sensorless control system. . . . . 95
6.2 Contour plots of the cost function (6.4): (a) 400 rpm and $i_{phase}^{peak} = 0$; (b) 400 rpm and $i_{phase}^{peak} = 4$; (c) 800 rpm and $i_{phase}^{peak} = 0$. . . . . 98
6.3 Convex region of the cost function at 400 rpm: (a) convex regions on the contour plot; (b) zoomed in convex region around the expected local minimum. . . . . 100
6.4 Convex region of the cost function at 800 rpm: (a) convex regions on the contour plot; (b) zoomed in convex region around the expected local minimum. . . . . 100
6.5 Contour plots of the cost function: (a) cost function $G_r$ at 0 rpm without injection; (b) cost function $G_l$ at 0 rpm with injection. . . . . 102

6.6 Contour plots of the cost function: (a) cost function $G_r$ at 50 rpm without injection; (b) cost function $G_l$ at 50 rpm with injection. . . . 102
6.7 Convex regions of the modified cost function $G_l$: (a) convex region at 0 rpm; (b) convex region at 50 rpm. . . . . 103
6.8 Variable magnitudes voltage injection scheme. . . . . 104
6.9 Nonlinear optimization based position estimator. . . . . 105
6.10 Experimental results, convergence tests at standstill condition: (a) positive initial error; (b) negative initial error. . . . . 106
6.11 Experimental results, speed and position estimation before and after PLL: (a) position estimation at transients; (b) speed estimation. . . . 107
6.12 Experimental results, speed step change without load, 50 rpm: (a) position estimation error; (b) position estimation at transients; (c) speed estimation. . . . . 109
6.13 Experimental results, speed step change with 20% rated torque, 50 rpm: (a) position estimation error; (b) position estimation at transients; (c) speed estimation . . . . . 110
6.14 Experimental results, speed step change with 40% rated torque, 50 rpm: (a) position estimation error; (b) position estimation at transients; (c) speed estimation . . . . . 111
6.15 Experimental results, speed step change with 40% rated torque, 100 rpm: (a) position estimation error; (b) current in $\gamma$ axis; (c) position estimation at transients; (d) speed estimation. . . . . 112

6.16 Experimental results, torque step change at constant speed, 300 rpm: (a) position estimation error; (b) current in $\gamma$ axis; (c) position estimation at transients; (d) speed estimation. . . . . 113
6.17 Experimental results, wide speed range operation: (a) position estimation error; (b) speed estimation. . . . . 114
6.18 Experimental results, speed and position estimation at wide speed range including standstill: (a) position estimation error; (b) position estimation at transients; (c) current in $\gamma$ axis; (d) speed estimation. . 115
6.19 Parameter sensitivity contour plot analysis at 300 rpm with 40% rated torque: (a) 50% resistance variation; (b) 50% permanent magnet flux variation; (c) 50% *d*-*q* axes inductances variation. . . . . 116
6.20 Parameter sensitivity experimental test results: (a) ±50% resistance variation; (b) ±50% PM flux variation; (c) ±50% *d*-*q* axes inductances variation. . . . . 117
7.1 The modified PLL used in PSVI and EEMF methods. . . . . 120
7.2 Experimental comparison on convergence speed between PSVI method and UNOP method. . . . . 121
7.3 Experimental comparison on torque transient performance between PSVI method and UNOP method: (a) 20% rated torque change; (b) 40% rated torque change. . . . . 122
7.4 Resulting $\delta$ axis currents due to the injection in magnetic polarity detection. . . . . 123
7.5 Plot of $\bar{G}_i(\hat{\theta})$ versus position estimation errors at different initial positions for $m = 1$ using experimental data. . . . . 124

7.6 Position estimation errors of the linear method at different initial positions with different injection durations. . . . . 126
7.7 Position estimation errors of the nonlinear method at different initial positions with different injection durations. . . . . 127
7.8 Estimation accuracy comparison between nonlinear and linear methods ($5T_s$ for each voltage pulse). . . . . 128
7.9 Benchmark reference, speed and position estimation with PSVI method with the same test shown in Figure 6.14: (a) position estimation error; (b) position estimation at transients; (c) speed estimation. . . . . 129
7.10 Experimental results of the UNOP method at low speed, torque step change at 100 rpm: (a) position estimation error; (b) position estimation at transients; (c) current in $\gamma$ axis (d) speed estimation. . . . . 130
7.11 Benchmark reference, PSVI base method at low speed, torque step change at 100 rpm: (a) position estimation error; (b) position estimation at transients; (c) current in $\gamma$ axis; (d) speed estimation. . . . . 131
7.12 Benchmark reference, EEMF base method at high speed, speed step change with 15% rated torque: (a) position estimation error; (b) position estimation at transients; (c) current in $\gamma$ axis; (d) speed estimation. 133
7.13 Experimental results of the UNOP method at high speed, speed step change with 15% of rated torque: (a) position estimation error; (b) position estimation at transients; (c) current in $\gamma$ axis; (d) speed estimation. . . . . 134

7.14 Benchmark reference, EEMF base method at high speed, torque step change at 400 rpm: (a) position estimation error; (b) position estimation at transients; (c) current in $\gamma$ axis; (d) speed estimation. . . . . 135
7.15 Experimental results of the UNOP method at high speed, torque step change at 400 rpm: (a) position estimation error; (b) position estimation at transients; (c) current in $\gamma$ axis; (d) speed estimation. . . . . 136
7.16 Benchmark reference, the combined method during switch process, speed step change without load: (a) position estimation error; (b) position estimation at transients; (c) speed estimation. . . . . 137
7.17 Experimental results of the proposed unified method during switch process, speed step change without load: (a) position estimation error; (b) position estimation at transients; (c) speed estimation. . . . . 138
7.18 Benchmark reference, the combined method during switch process, speed step change with 30% rated torque: (a) position estimation error; (b) current in $\gamma$ axis; (c) speed estimation. . . . . 139
7.19 Experimental results of the proposed unified method during switch process, speed step change with 30% rated torque: (a) position estimation error; (b) current in $\gamma$ axis; (c) speed estimation. . . . . 140
7.20 Screenshot of the scope, continuous rectangular voltage injection in Step III. . . . . 141
7.21 Experimental results on initial position estimation at 41.5° with rectangular voltage injection: (a) measured and estimated positions; (b) position estimation error. . . . . 142

7.22 Experimental results, speed and position estimation with continuous rectangular voltage injection: (a) position estimation error; (b) position estimation at transients; (c) current in $\gamma$ axis; (d) speed estimation. 143
7.23 Experimental results, speed and position estimation with 2 KHz sampling frequency, no load: (a) position estimation error; (b) position estimation at transients; (c) speed estimation. . . . . 144
7.24 Experimental results, speed and position estimation with 2 KHz sampling frequency, with 40% rated torque: (a) position estimation error; (b) position estimation at transients; (c) speed estimation. . . . . 145
7.25 Estimation performance validation with different iterations, convergence test with 30° initial error. . . . . 147
7.26 Estimation performance validation with different iterations: (a) speed transients; (b) torque transients. . . . . 148
7.27 Sensorless methods comparison. . . . . 148

# Chapter 1

# Introduction

## 1.1 Motivation

The electric machines have been widely used in pumps, fans, aerospace actuators, robotic actuators and automobile industries. According to the United States Industrial Electric Motor Systems Market Opportunities Assessment published in 1998, the industrial electric motor systems were the largest single electrical end use in US economy, which consumed 679 billion kWh power and occupied roughly 23% of all electricity sold in the United States in 1994 (XENERGY, 1998). Since then the rapid development of the electric motor systems has been sustained in recent 20 years and they are currently the single largest electrical end use which accounts for 43% to 46% of the global electricity consumption (Waide and Brunner, 2011).

The electric machine can be classified into direct current (DC) machines and alternating current (AC) machines according to the machine input. Compared with DC machines, AC machines are more commonly employed due to their simplicity and higher efficiency. The AC machines consist of the stationary part called stator and

the rotating part named rotor. The stator consists of three-phase windings, which generate the rotating magnetic field. The magnetic field of the rotor is generated by the rotor windings in induction machines and synchronous machines. However, the permanent magnets are used as a counterpart of the rotor windings in permanent magnet synchronous machines (PMSM). Since the rotor field is generated by the permanent magnets, the motor efficiency improves without rotor copper loss. For a given output power, the weight and volume are smaller in PMSMs compared with induction machines or synchronous machines, which leads to a higher power density. Moreover, less heat is generated in PMSMs for a given power input due to the absence of rotor windings (Preindl, 2013; Hughes, 2006; Chan, 2002; Nalakath *et al.*, 2015).

In PMSMs, the permanent magnet can either be mounted on the surface of the rotor core or buried inside the rotor lamination. Compared with the surface mounted permanent magnet (SPM) machine, the interior permanent magnet (IPM) synchronous machine has several advantages on the rotor operating characteristics. Since the permanent magnets are physically installed and protected inside the rotor, the IPM motor is capable of operating at higher speed robustly than the SPM counterpart. Additionally, the buried permanent magnets change the machine magnetic circuit and flux linkage path, which leads to the improvements in the electromagnetic torque production (Jahns *et al.*, 1986; Bilgin *et al.*, 2015).

The proper functioning of the electric machine relies on the electric drive system, which converts the electric energy into mechanical energy (Emadi, 2014; Preindl, 2013). The modern electric motor drive system shown in Figure 1.1 usually comprises the power source, the power electronics converter, the electric machine, the mechanical load and the digital controller. When the electromagnetic torque of the machine

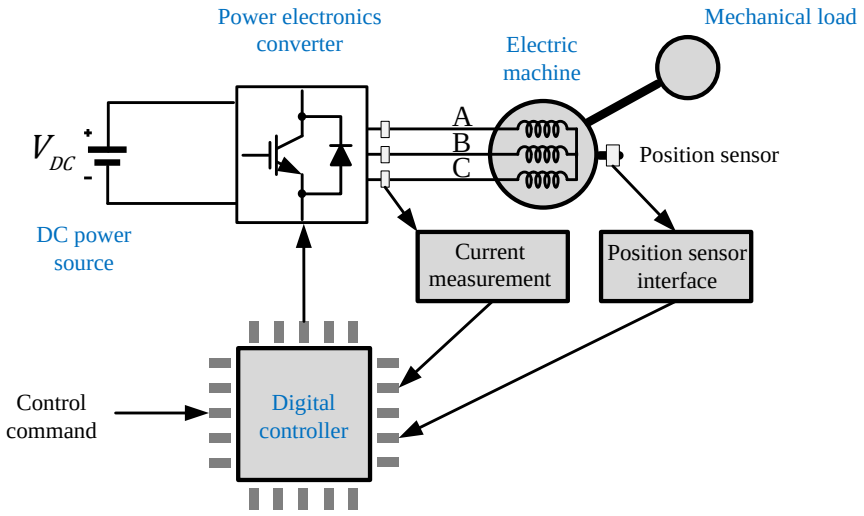


Figure 1.1: The modern electric motor drive system.

has the same direction with the machine speed, the power flow direction is positive (machine consuming energy) and it is called the motor convention. When the machine torque and speed are in the reverse direction, the power flow direction is negative (machine generating energy) and the machine operates in the generator convention (EL-Sharkawi, 2000). In this thesis, the motor convention operation is the sense that mainly focused on.

In the AC machine drive system, the DC power from the power source needs to be transformed into AC power for the generation of the rotating magnetic field. This transformation relies on the voltage source inverter (VSI), which is a specific power electronics converter used in AC motor drives (Preindl, 2013). The electronic switches, e.g. Insulated Gate Bipolar Transistor (IGBT) or Metal-Oxide-Semiconductor-Field Effect Transistor (MOSFET), are controlled by the switching signals provided by the digital controller. In order to achieve the desired performance, the switching signals are generated based on the control reference and measurements. The motor speed

or torque are the commonly used control reference while the voltages are the real quantities that applied on the electric machine. Hence, the reference voltages need to be determined by the control reference based on the specific control algorithms, e.g. Field Oriented Control (FOC) and Direct Torque Control (DTC). Those close loop control algorithms require the feedback of the phase currents and rotor position, which are normally obtained from the specific current sensors and position sensors. With the inverted three phase voltages applied on the stator, the electromagnetic torque can be delivered by the interaction of the stator and rotor fields for the propulsion of the mechanical load.

The rotor position and speed are indispensable in close loop control and achieving maximum torque in AC motor drives. The knowledge of position and speed is usually provided by the specific position sensors (resolver and encoder) in real time. However, the existence of the position sensor increases the machine size. Moreover, the position sensor installation requires the shaft extension and frequent maintenance of the sensors is needed. Besides, the interface between the position sensor output and controller input is required for signal conditioning, which increases the cost of the entire drive system. Additionally, the motor drive system robustness is degraded due to the noise issues existed in the signal transmission between the position sensor and the digital controller, even though specific techniques have been utilized in reducing the noise in the position sensor interface. Hence, much efforts have been focused on new methods for position sensorless control of electric motor drives to avoid sensor-related issues (Sun *et al.*, 2015; Emadi *et al.*, 2008; Fahimi *et al.*, 2004).

The existing sensorless solutions for IPMSM drive system can be divided into two categories, the electromotive force (EMF) based methods and the saliency tracking

based methods. The EMF based methods work robustly in medium and high speed while the saliency tracking based method is more suitable for position sensing at low speed and standstill conditions. For wide speed range operation, different methods need to be combined, which leads to the existence of at least two different speed and position estimators in the drive system. In order to reduce the system complexity, a unified speed and position estimation method for IPMSM drives at wide speed range is proposed in this thesis. The proposed method estimates speed and position by minimizing proposed cost functions which contain the position information in the EMF components as well as in the machine saliency. The feasibility of the proposed unified position sensing method is validated with the prototype IPMSM drive system. Besides the capability of providing speed and position information to the drive system fast and reliably, the proposed method also exhibits several features which will make it attractive to the adjustable speed drives industry.

## 1.2 Contributions

The author has contributed a number of original developments in speed and position estimation of IPM motor drives in this thesis, which are listed as follows:

1. Cost functions based on the voltage equations are proposed for analysis and implementation of the proposed estimation method.

2. A fast and accurate nonlinear optimization based initial position estimation method is proposed and validated.

3. An accurate nonlinear IPM motor model with current-flux look-up tables is proposed and utilized for simulation of the proposed sensorless algorithms.

4. A unified nonlinear optimization based speed and position estimation method at running state is proposed and validated.

5. Comparative assessments between the proposed methods and the benchmark references are exhibited for comprehensively evaluating the proposed estimation methods.

## 1.3 Outline of the Thesis

This thesis presents a unified speed and position estimation method in position sensorless control of IPMSM drives at wide speed range operation including standstill condition. The thesis is mainly focused on: (1) Analysis of the proposed cost functions at different operation conditions; (2) Experimental validation of the proposed sensorless solution at wide speed range; (3) Comparative assessment of the proposed methods with other existing sensorless methods.

Chapter 2 introduces the components of the modern electric drive system. Firstly, fundamentals of IPM motors including the generation and interaction of the stator and rotor flux, the concept of saliency and the torque generation are explained. In order to generate the rotating flux in the stator, the VSI is employed for converting DC voltage into AC voltage. The working theory and different control methods of the VSI are explained. Additionally, the control of AC electric motors requires the knowledge of speed and position. Therefore the position sensors and their interfaces are illustrated as well. Moreover, the torque control of IPM motor drives is explained at the end of this chapter.

Chapter 3 presents the existing sensorless control methods of IPMSM drives. The

EMF based methods which are suitable for medium and high speed operation are introduced and the extended EMF based estimation method is explained in detail and implemented in the prototype IPMSM drive system as a benchmark reference. At low speed including standstill condition, the saliency tracking based methods which employ the continuous signal injection are introduced. The pulsating voltage injection method which relies on the high frequency sinusoidal voltage injection in the estimated rotor reference frame is explained explicitly and is also implemented as a benchmark reference method. Additionally, the existing initial position estimation methods at machine startup are also reviewed. Since the initial position estimation of PMSM usually contains an ambiguity of 180°, the conventional magnetic polarity detection methods in the literature are also studied and presented.

Chapter 4 studies the IPM machine modeling which involves the machine nonlinear inductance profiles. The traditional nonlinear IPM motor model relies on the flux-current look-up tables, which requires the differentiation of the flux. A novel nonlinear machine model which utilizes the current-flux look-up tables is studied and explained in this chapter. Besides, the components of the prototype IPM motor drive system including the MicroAutoBox II, the Silicon-Carbide MOSFET inverter and the high resolution incremental encoder are also briefly presented.

Chapter 5 introduces the proposed initial position estimation method for IPMSM drives at startup and standstill condition. The initial position estimation has three steps. Step I employs the voltage pulse injection in the stationary reference frame and a cost function used in initial position estimation. The rotor position can be estimated by minimizing the cost function with injected voltage and induced current. Since the estimation results in Step I have an ambiguity of 180°, a generalized approach to

polarity detection which exploits asymmetries in machine specific differential inductance profiles is employed as Step II. In order to improve the estimation accuracy, continuous sinusoidal voltage is injected in estimated rotor reference frame in Step III. A modified cost function is minimized based on the injected voltage and resulting current. The effectiveness of the initial position estimation method is demonstrated with high accuracy simulation and the prototype IPMSM drives test bench.

Chapter 6 proposes a nonlinear optimization based position and speed estimation algorithm for wide speed range operations. A cost function which employs both speed and position as decision variables is proposed and utilized for estimation. The speed and position can be estimated by minimizing the proposed cost function based on the measurements of stator voltages and currents. Since the voltage information is less significant at low speed and unable to be observed at standstill condition, extra high frequency sinusoidal voltages are injected in estimated magnetic axis. Extra regularization terms are added in the cost function at low speed to improve speed and position estimation quality. A phase locked loop (PLL) is involved at the output of the position estimator serving as a filter. Analysis on the convexity of the proposed cost functions under different speeds and positions are also presented in this chapter. The feasibility of the proposed estimation algorithm is validated with the experimental setup.

Chapter 7 compares the proposed speed and position estimation methods with the benchmark reference methods mentioned in Chapter 3. The comparisons include both the dynamic and steady state performance during speed and torque transients at wide speed range. Besides the comparison, some other attractive features of the proposed method are also presented in this chapter. Those features include : (1) The

capability of estimating speed and position with multiple voltage injection types; (2) The capability of involving nonlinear motor parameters in the cost functions for initial position estimation; (3) The capability of performing estimation at low sampling frequency. The above features are validated with the experimental tests and the results are presented in this chapter.

The thesis is concluded in Chapter 8 with suggested future work.

# Chapter 2

# Interior Permanent Magnet Synchronous Motor Drives and Control

## 2.1 Introduction

This chapter introduces the basic operational theories of the components in the modern electric motor drive system. Firstly, fundamentals of interior permanent magnet (IPM) motor including the generation and interaction of the stator and rotor flux, the concepts of coordinate transformation, saliency and the torque generation are explained. The three-phase voltage source inverter (VSI) is usually employed for converting DC voltage into AC voltage for generating the rotating magnetic field in the stator. The working theory and two different modulation methods in controlling the VSI are introduced. Additionally, the control of AC electric machines requires the knowledge of speed and position, which relies on the existence of the position sensors

and their interfaces in the drive system. Therefore, the position sensors and the corresponding interfaces are briefly illustrated. Moreover, the IPMSM optimal operation and field oriented control (FOC) which requires the rotor position are explained in detail at last.

## 2.2 Fundamentals of Interior Permanent Magnet Synchronous Motor

### 2.2.1 Stator Voltage Equations

According to Faraday's Law, an electromotive force (EMF) is generated when a conductor is placed in a time-changing magnetic flux flows (Emadi, 2014), which is calculated as

$$e_{con}(t) = p\lambda_{con}(t), \tag{2.1}$$

where $e_{con}(t)$, $\lambda_{con}(t)$ and $p$ denote the EMF, flux linkage and the differential operator respectively.

If the resistance of the conductor $R_{con}$ is taken into account, then the terminal voltage $u_{con}(t)$ across the conductor is represented as

$$u_{con}(t) = R_{con}i_{con}(t) + e_{con}(t), \tag{2.2}$$

where $i_{con}(t)$ represents the time-changing current flowing in the conductor.

In PMSM drives, the three phase windings are excited by sinusoidal voltages with

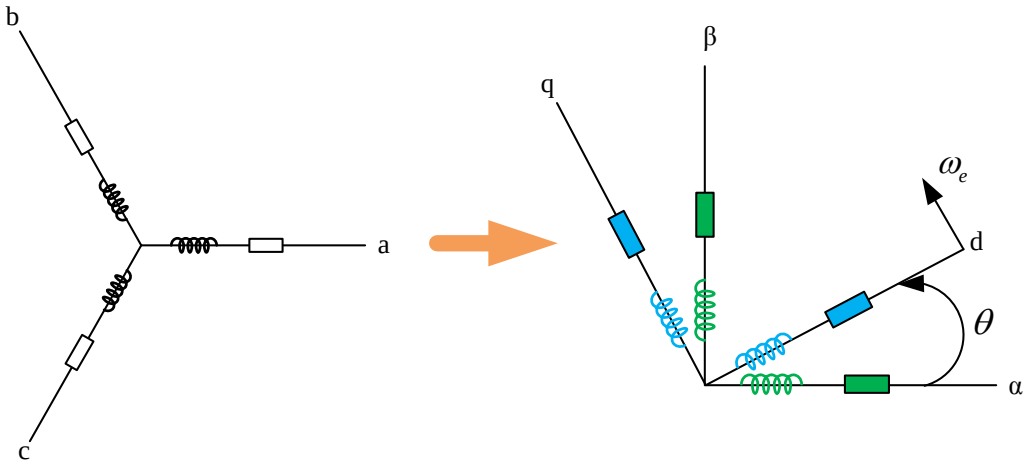


Figure 2.1: Clark and Park Transformations.

120° electrical degree apart. The three phase voltages $u_{abc}(t)$ can be represented similarly as

$$u_{abc}(t) = R_s i_{abc}(t) + e_{abc}(t), \tag{2.3}$$

where $R_s$, $i_{abc}(t)$ and $e_{abc}(t)$ denote the phase resistance, three-phase currents and EMFs in the three phases respectively.

In the normally used field oriented control, the voltages and currents need to be regulated in a frame which rotates with the rotor. That frame is named rotor reference frame or *d-q* frame. The quantities including voltages and currents in the three-phase coordinates need to be transformed into this rotating *d-q* frame, as shown in Figure 2.1. The first procedure of the transformation is called Clark Transformation which converts the three phase quantities into the stationary reference frame ($\alpha$-$\beta$ frame).

The equation of the Clark Transformation is

$$\begin{bmatrix} Q_\alpha \\ Q_\beta \end{bmatrix} = C_{\alpha\beta} \begin{bmatrix} Q_a \\ Q_b \\ Q_c \end{bmatrix} = \frac{2}{3} \begin{bmatrix} 1 & -\frac{1}{2} & -\frac{1}{2} \\ 0 & \frac{\sqrt{3}}{2} & -\frac{\sqrt{3}}{2} \end{bmatrix} \begin{bmatrix} Q_a \\ Q_b \\ Q_c \end{bmatrix}, \tag{2.4}$$

where $Q_{abc}$ and $Q_{\alpha\beta}$ represent the quantities (voltages and currents) in the three-phase coordinates and the $\alpha$-$\beta$ frame respectively.

The quantities in the stationary reference frame then need to be transformed into the rotor reference frame by the Park Transformation, which is illustrated in

$$\begin{bmatrix} Q_d \\ Q_q \end{bmatrix} = T_{dq} \begin{bmatrix} Q_\alpha \\ Q_\beta \end{bmatrix} = \begin{bmatrix} \cos\theta & \sin\theta \\ -\sin\theta & \cos\theta \end{bmatrix} \begin{bmatrix} Q_\alpha \\ Q_\beta \end{bmatrix}, \tag{2.5}$$

where $\theta$ denotes the rotor position with respect to the $\alpha$ axis or phase A.

With Clark and Park Transformations, the steady-state AC variables perform like DC quantities and the DC machine control methods can be applied to the AC machine control as well (Emadi, 2014). The time domain stator voltage equations in $d$-$q$ frame are

$$\begin{bmatrix} u_d(t) \\ u_q(t) \end{bmatrix} = R_s \begin{bmatrix} i_d(t) \\ i_q(t) \end{bmatrix} + p \begin{bmatrix} \lambda_d(t) \\ \lambda_q(t) \end{bmatrix} + \omega_e(t) \begin{bmatrix} -\lambda_q(t) \\ \lambda_d(t) \end{bmatrix}. \tag{2.6}$$

The $u_{dq}(t)$, $i_{dq}(t)$ and $\lambda_{dq}(t)$ are the voltages, currents and fluxes in $d$-$q$ frame, which are DC quantities. The $\omega_e(t)$ denotes the synchronous speed. It is called synchronous speed because the stator and rotor fluxes both rotate at this speed.

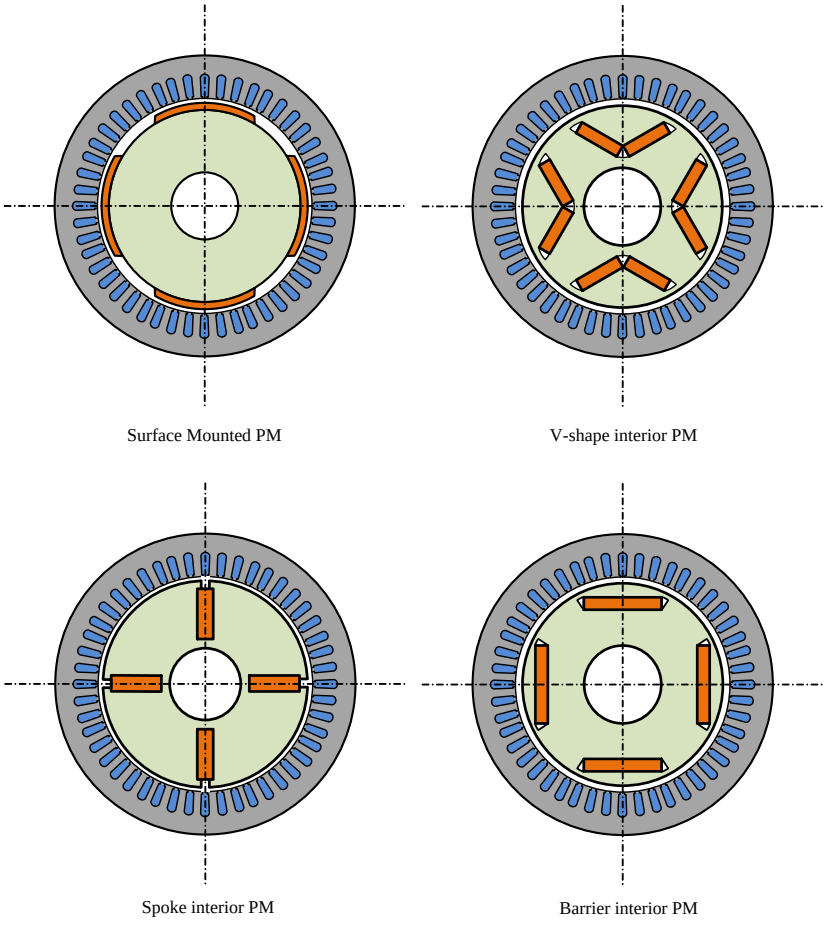


Figure 2.2: Different rotor configurations of PMSM machines.

### 2.2.2 Flux, Inductance and Torque

In permanent magnet machines, the stator flux is excited by the time-changing sinusoidal currents in the windings and the rotor flux is generated by the permanent magnets installed in the rotor. As mentioned in Section 1.1, the permanent magnets can be glued on the surface of the rotor or mounted inside the rotor lamination. Figure 2.2 shows different rotor configurations of the PMSMs (Emadi, 2014).

If the stator flux is transformed into $d$-$q$ frame, then the positive direction of $d$

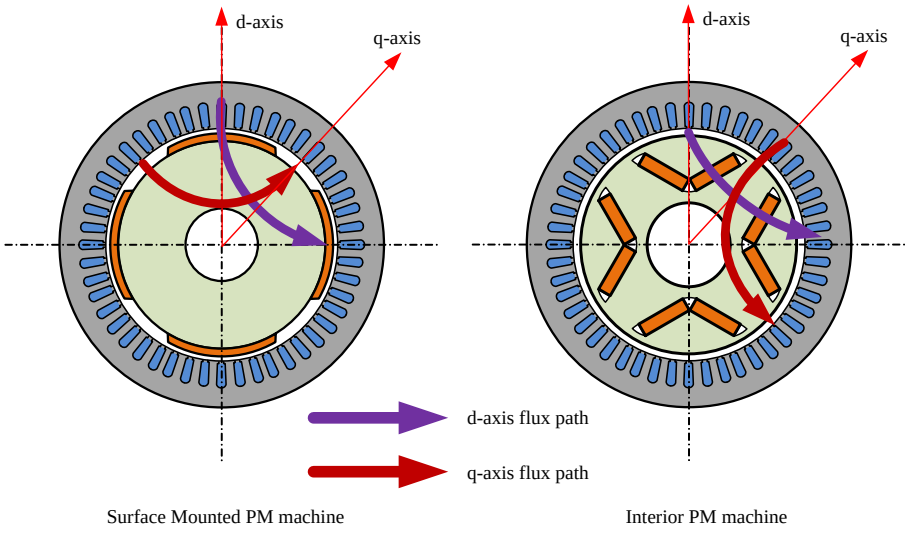


Figure 2.3: The $d$-$q$ axes flux paths in PMSMs.

axis aligns with the rotor flux. Figure 2.3 depicts the $d$–$q$ axes flux paths. The air gap flux is a superposition of stator and rotor flux which is calculated in

$$\begin{bmatrix} \lambda_d(t) \\ \lambda_q(t) \end{bmatrix} = \begin{bmatrix} L_d & 0 \\ 0 & L_q \end{bmatrix} \begin{bmatrix} i_d(t) \\ i_q(t) \end{bmatrix} + \begin{bmatrix} \lambda_{pm} \\ 0 \end{bmatrix}, \tag{2.7}$$

where $L_{dq}$ and $\lambda_{pm}$ represent the $d$-$q$ axes inductances and the permanent magnet flux linkage.

In surface mounted permanent magnet (SPM) machines, the inductances in $d$ and $q$ axis are almost the same due to the fact that the permanent magnet and the air have the similar permeability. However, the $d$ and $q$ axis flux paths are different in IPM machines due to the buried permanent magnets in the rotor lamination. The $d$ axis flux flows through two permanent magnets in the rotor which has larger reluctance than the magnetic steels while the $q$ axis flux path only crosses the steel lamination (Emadi, 2014). Hence, the $q$ axis inductance is larger than the $d$ axis inductance.

The saliency ratio $L_q/L_d$ is usually employed for quantify the difference between $L_d$ and $L_q$ and it varies in different IPM motor designs.

The equation of the electromagnetic torque $T_e$ in IPM machine is shown in

$$T_e = \frac{3}{2}P\big(\lambda_{pm} i_q + (L_d - L_q) i_d i_q\big), \tag{2.8}$$

where $P$ denotes the number of pole pairs. In (2.8), the electromagnetic torque has two components. The first component $3/2P\lambda_{pm}i_q$ is called the permanent magnetic torque which is generated due to the interaction between the rotor permanent magnet flux and the stator flux. The second component $3/2P(L_d - L_q)i_d i_q$ is named reluctance torque which doesn't exist in SPM. It is produced by the tendency that tracks the minimum reluctance path (Preindl, 2013).

In this section, the constant motor parameters are used in the analysis. In reality, the stator and rotor flux are nonlinear due to the saturation and the cross-saturation effects. Those machine nonlinearities will be introduced in Chapter 4 in detail.

## 2.3 Inverter Control and Pulse Width Modulation

The VSI shown in Figure 2.4 is commonly used in adjustable speed IPM motor drive system for generating variable frequencies and magnitudes AC output voltages from the DC link voltage source. The three-phase output voltages are applied by the three pairs of switches triggered by the switching signals from the digital controller. The IGBT and MOSFET are usually employed in the VSI as electronic switches while in Figure 2.4, the transistors symbols are used as an illustration for simplicity (Quang and Dittrich, 2008; Devices, 2000).

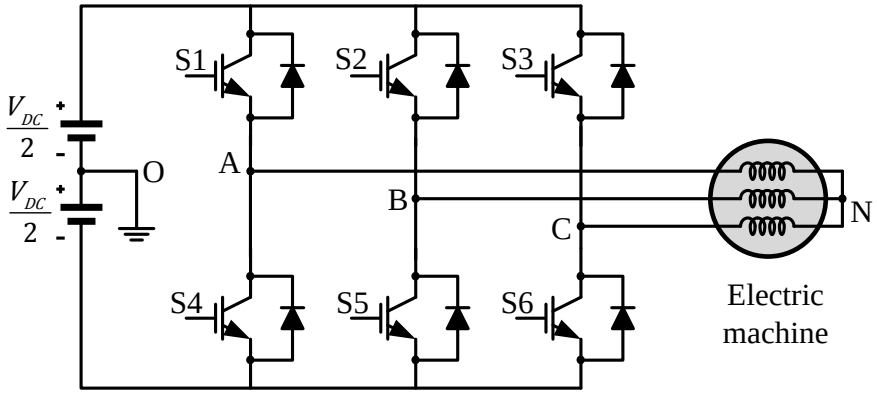


Figure 2.4: Voltage Source Inverter.

Pulse Width Modulation (PWM) is widely applied in motor drives for reproducing the reference voltages or currents. It controls the average output voltage by producing variable duty cycle pulses within small switching period $T_c$. Since the switching frequency is much higher compared with the frequency of the output voltage, the PWM output voltage can be treated as the same with the reference voltage. In the AC motor drive system, the typical method used for reproducing the desired output sinusoidal voltages is called sinusoidal PMW (SPWM), which compares the reference sinusoidal voltages to the carrier sawtooth voltages in the switching frequency. If the reference voltage is larger than the carrier voltage, the upper switch will be turned on and the lower switch in the same bridge will be off complementarily. In this case, the voltage between phase A terminal and the neutral point of the drive system $u_{AO} = V_{dc}/2$ where $V_{dc}$ denotes the DC link voltage. While if the reference voltage is smaller than the carrier voltage, the lower switch will be on and the upper switch will be turned off, which leads to $u_{AO} = -V_{dc}/2$. The working theory of SPMW is shown in Figure 2.5 (Devices, 2000). The PWM sinusoidal voltage then can be generated and its frequency and magnitude are determined by the reference voltage. The maximum

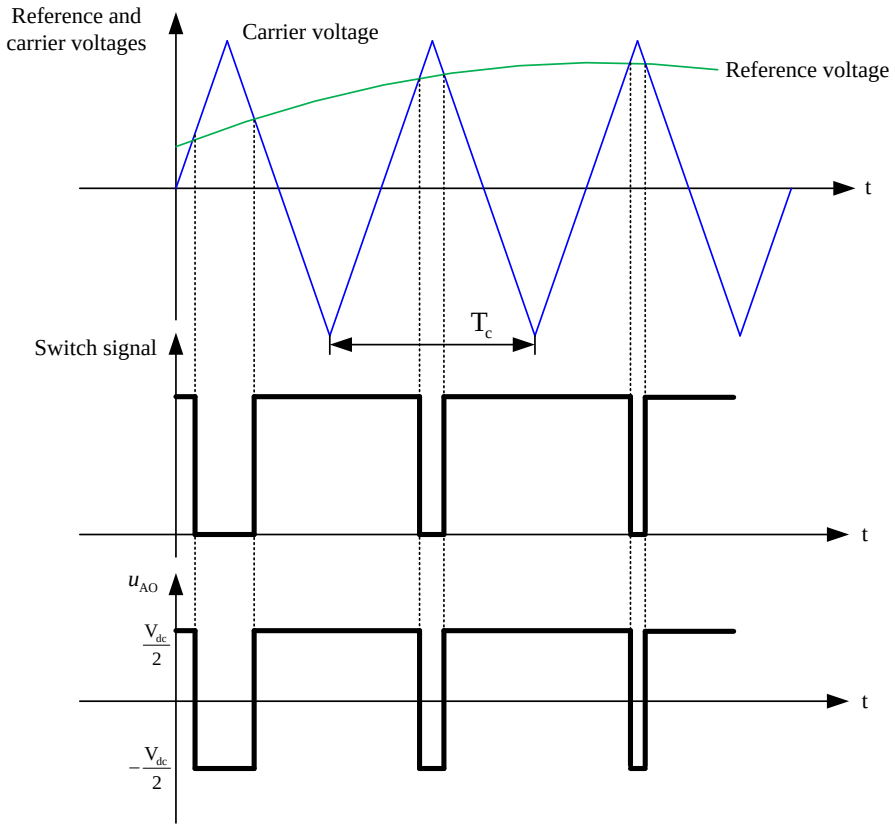


Figure 2.5: Sinusoidal pulse width modulation.

voltage waveform generated by this demodulation method is $V_{dc}/2$ with a square waveform. The fundamental frequency component of the square waveform is $2V_{dc}/\pi$ and the modulation index $M_i$ is calculated as

$$M_i = \frac{V_{dc}/2}{2V_{dc}/\pi} = 78.54\%, \tag{2.9}$$

which indicates that the maximum utilization of the DC linkage voltage in SPWM is 78.54% (Hart, 2010).

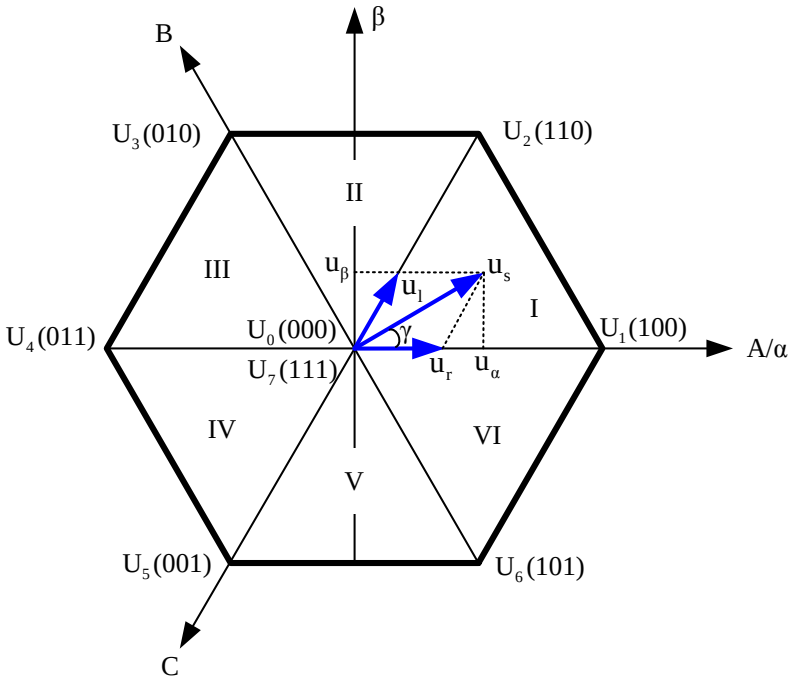


Figure 2.6: Voltage vectors in SVPWM

In order to improve the utilization of the DC link voltage, another type of modulation method, space vector pulse width modulation (SVPWM) is also widely employed in AC motor drives. For each individual switch there are two states, i.e. on and off. In this way, there are $2^6$ possibilities of the switching conditions. There are only 8 effective combinations among the $2^6$ possibilities and they are listed in Table. 2.1. The number **0** denotes the condition when the upper switch is off and the lower switch is on and the number **1** represents the reversed condition (Quang and Dittrich, 2008).

Table 2.1: Voltage vectors in SVPWM

| Voltage vector | $\mathbf{U}_0$ | $\mathbf{U}_1$ | $\mathbf{U}_2$ | $\mathbf{U}_3$ | $\mathbf{U}_4$ | $\mathbf{U}_5$ | $\mathbf{U}_6$ | $\mathbf{U}_7$ |
|---|---|---|---|---|---|---|---|---|
| Phase A | 0 | 1 | 1 | 0 | 0 | 0 | 1 | 1 |
| Phase B | 0 | 0 | 1 | 1 | 1 | 0 | 0 | 1 |
| Phase C | 0 | 0 | 0 | 0 | 1 | 1 | 1 | 1 |

If the reference voltage vector $\mathbf{u}_s$ locates in Sector I in Figure 2.6, the $\mathbf{u}_s$ can be obtained as the vector addition of boundary vectors $\mathbf{u}_r$ and $\mathbf{u}_l$ in the same directions with $\mathbf{U}_1$ and $\mathbf{U}_2$ (Quang and Dittrich, 2008). Since $\mathbf{u}_r$ and $\mathbf{u}_l$ are proportional to $\mathbf{U}_1$ and $\mathbf{U}_2$, the time span of each voltage vector in Sector I are calculated as

$$\begin{aligned} T_r &= \frac{T_c}{2}\frac{|\mathbf{u}_r|}{|\mathbf{U}_1|} \\ T_l &= \frac{T_c}{2}\frac{|\mathbf{u}_l|}{|\mathbf{U}_2|} \end{aligned} \tag{2.10}$$

where $|\mathbf{U}_1| = |\mathbf{U}_2| = \frac{2V_{dc}}{3}$.

For the rest time of the half switching period $T_c/2$, the zero vectors ($\mathbf{U}_0$ and $\mathbf{U}_7$) need to be applied. In order to reduce the switching loss, the favorable switching pattern is to change the state of only one switch for applying different voltage vectors. The expected switching pattern is shown in Figure 2.7. The time spans of the zero vectors are equally distributed to $\mathbf{U}_0$ and $\mathbf{U}_7$ and it is calculated as

$$T_0 = \frac{T_c}{2} - (T_r + T_l). \tag{2.11}$$

Then the reference voltage vector $\mathbf{u}_s$ is finally represented as

$$\mathbf{u}_s\frac{T_c}{2} = \frac{T_0}{2}\mathbf{U}_0 + T_r\mathbf{U}_1 + T_l\mathbf{U}_2 + \frac{T_0}{2}\mathbf{U}_7. \tag{2.12}$$

The process of realizing the voltage vector in Sector II-VI is similar as what has been explained in Sector I. In order to calculate $T_r$ and $T_l$, the magnitudes of the boundary vectors $\mathbf{u}_r$ and $\mathbf{u}_l$ needs to be calculated. First of all, the reference voltages for SVPWM need to be transformed into $\alpha - \beta$ frame using (2.4). Then the

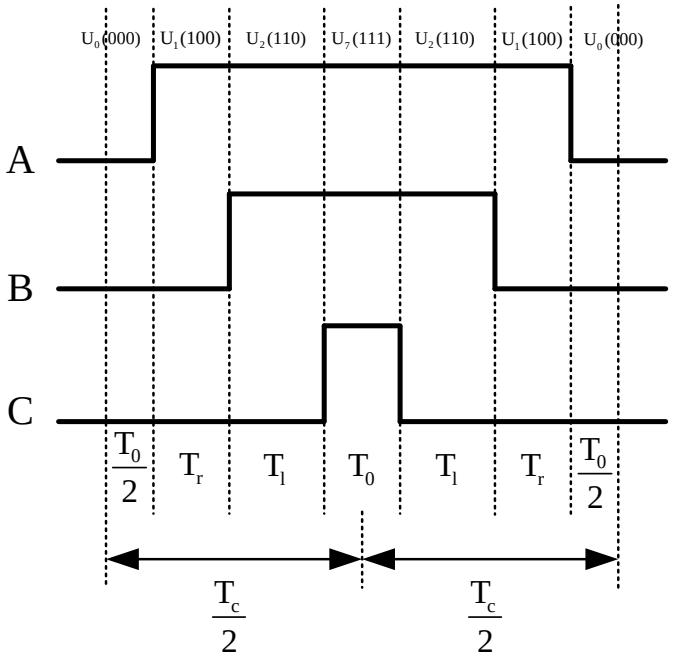


Figure 2.7: Switching pattern in Sector I.

magnitudes of the boundary vectors are calculated in

$$
\begin{aligned}
|\mathbf{u}_r| &= \frac{2}{\sqrt{3}}|u_s|sin(60^\circ - \gamma) \\
|\mathbf{u}_l| &= \frac{2}{\sqrt{3}}|u_s|sin\gamma \\
\gamma &= arctan\frac{u_\beta}{u_\alpha},
\end{aligned}
\tag{2.13}
$$

where $u_{\alpha\beta}$ denotes the voltages in $\alpha - \beta$ frame and $\gamma$ represents the angle between the reference voltage vector and $\alpha$ axis. The angle $\gamma$ is also employed for deciding the sector where $\mathbf{u}_s$ locates.

Figure 2.8 depicts the comparison between SPWM and SVPWM. By utilizing SVPWM, the maximum voltage magnitude which can be achieved is $OM = \sqrt{3}V_{dc}/3$.

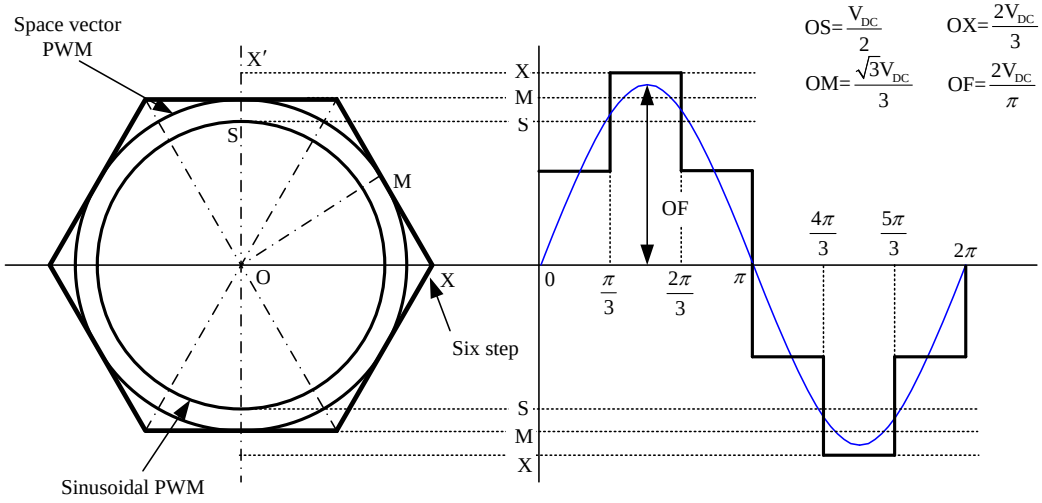


Figure 2.8: Comparison between SPWM and SVPWM.

The maximum phase voltage that can be generated by a three-phase inverter from a certain DC link voltage occurs when the six step operation is employed. The fundamental frequency voltage magnitude is $2V_{dc}/\pi$ (Hart, 2010), which is the length of OF in Figure 2.8. Then the modulation index of the SVPWM is

$$M_i = \frac{\sqrt{3}V_{dc}/3}{2V_{dc}/\pi} = 90.69\%, \tag{2.14}$$

which indicates a higher utilization of the DC linkage voltage compared with SPWM.

If the maximum voltage magnitude is less than the length of OM, the SVPWM works in the linear region. It is possible to increase the modulation index further by operating in discontinuous SVPWM, which is not discussed in this thesis.

## 2.4 Position Sensors and Interface

In (2.5), the transformation from $\alpha$-$\beta$ frame into $d$-$q$ frame requires the knowledge of rotor position $\theta$. Moreover, the motor speed needs to be measured in the close loop speed control. The speed and position acquisition is usually achieved by the position sensors. Resolvers and Encoders are the two types of widely used position sensors in industry.

### 2.4.1 Resolver and Its Interface

The working theory of the resolve is similar as a variable coupling transformer which transmits the magnetic energy from the primary winding to the secondary winding. It consists of two parts, the stator and the rotor. The typical resolver has a primary winding on the rotor and two secondary windings on the stator (Szymczak *et al.*, 2014). However, this scheme requires slip rings for excitation of the magnetic field in the rotor. So another type of resolver named variable reluctance resolver, which has both the primary winding and secondary windings mounted on the resolver stator, is more welcomed in industry. Figure 2.9 (a) depicts the variable reluctance resolvers manufactured by Tamagawa (Tamagawa, 2014). In variable reluctance resolvers, the sinusoidal variation caused by the rotor movement is coupled from the primary winding to the secondary windings through the rotor saliency (Szymczak *et al.*, 2014).

Figure 2.10 shows the structure of the variable reluctance resolver. The primary winding is excited by sinusoidal voltages. The induced voltages in the secondary windings are functions of the rotor position and their magnitudes are proportional to the excitation voltage with a ratio $N_r$. Since the two secondary windings are displaced orthogonal with each other, the induced voltages in the two windings have 90° phase

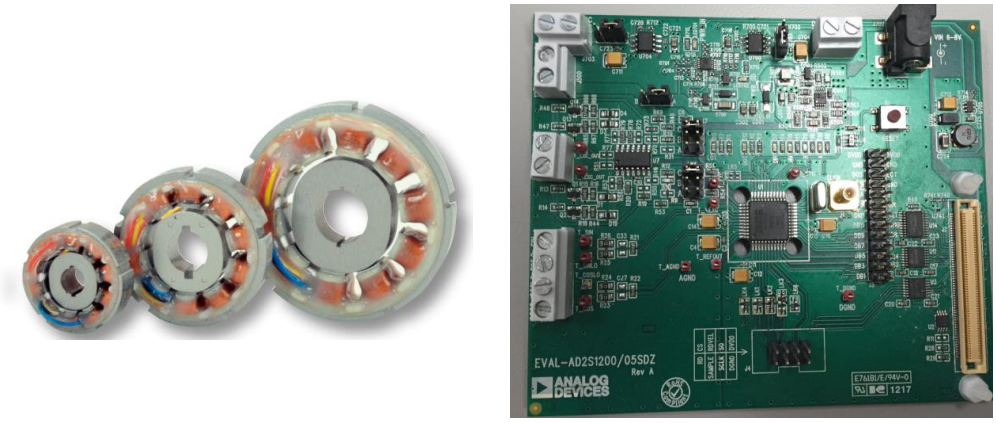


(a) Tamagawa resolvers

(b) Resolver interface evaluation board (AD2S1200 Based)

Figure 2.9: Resolver and its interface.

shift. The voltage equations of the primary and secondary windings are shown in

$$\begin{aligned} V_{pr} &= E_0 sin\omega_0 t \\ V_{13} &= N_r E_0 sin\omega_0 t \sin\theta \\ V_{24} &= N_r E_0 sin\omega_0 t \cos\theta, \end{aligned} \tag{2.15}$$

where $E_0$ and $\omega_0$ denote the magnitude and frequency of the excitation voltage in the primary winding.

From (2.15), it is clear to see that the rotor position $\theta$ is contained in the induced voltages $V_{13}$ and $V_{24}$. The extraction of the rotor position information and the excitation of the primary winding both rely on the resolver interface. Figure 2.9 shows one type of resolver interface, which is the evaluation board manufactured by Analog Devices based on AD2S1200. The working theory of speed and position extraction from the resolver interface is shown in Figure 2.11. In order to obtain the rotor position, an angle $\varphi$ is generated by the interface and is incorporated with $V_{13}$ and $V_{24}$

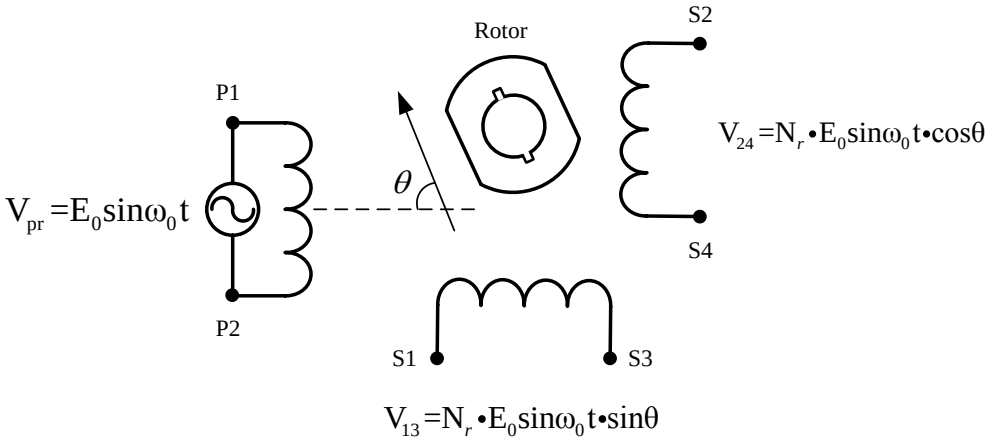


Figure 2.10: Variable reluctance resolver.

in the trigonometric function format, which is shown in

$$\begin{aligned} f_1(\theta-\varphi) &= N_r E_0 sin\omega_0 t \sin\theta\cos\varphi - N_r E_0 sin\omega_0 t \cos\theta \sin\varphi \\ &= N_r E_0 sin\omega_0 t(\sin\theta\cos\varphi - \cos\theta\sin\varphi) = N_r E_0 sin\omega_0 t \sin(\theta-\varphi). \end{aligned} \quad (2.16)$$

Then $f_1(\theta-\varphi)$ is demodulated by multiplying $sin\omega_0 t$ and the final position error function $f_3(\theta-\varphi)$ is obtained after the low pass filter, which is

$$f_3(\theta-\varphi) = \frac{1}{2} N_r E_0 \sin(\theta-\varphi). \quad (2.17)$$

When this estimator finally converges, $f_3(\theta-\varphi)$ tends to be zero and under that case the generated angle $\varphi$ equals to the actual position. In this way, the shaft speed and the rotor position can be measured and fed back to the control system.

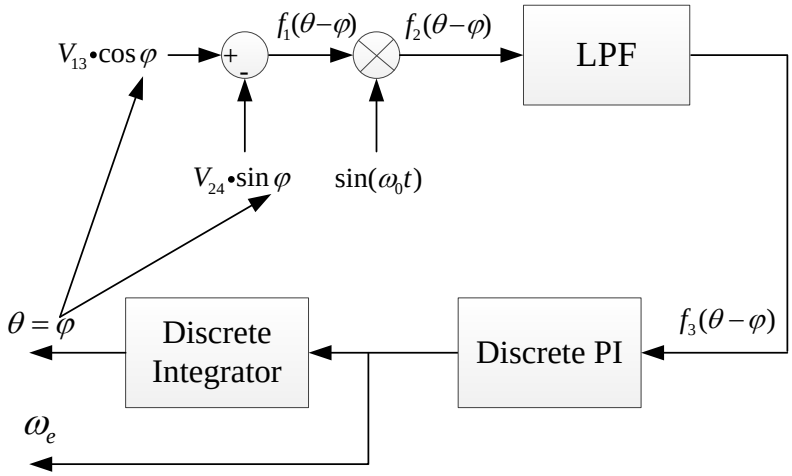


Figure 2.11: Speed and position extraction from the resolver interface.

### 2.4.2 Encoder and Its Interface

One of the drawbacks of the resolvers introduced in Section 2.4.1 is its restricted maximum speed measurement capability due to the limitation of the resolver signal frequencies, which is usually less than 5 KHz (Byrd, 2014). Moreover, the shaft vibration will also affect the proper functioning of the resolver in speed and position measurement. So a digital counterpart named encoder is also widely applied in the position sensing industry. An encoder is a device which can translate the position information into specific digital signals. It can be used for measuring the velocity and position in a single direction (linear encoder), or employed for angular displacement and speed (rotary encoder). The latter one is more widely used in the motor drive system and is usually mounted on the extended shaft of the machine. Figure 2.12 (a) shows one type of encoders manufactured by BEI Sensors (Sensors, 2015).

The output signal of the encoder can be generated in the electrical way (sliding contact encoder) or the magnetic way (magnetic encoder), but the most widely used

Figure 2.12: BEI incremental encoder.

encoder is the optical encoder. It has a specific pattern on the rotating disk which can either allow or block the light passing through. A light source and a light sensor need to work along with the rotating disk for producing position related disk counts.

In terms of the movement identification and interpretation of the output, the optical encoder can be divided into the absolute encoder and the incremental encoder. Figure 2.13 shows the different disk patterns of the absolute encoder and the incremental encoder. They both have transparent windows which can pass through the light on the opaque disk. In the absolute encoder, the position information can be directly translated into specific binary codes as shown in Figure 2.13 (a). The Gray code is also used in order to avoid the ambiguity in bit switching in absolute encoders (Kimbrell, 2013).

Different with the absolute encoder, the incremental encoder shown in Figure 2.13 (b) only shows the relative position change and how far the shaft has rotated after the encoder is powered up (Kimbrell, 2013). The pattern on the disk generates a

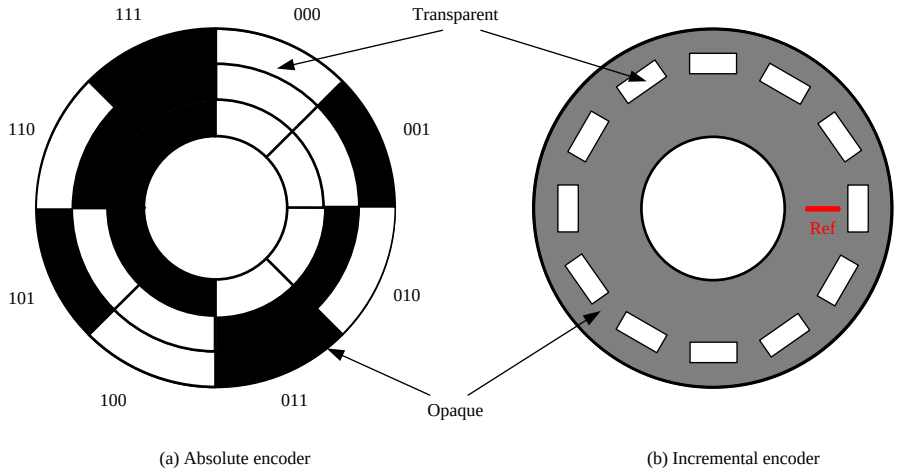


Figure 2.13: Absolute and incremental encoders.

digital high voltage or low voltage based on the fact whether the light is allowed to pass through the transparent window or is blocked by the opaque disk. The generated electric pulse is counted for calculating the angular speed and position. The electrical pulses can either be recorded in single channel or double channels (quadrature output). In quadrature output, two different channels named A and B are 90° phase shifted, which is shown in Figure 2.14. The two outputs can be both high or low, which leads to four different states shown in Table. 2.2. The quadrature output can provide four times pulses than the single channel. Besides the two channels, certain incremental encoders also have a physical reference called index reference which provides the zero position of the incremental encoder. When the rotating disk passes through the reference, the position value will be reset to zero.

Table 2.2: Quadrature output states

| States | S1 | S2 | S3 | S4 |
|---|---|---|---|---|
| Channel A | 1 | 1 | 0 | 0 |
| Channel B | 0 | 1 | 1 | 0 |

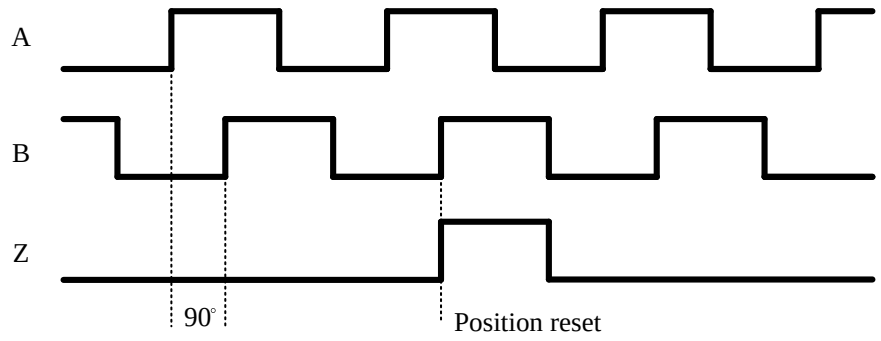


Figure 2.14: Quadrature output in incremental encoder.

Assuming that the incremental encoder can generate $M$ pulses in one turn, the current position $\theta_{enc}$ can be represented as

$$\theta_{enc} = \frac{2\pi N_{count}}{M}, \tag{2.18}$$

where the $N_{count}$ denotes the count of the electrical pulses.

The speed $\omega_{enc}$ is calculated in

$$\omega_{enc} = \frac{2\pi \Delta N_{count}}{M T_{enc}}, \tag{2.19}$$

where $T_{enc}$ and $\Delta N_{count}$ represent the sample time of the encoder and the number of pulses between two consecutive encoder sample times.

In order to cancel the common mode noises on the quadrature output during the data transmission, the line drive signals with two separate wires for each channel ($A$ and $\bar{A}$; $B$ and $\bar{B}$; $Z$ and $\bar{Z}$) are usually used. The line driver outputs are converted to the common mode signal by specific quadruple differential line receivers, e.g. AM26LV32C (Instruments, 2005). The converted encoder outputs are processed

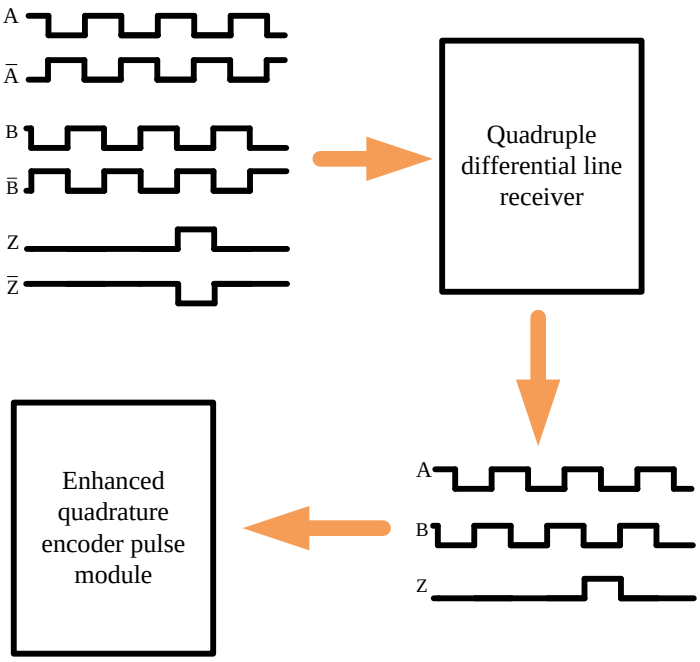


Figure 2.15: The working theory of the incremental encoder interface.

by the enhanced quadrature encoder pulse (eQEP) module built in the DSP for extracting the speed and position information (Instruments, 2015) The working theory of the incremental encoder interface is shown in Figure 2.15.

## 2.5 Control of Interior Permanent Magnet Synchronous Motor

In AC motor drives, controlling three phase voltages or currents separately has several drawbacks due to the interaction among three phase fluxes and the difficulty in performing a sinusoidal current regulation with PI controllers (Europe, 1998). The idea of field oriented control comes from the expectation of controlling the AC machines

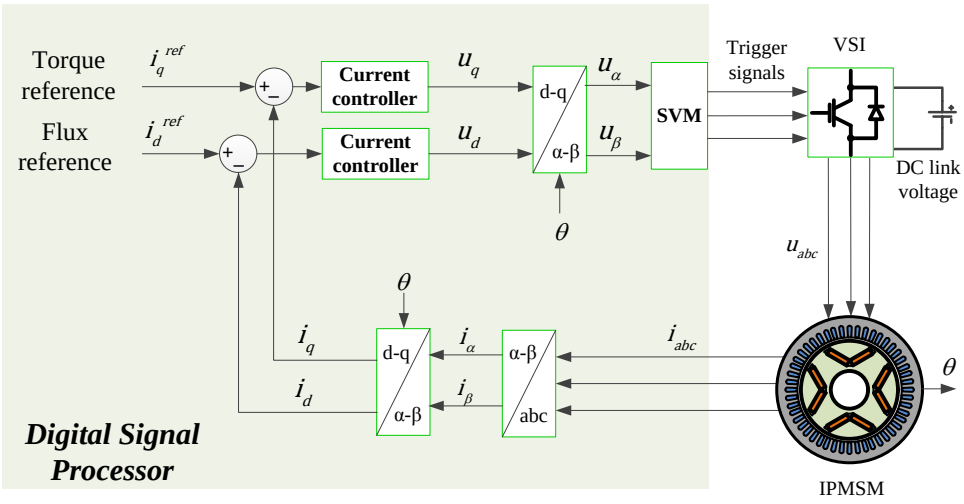


Figure 2.16: Block diagram of the FOC in IPM motor drives.

with DC motor control techniques. In order to achieve it, the three-phase quantities (voltage and current) are transformed from a three-phase time-dependent coordinate into the two-coordinate time-invariant *d-q* frame, which has already been introduced in Section 2.2. The rotor flux generated by the permanent magnets aligns with the rotating flux induced in the stator and they both rotate at the synchronous speed. In this way, the flux and torque can be controlled separately (Emadi, 2014; Europe, 1998; Bilewski *et al.*, 1993). Figure 2.16 illustrates the block diagram of the FOC in IPM motor drives.

In the practical IPM motor drives, the stator voltages and currents need to be limited due to the inverter capacity. If the phase resistance is ignored, then the voltage is limited in

$$u_d^2 + u_q^2 = \omega_e^2\left(L_q^2 i_q^2 + (L_d i_d + \lambda_{pm})^2\right) \leq V_{lim}^2, \tag{2.20}$$

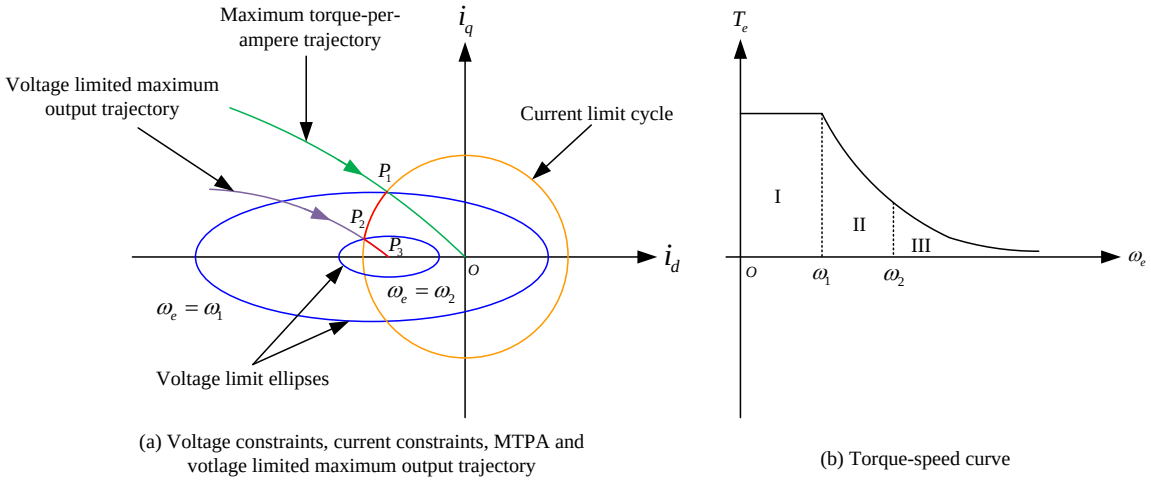


(a) Voltage constraints, current constraints, MTPA and votlage limited maximum output trajectory

(b) Torque-speed curve

Figure 2.17: Optimal IPM motor operation with voltage and current limits and torque-speed curve.

where $V_{lim}$ denotes the maximum output voltage of the three phase inverter (Morimoto *et al.*, 1990; Cheng and Tesch, 2010), which is $2V_{dc}/\pi$ mentioned in Section 2.3. The voltage limit is represented as the voltage limit ellipse shown in Figure 2.17 (a).

The stator current also has the limitation decided by the continuous stator current rating of the machine and the output current limit of the inverter (Morimoto *et al.*, 1990). The current limit $I_{lim}$ is illustrated in

$$i_d^2 + i_q^2 \leq I_{lim}^2, \tag{2.21}$$

which is depicted as a current limit cycle shown in Figure 2.17 (a).

Assume $\theta_s$ is the angle between the stator current vector $I_s$ and the negative direction of $d$ axis, the relationship between the stator current and the $d$-$q$ axes

currents are shown in

$$\begin{aligned} i_d &= -I_s \cos\theta_s \\ i_q &= I_s \sin\theta_s. \end{aligned} \tag{2.22}$$

Then the electromagnetic torque shown in (2.8) can be represented as a function of $I_s$ and $\theta_s$. In order to get the maximum utilization of the current, the maximum torque-per-ampere (MTPA) needs to achieved. For a specific $I_s$, the maximum torque can be obtained when $dT_e/d\theta_s = 0$. Combining (2.8) and (2.22), the following equation is obtained as

$$2(L_q - L_d)I_s \cos^2\theta_s + \lambda_{pm}\cos\theta_s - (L_q - L_d)I_s = 0. \tag{2.23}$$

Combining (2.22) and (2.23), the final relationship between $i_d$ and $i_q$ to achieve MTPA is shown in

$$i_d = \frac{\lambda_{pm} - \sqrt{\lambda_{pm}^2 + 4(L_q - L_d)^2 i_q^2}}{2(L_q - L_d)}. \tag{2.24}$$

The MTPA trajectory is shown in Figure 2.17 (a). Before the MTPA trajectory intersects the current limit cycle, the rated torque can be maintained by applying the current vector fixed in $P1$ and the motor speed can increase with the maximum torque until it reaches the motor base speed $\omega_1$ (Morimoto *et al.*, 1990), which is

$$\omega_1 = \frac{V_{lim}}{\sqrt{L_q^2 i_q^2 + (L_d i_d + \lambda_{pm})^2}}. \tag{2.25}$$

When the motor speed is below the base speed, the motor is running in region I in Figure 2.17 (b), which is usually called the constant torque mode. If the motor speed keeps increasing, the current vector trajectory has to move along the current limit cycle towards $P2$, which is the intersection of the current limit cycle and the voltage limited maximum output trajectory (Morimoto *et al.*, 1990; Uddin *et al.*, 2002). When the current vector trajectory moves from $P1$ to $P2$, the motor speed increases from $\omega_1$ to $\omega_2$ and the currents in $d$-$q$ axes need to satisfy

$$\begin{aligned} i_d &= \frac{-\lambda_{pm} + \sqrt{\frac{V_{lim}^2}{\omega_e^2} - L_q^2 i_q^2}}{L_d} \\ i_d^2 + i_q^2 &= I_{lim}^2. \end{aligned} \tag{2.26}$$

The above operation condition is also represented as region II in the torque-speed curve in Figure 2.17 (b). This region consists of all the intersections of the current limit cycle and voltage limit ellipses. As shown in (2.26), the current and voltage both reach to the limits and this region is usually named constant power region. When the motor speed is above $\omega_2$, the $V_{lim}$ is satisfied while the current limit $I_{lim}$ can not be reached. It is called reduced power mode (Bianchi and Bolognani, 1997) and is depicted as the trajectory from $P2$ to $P3$ in Figure 2.17 (a) and the region III in Figure 2.17 (b).

## 2.6 Conclusions

In this chapter, the basic working theories of the components used in the modern electric motor drive system are introduced. In order to generate electromagnetic torque

for propelling the mechanical load, the DC voltage needs to be converted to three phase AC voltages through the voltage source inverter. By using SPWM or SVPWM illustrated in this chapter, this conversion can be achieved. The electromagnetic torque is generated by the interaction between the rotating stator flux and the rotor flux provided by the permanent magnets. The electromagnetic torque is controlled by regulating the currents in the rotor reference frame. The field oriented control and IPMSM optimal operation are introduced and explained in this chapter. Moreover, in order to achieve field oriented control, the knowledge of the rotor position and speed is needed. The working theories of the position sensors and their interfaces are also explained in this chapter in detail.

# Chapter 3

# Existing Sensorless Control Methods of IPM Motor Drives

## 3.1 Introduction

High performance AC motor control requires the knowledge of rotor position and speed. Specific position sensors (resolver and encoder) are normally used in providing the position and speed information in real time as introduced in Section 2.4. However, the existence of the position sensor increases the machine size and frequent maintenance of the sensors is needed. Moreover, additional signal conditioning circuits are needed for interfacing the sensor output signals with the digital controller, which increase the cost of the entire drive system. Additionally, the transmission between the sensors and the controller through specific interfaces may be affected by the external noise that degrades the system robustness. Hence, much efforts have been focused on new methods for speed and position sensorless control of IPMSM drives to avoid sensor-related issues (Sun *et al.*, 2015). In this chapter, the speed

and position estimation algorithms of IPMSM drives at standstill, low speed, high speed and wide speed range are introduced respectively. Typical existing methods are explained explicitly and are implemented experimentally as benchmark references of the proposed methods.

## 3.2 EMF Based Speed and Position Estimation

Sensorless control methods can be classified into two categories. The first category is the electromotive force (EMF) based estimation methods relying on the measurement of the stator voltages and currents for medium and high speed operations (Morimoto *et al.*, 2002; Chen *et al.*, 2003; Nahid-Mobarakeh *et al.*, 2007; Genduso *et al.*, 2010; Liu and Zhu, 2014a; Shinnaka, 2006; Chan *et al.*, 2008; Hasegawa and Matsui, 2009; Chi *et al.*, 2009; Zhao *et al.*, 2013; Wang *et al.*, 2013b, 2014; Zhao *et al.*, 2015a,b; Bolognani *et al.*, 1999; Kim and Kook, 1999; Boussak, 2005). The most straightforward way of obtaining the position information is to calculate the EMF or flux in open loop or simply estimating flux by integrating the EMF. However, the integration degrades due to the drift problem and is sensitive to machine phase resistance. In order to improve position estimation, the Back-EMF, extended EMF and flux were estimated by state observers (Morimoto *et al.*, 2002; Chen *et al.*, 2003; Nahid-Mobarakeh *et al.*, 2007; Genduso *et al.*, 2010; Liu and Zhu, 2014a; Shinnaka, 2006; Chan *et al.*, 2008; Hasegawa and Matsui, 2009), sliding mode observers (Chi *et al.*, 2009; Zhao *et al.*, 2013; Wang *et al.*, 2013b, 2014; Zhao *et al.*, 2015a,b) and extended Kalman Filters (Bolognani *et al.*, 1999; Kim and Kook, 1999; Boussak, 2005). In this section, the method employing extend EMFs in the estimated rotor reference frame (Morimoto *et al.*, 2002) is introduced in detail.

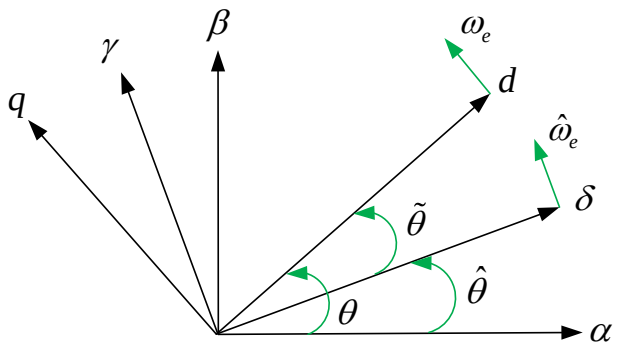


Figure 3.1: Different reference frames in IPMSM drives.

In sensorless field oriented control of permanent magnet motor drives, three reference frames shown in Figure 3.1 are normally utilized. The voltages and currents in the stationary reference frame ($\alpha$-$\beta$ frame) can be transformed to the rotor reference frame ($d$-$q$ frame) or the estimated rotor reference frame ($\delta$-$\gamma$ frame) by actual position $\theta$ or estimated position $\hat{\theta}$.

The fundamental frequency voltage equations of IPM motor in $d$-$q$ frame are shown in

$$\begin{bmatrix} u_d \\ u_q \end{bmatrix} = \begin{bmatrix} R_s & -\omega_e L_q \\ \omega_e L_d & R_s \end{bmatrix} \begin{bmatrix} i_d \\ i_q \end{bmatrix} + \begin{bmatrix} L_d & 0 \\ 0 & L_q \end{bmatrix} p \begin{bmatrix} i_d \\ i_q \end{bmatrix} + \omega_e \lambda_{pm} \begin{bmatrix} 0 \\ 1 \end{bmatrix}. \tag{3.1}$$

In EMF based methods, the rotor position can be obtained from the EMF or flux linkage due to the permanent magnets by using different kinds of observers. Particularly, the extended EMFs in $\delta$-$\gamma$ frame are utilized to extract the rotor position and speed at medium and high speed conditions (Morimoto *et al.*, 2002). If the square

matrice in (3.1) are written symmetrically, the voltage equations become

$$\begin{bmatrix} u_d \\ u_q \end{bmatrix} = \begin{bmatrix} R_s & -\omega_e L_q \\ \omega_e L_q & R_s \end{bmatrix} \begin{bmatrix} i_d \\ i_q \end{bmatrix} + \begin{bmatrix} L_d & 0 \\ 0 & L_d \end{bmatrix} p \begin{bmatrix} i_d \\ i_q \end{bmatrix} + \begin{bmatrix} 0 \\ E_{ext} \end{bmatrix}, \tag{3.2}$$

where the extended EMF $E_{ext}$ is represented as

$$E_{ext} = \omega_e \left[ (L_d - L_q) i_d + \lambda_{pm} \right] - (L_d - L_q) p i_q. \tag{3.3}$$

If the voltage equations are transformed into $\delta$-$\gamma$ frame, then the voltage equations change to

$$\begin{bmatrix} u_\delta \\ u_\gamma \end{bmatrix} = \begin{bmatrix} R_s & -\omega_e L_q \\ \omega_e L_q & R_s \end{bmatrix} \begin{bmatrix} i_\delta \\ i_\gamma \end{bmatrix} + \begin{bmatrix} L_d & 0 \\ 0 & L_d \end{bmatrix} p \begin{bmatrix} i_\delta \\ i_\gamma \end{bmatrix} + \begin{bmatrix} e_\delta \\ e_\gamma \end{bmatrix}. \tag{3.4}$$

The $e_\delta$ and $e_\gamma$ denote the extended EMF in $\delta$-$\gamma$ frame which are shown as

$$\begin{bmatrix} e_\delta \\ e_\gamma \end{bmatrix} = E_{ext} \begin{bmatrix} -\sin\tilde{\theta} \\ \cos\tilde{\theta} \end{bmatrix} + \tilde{\omega}_e L_d \begin{bmatrix} -i_\gamma \\ i_\delta \end{bmatrix}. \tag{3.5}$$

The $\tilde{\omega}_e$ denotes the speed estimation error and is calculated as $\tilde{\omega}_e = \omega_e - \hat{\omega}_e$. By assuming that the estimated speed is very close to the measured speed in steady state, the second components in (3.5) can be ignored.

Since the position information is contained in the extended EMF shown in (3.5), the extended EMFs need to be estimated in order to estimate the position and speed. A state observer is utilized for extended EMF estimation in $\delta$-$\gamma$ frame (Morimoto *et al.*, 2002). Figure 3.2 shows the structure of the observer in $\delta$ axis and a similar observer is also employed in $\gamma$ axis. Additionally, the state observer in Figure 3.2 can

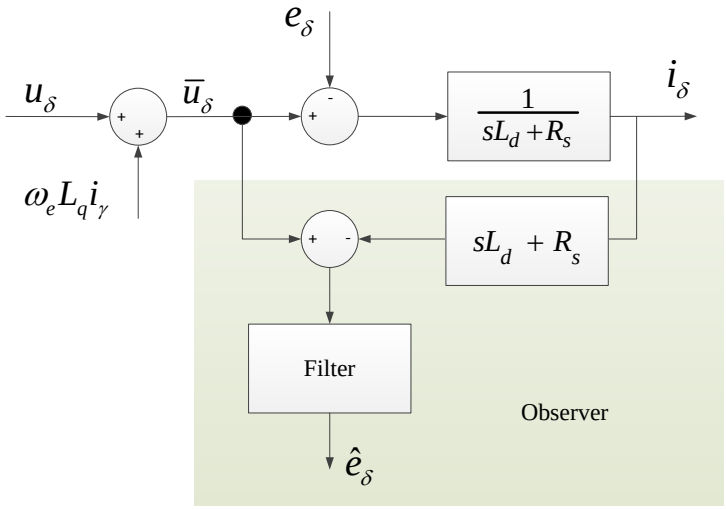


Figure 3.2: State observer for extended EMF in $\delta$ axis.

be replaced by Sliding Mode Observer and Extended Kalman Filter as well.

The state space equations of the extended EMF observers are

$$p\begin{bmatrix} i_\delta \\ e_\delta \end{bmatrix} = \frac{1}{L_d}\begin{bmatrix} -R_s & -1 \\ 0 & 0 \end{bmatrix}\begin{bmatrix} i_\delta \\ e_\delta \end{bmatrix} + \frac{1}{L_d}\begin{bmatrix} 1 \\ 0 \end{bmatrix}\bar{u}_\delta$$
$$p\begin{bmatrix} i_\gamma \\ e_\gamma \end{bmatrix} = \frac{1}{L_d}\begin{bmatrix} -R_s & -1 \\ 0 & 0 \end{bmatrix}\begin{bmatrix} i_\gamma \\ e_\gamma \end{bmatrix} + \frac{1}{L_d}\begin{bmatrix} 1 \\ 0 \end{bmatrix}\bar{u}_\gamma, \tag{3.6}$$

where the input voltages are compensated by $\bar{u}_\delta = u_\delta + \omega_e L_q i_\gamma$ and $\bar{u}_\gamma = u_\gamma - \omega_e L_q i_\delta$ to eliminate the cross coupling effect (Morimoto *et al.*, 2002).

The estimated extended EMF is represented as

$$\begin{bmatrix} \hat{e}_\delta \\ \hat{e}_\gamma \end{bmatrix} = E_{ext}\begin{bmatrix} -\sin\hat{\tilde{\theta}} \\ \cos\hat{\tilde{\theta}} \end{bmatrix} \tag{3.7}$$

and the estimated position estimation error is calculated as

$$\hat{\tilde{\theta}} = arctan\left(-\frac{\hat{e}_\delta}{\hat{e}_\gamma}\right). \tag{3.8}$$

The estimated position error can be processed with a Phase Locked Loop (PLL) which consists of a PI regulator and an integrator for speed and position estimation. The block diagram of the PLL is shown in Figure 3.3. The estimated speed is obtained directly from the PLL output. Assuming that the $\hat{\tilde{\theta}} = \theta - \hat{\theta}$, the close loop transfer function of the PLL from the actual position to the estimated one is represented in

$$\frac{\hat{\theta}}{\theta} = \frac{K_p s + K_i}{s^2 + K_p s + K_i}, \tag{3.9}$$

where $K_p$ and $K_i$ denote the proportional gain and the integral gain in the PI regulator. The PLL contains two integrations and the steady state error is zero with a ramp input (Dorf and Bishop, 2010). The $K_p$ and $K_i$ can be designed based on the PLL bandwidth requirements, but the theoretical numbers need to be adjusted heuristically by balancing the estimation bandwidth and noise attenuation (Morimoto *et al.*, 2002; Jeong *et al.*, 2005; Jang *et al.*, 2004; Al-nabi *et al.*, 2013).

Since the EMF components are proportional to the motor speed, the extraction of EMF is challenging at low speed condition. Moreover, the voltage drop due to the stator resistance and inverter nonlinearities also affect estimation performance of the EMF based methods at low speed.

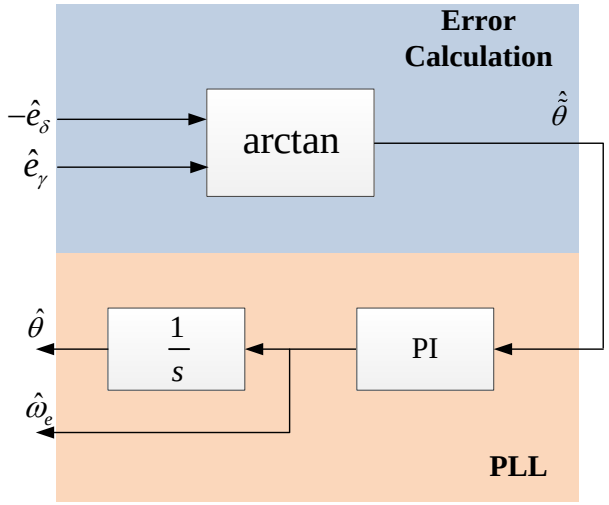


Figure 3.3: Extended EMF based position estimator.

## 3.3 Saliency Tracking Based Speed and Position Estimation

In order to achieve speed and position estimation at low speed, the saliency tracking based methods, which usually employ high frequency signal injection into different frames of the machine (Kim *et al.*, 2004; Jeong *et al.*, 2005; Bolognani *et al.*, 2011; Kim *et al.*, 2012; Aihara *et al.*, 1999; Jang *et al.*, 2004; Foo *et al.*, 2010; Gong and Zhu, 2013; Zaim *et al.*, 2014; Huang *et al.*, 2014; Yang, 2015; Noguchi *et al.*, 1998; Liu and Zhu, 2014b), are also widely utilized. These methods exploited the anisotropic property of IPM machines caused by spatial saliency or magnetic saturation. In (Kim *et al.*, 2004; Jeong *et al.*, 2005; Bolognani *et al.*, 2011; Kim *et al.*, 2012), rotating sinusoidal voltage signals were injected into stationary reference frame and the resulting carrier frequency currents were demodulated for extracting the rotor position information. Another major type of injection method is called pulsating voltage injection

method (Aihara *et al.*, 1999; Jang *et al.*, 2004; Foo *et al.*, 2010; Gong and Zhu, 2013). This method relied on injecting sinusoidal voltage signals into $\delta$ or $\gamma$ axis and the induced currents in $\gamma$ or $\delta$ axis was utilized for position estimation. Compared with rotating sinusoidal injection, the pulsating voltage injection has the benefits of simpler demodulation procedures and less torque ripples. Other injection types like square wave voltage injection (Zaim *et al.*, 2014; Huang *et al.*, 2014; Yang, 2015), sinusoidal current injection (Noguchi *et al.*, 1998) and pulsating voltage injection into stationary reference frame (Liu and Zhu, 2014b) were also applied for position sensing. Besides signal injection, methods relying on high frequency excitation by PWM switching (Schroedl, 1996; Petrovic *et al.*, 2003) were also employed for sensorless control of permanent magnet motor drives.

In this section, the pulsating sinusoidal voltage injection based method (Zhu and Gong, 2011; Gong and Zhu, 2013) is introduced as an example of the saliency tracking based methods. In signal injection based method, since the injection frequency is usually much higher than the fundamental frequency and the machine speed is low, the resistive voltage drop and EMF components can be ignored in the voltage equations. The high frequency voltage equations are rewritten as

$$\begin{bmatrix} u_{dh} \\ u_{qh} \end{bmatrix} = \begin{bmatrix} L_d & 0 \\ 0 & L_q \end{bmatrix} p \begin{bmatrix} i_{dh} \\ i_{qh} \end{bmatrix}, \tag{3.10}$$

where $u_{dqh}$ and $i_{dqh}$ represent the *d-q* frame voltages and currents in the injection frequency.

The transformation from $\delta$-$\gamma$ frame to $d$-$q$ frame is shown as

$$T(\tilde{\theta}) = \begin{bmatrix} \cos(\tilde{\theta}) & \sin(\tilde{\theta}) \\ -\sin(\tilde{\theta}) & \cos(\tilde{\theta}) \end{bmatrix}, \tag{3.11}$$

where the position error $\tilde{\theta}$ can be represented as $\tilde{\theta} = \theta - \hat{\theta}$.

The voltage equations in $\delta$-$\gamma$ frame can be obtained from (3.10) and (3.11), which is

$$\begin{bmatrix} u_{\delta h} \\ u_{\gamma h} \end{bmatrix} = T^{-1}(\tilde{\theta}) \begin{bmatrix} L_d & 0 \\ 0 & L_q \end{bmatrix} T(\tilde{\theta}) p \begin{bmatrix} i_{\delta h} \\ i_{\gamma h} \end{bmatrix}. \tag{3.12}$$

The above equations are further developed as

$$p \begin{bmatrix} i_{\delta h} \\ i_{\gamma h} \end{bmatrix} = \begin{bmatrix} \frac{1}{L_m} + \frac{1}{L_n}\cos(2\tilde{\theta}) & \frac{1}{L_n}\sin(2\tilde{\theta}) \\ \frac{1}{L_n}\sin(2\tilde{\theta}) & \frac{1}{L_m} - \frac{1}{L_n}\cos(2\tilde{\theta}) \end{bmatrix} \begin{bmatrix} u_{\delta h} \\ u_{\gamma h} \end{bmatrix}, \tag{3.13}$$

where $L_m = 2L_dL_q/(L_d + L_q)$ and $L_n = 2L_dL_q/(L_q - L_d)$.

In the proposed method, the high frequency voltage is injected in $\delta$ axis. The injected voltages are mathematically represented as

$$\begin{bmatrix} u_{\delta h} \\ u_{\gamma h} \end{bmatrix} = V_h \begin{bmatrix} \cos(\omega_h t) \\ 0 \end{bmatrix}, \tag{3.14}$$

where $V_h$ and $\omega_h$ represent the magnitude and frequency of the injected voltage.

Combining (3.13) and (3.14), the resulting currents in the injection frequency are

developed as

$$\begin{bmatrix} i_{\delta h} \\ i_{\gamma h} \end{bmatrix} = \begin{bmatrix} I_1 + I_2 \cos(2\tilde{\theta}) \\ I_2 \sin(2\tilde{\theta}) \end{bmatrix} \sin(\omega_h t), \tag{3.15}$$

where $I_1 = V_h/(\omega_h L_m)$ and $I_2 = V_h/(\omega_h L_n)$.

From (3.15), it is easy to see that the position information $\tilde{\theta}$ is contained both in $i_{\delta h}$ and $i_{\gamma h}$. In order to obtain the position information, a demodulation method containing a band-pass filter (BPF) and a low-pass filter (LPF) is utilized for processing the resulting current in $\gamma$ axis, as shown in Figure 3.4. First of all, the BPF is used for extracting $i_{\gamma h}$ from $i_\gamma$. Then the multiplication of $\sin(\omega_h t)$ is applied to the output of the BPF. Finally, a LPF is used to eliminate the high frequency components in the obtained signal. A function containing the position error is extracted at the output of the LPF, which is represented as

$$f(\tilde{\theta}) = \frac{1}{2} I_2 \sin(2\tilde{\theta}). \tag{3.16}$$

Similar to the extended EMF based method, a PLL is also used for estimating the speed and position in the demodulation based position estimator. When $\tilde{\theta}$ is small enough, $sin(2\tilde{\theta}) \approx 2\tilde{\theta}$. So $f(\tilde{\theta})$ can be applied as the input of the PLL and the outputs are the estimated speed and position.

The saliency tracking based methods are parameter independent and suitable for low speed operations including standstill conditions. However, larger torque ripples and extra losses are introduced in these methods due to the superimposition of extra signals on the fundamental frequency components. Additionally, the control bandwidth is limited due to demodulation of the carrier frequency current components in

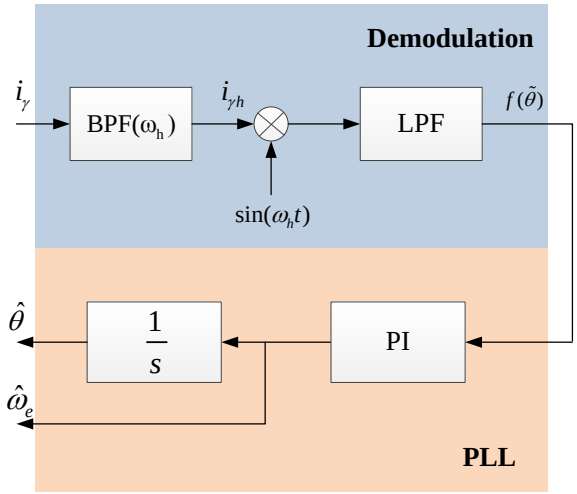


Figure 3.4: Demodulation based position estimator.

the position estimator.

## 3.4 Speed and Position Estimation at Wide Speed Range

The combination of the EMF based methods and saliency tracking based methods is a widely employed solution for applying sensorless control algorithms on PMSM drives at wide speed range operations. At low speed, the saliency tracking based methods are employed. The EMF based estimation methods take over at medium and high speed conditions. During the transition between low speed and medium speed, several combination algorithms were proposed. In (Silva *et al.*, 2006; Bisheimer *et al.*, 2010; Andreescu *et al.*, 2008), variable observer structures or gains were applied at different speed ranges. In (Wang *et al.*, 2013a; Ma *et al.*, 2013; Bolognani *et al.*, 2012), a linear blending combination was proposed between EMF based methods and saliency

tracking based methods during the switching process, which is shown in this section.

As shown in Figure 3.5, two speed boundaries are selected as $N_1$ and $N_2$. If the machine speed is lower than $N_1$, only the estimated speed and position from the pulsating voltage injection method are used. If the machine speed is higher than $N_2$, only the estimated speed and position from the extended EMF based method are employed. If the motor speed is between $N_1$ and $N_2$ , then the final estimated speed and position are the linear combinations of speeds and positions estimated by both methods. The relationship is shown in (3.17) and (3.18), where $\hat{N}$ denotes the estimated speed in rpm.

$$\hat{\theta} = \begin{cases} \hat{\theta}_{low} & \left|\hat{N}\right| \leq N_1 \\ \hat{\theta}_{high} & \left|\hat{N}\right| \geq N_2 \\ \frac{N_2 - \left|\hat{N}\right|}{N_2 - N_1}\hat{\theta}_{low} + \frac{\left|\hat{N}\right| - N_1}{N_2 - N_1}\hat{\theta}_{high} & N_1 < \left|\hat{N}\right| < N_2 \end{cases} \tag{3.17}$$

$$\hat{\omega} = \begin{cases} \hat{\omega}_{low} & \left|\hat{N}\right| \leq N_1 \\ \hat{\omega}_{high} & \left|\hat{N}\right| \geq N_2 \\ \frac{N_2 - \left|\hat{N}\right|}{N_2 - N_1}\hat{\omega}_{low} + \frac{\left|\hat{N}\right| - N_1}{N_2 - N_1}\hat{\omega}_{high} & N_1 < \left|\hat{N}\right| < N_2 \end{cases} \tag{3.18}$$

The block diagram of the combined sensorless control system is shown in Figure 3.6. Two position estimators and two PLLs are needed in the combined system, which increases the system complexity. This combined algorithm was implemented in the experimental test bench as a benchmark reference for the proposed unified method.

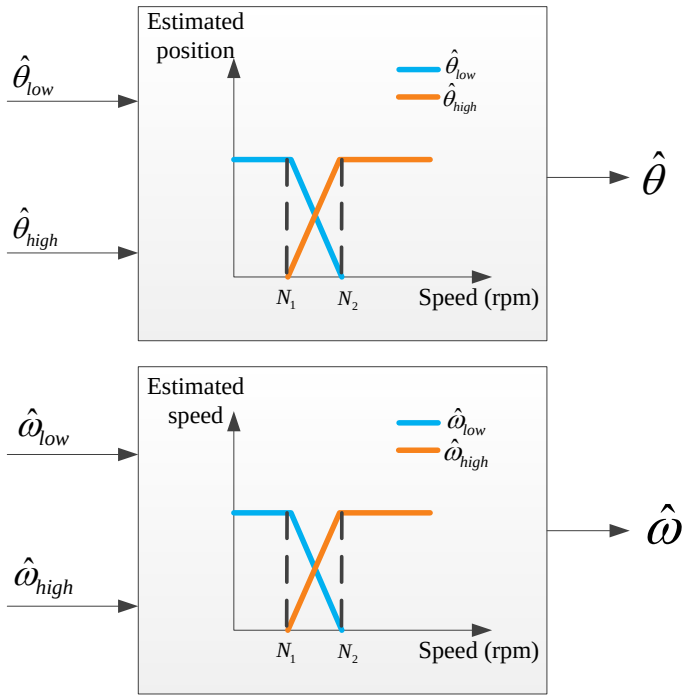


Figure 3.5: Linear blending algorithm for speed and position combination.

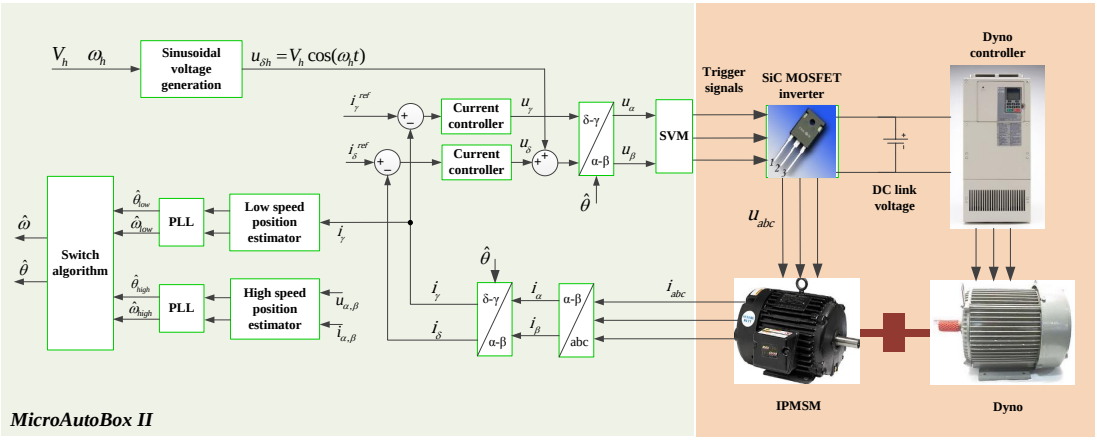


Figure 3.6: Block diagram of the sensorless control system with combined algorithms.

## 3.5 Initial Position Estimation

The function of position error shown in (3.16) implies that only $2\tilde{\theta}$ is available for the low speed position estimator. So the estimated position will have an ambiguity of 180°, which implies that the initial position and the magnetic polarity need to be identified at the machine startup. According to the literature, the existing starting procedures can be classified into three categories: (1). Physical alignment of the rotor magnetic axis ($d$ axis) in the direction of a fixed stator magnetic field generated by a DC current excitation; (2). Starting the rotor with a rotating stator magnetic field in open loop; (3). Detection of stator inductance variations by different estimation algorithms (Tursini *et al.*, 2003; Antonello *et al.*, 2015).

The first procedure can be achieved by simply imposing a constant voltage vector to the inverter to align $d$ axis to a specific phase direction. However, the application of this method is restricted by the presence of load torque and the availability of movement of the mechanical system. The second procedure aims at rotating the machine in open loop with specific rotating magnetic field until the machine back-emf (proportional to the machine speed) is sufficiently large for position estimation. Nevertheless, only limited torque is allowed at startup if this procedure is employed (Tursini *et al.*, 2003; Chen *et al.*, 2003; Genduso *et al.*, 2010; Antonello *et al.*, 2015).

The existing initial position estimation algorithms are mostly concentrating on estimating the rotor position by identifying the location of the minimum stator inductance. Besides the continuous signal injection introduced in Section 3.2, the pulse voltage injection based methods (Antonello *et al.*, 2015; Schroedl, 1996; Nakashima *et al.*, 2000; Tursini *et al.*, 2003; Khlaief *et al.*, 2012) were also employed for initial position estimation.

### 3.5.1 Short Pulse Voltage Injection for Initial Position Estimation

Different with the continuous injection, pulse voltage signals can be utilized for identifying the initial position as well. The basic idea of these methods is searching for the minimum inductance location by measuring the peak current responses due to the injected short pulse voltage vectors applied along different directions with respect to the stator (Antonello *et al.*, 2015). The higher $di/dt$ indicates a smaller inductance along that direction. In (Nakashima *et al.*, 2000), twenty-one voltage vectors were applied in different directions along the stator in order to find the minimum inductance location which indicates the orientation of $d$ axis. In (Schroedl, 1996; Tursini *et al.*, 2003; Khlaief *et al.*, 2012), three voltage vectors were injected among three phases and the induced peak phase current responses were recorded for position estimation. The mathematical function $arctan$ is applied for calculating the position in (Schroedl, 1996) and a complicated table was used in (Khlaief *et al.*, 2012) to calculate the position by using $\arctan(\theta) \approx \theta$ approximately.

In (Boussak, 2005; Khlaief *et al.*, 2012), voltage pulses were injected in phase A, B and C respectively by applying gate signals V(100), V(010) and V(001) to the voltage source inverter directly and the current peaks were recorded for position estimation. The injection scheme is shown in Figure 3.7.

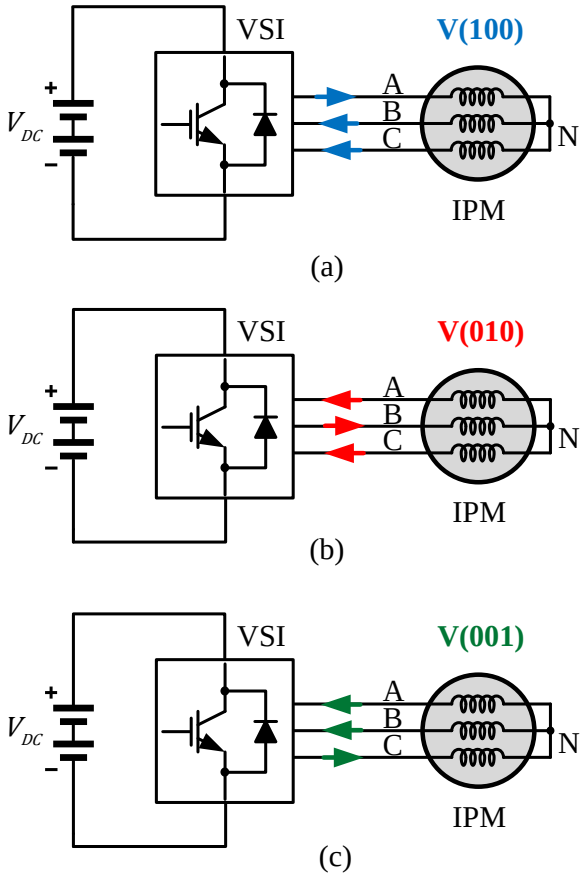


Figure 3.7: Applied voltage vectors for initial position estimation.

In one electrical period, the phase current peaks $I_a$, $I_b$ and $I_c$ are sinusoidal functions of the rotor position shown as

$$\begin{aligned} I_a &= I_0 + \Delta I_a = I_0 + \Delta I_0 \cos(2\theta_{int}) \\ I_b &= I_0 + \Delta I_b = I_0 + \Delta I_0 \cos(2\theta_{int} - \frac{2\pi}{3}) \\ I_c &= I_0 + \Delta I_c = I_0 + \Delta I_0 \cos(2\theta_{int} + \frac{2\pi}{3}), \end{aligned} \tag{3.19}$$

where $I_0 = (I_a + I_b + I_c)/3$ and $\Delta I_0$ denote the DC current offset and the magnitude of

Table 3.1: Initial Position Estimation

| Sign ($\Delta I_a$) | Sign ($\Delta I_b$) | Sign ($\Delta I_c$) | Estimated initial position $\theta_{int}$ |
|---|---|---|---|
| + | - | - | $\in [-15°15°]$ or $\in [165°195°]$ |
| + | + | - | $\in [15°45°]$ or $\in [195°225°]$ |
| - | + | - | $\in [45°75°]$ or $\in [225°255°]$ |
| - | + | + | $\in [75°105°]$ or $\in [255°285°]$ |
| - | - | + | $\in [105°135°]$ or $\in [285°315°]$ |
| + | - | + | $\in [135°165°]$ or $\in [315°345°]$ |

the fluctuated components. The current differences $\Delta I_a$, $\Delta I_b$ and $\Delta I_c$ are calculated as $\Delta I_a = I_a - I_0$, $\Delta I_b = I_b - I_0$ and $\Delta I_c = I_c - I_0$ respectively. Based on (3.19), the relationship among phase current differences is shown in

$$\tan 2\theta_{int} = \frac{\sqrt{3}(\Delta I_b - \Delta I_c)}{2\Delta I_a - \Delta I_b - \Delta I_c}. \tag{3.20}$$

The initial rotor position is then calculated as

$$\theta_{int} = \frac{1}{2} arctan(\frac{\sqrt{3}(\Delta I_b - \Delta I_c)}{2\Delta I_a - \Delta I_b - \Delta I_c}). \tag{3.21}$$

The range of $arctan(2\theta_{int})$ is between $[-90°\ 90°]$, then the detected initial position $\theta_{int}$ is within $[-45°\ 45°]$, which leads to an ambiguity of 90° electrical degree in the estimation results. In order to solve this problem, Table 3.1 was also used for identify the initial position.

With (3.21) and Table 3.1, the estimated initial position still contains an ambiguity of 180° as in the sinusoidal injection based method. This ambiguity can be eliminated by utilizing magnetic polarity detection, which is going to be introduced in Section 3.5.2.

### 3.5.2 Magnetic Polarity Detection

The spatial saliency of the IPM machine performs two periods in one electric cycle. The position estimation results contain an ambiguity of 180°, which leads to the reverse rotation of the machine shaft. In order to detect the magnetic polarity, several methods have been proposed in the literature (Kim *et al.*, 2004; Jeong *et al.*, 2005; Kondo *et al.*, 1995; Aihara *et al.*, 1999; Khlaief *et al.*, 2012; Noguchi *et al.*, 1998; Murakami *et al.*, 2012; Gong and Zhu, 2013). In (Kim *et al.*, 2004; Jeong *et al.*, 2005), the second order components of the induced high frequency currents were demodulated for polarity detection. The robustness of the secondary harmonic based method is limited due to the small magnitude of the second order components. In (Kondo *et al.*, 1995; Aihara *et al.*, 1999; Khlaief *et al.*, 2012; Noguchi *et al.*, 1998; Murakami *et al.*, 2012; Gong and Zhu, 2013), the magnetic saturation of the stator core was used for determining the location of the north magnetic pole. The decrease of $d$ axis inductance can be reflected in the increase of current response, both in $d$-$q$ inductances and phase inductances (Kondo *et al.*, 1995; Aihara *et al.*, 1999; Khlaief *et al.*, 2012). The voltage reference oscillations of the current controller due to saturation were observed for polarity detection in (Noguchi *et al.*, 1998) and the magnetic hysteresis phenomenon was utilized for identifying magnetic north pole in (Murakami *et al.*, 2012). Both methods were not straightforward for real time implementation. In (Gong and Zhu, 2013), the saturation based polarity detection algorithm was applied in the running state as well as standstill conditions while the detection time was relatively long. In these methods, the need for magnetic saturation of the stator iron may lead to a high current for polarity detection in some machines, which requires inverters with higher power rating to ensure robust detection of magnetic polarity.

In this chapter, the dual voltage injection based polarity detection method (Gong and Zhu, 2013; Kondo *et al.*, 1995; Aihara *et al.*, 1999) is introduced in detail. In this method, dual voltage pulses were injected in estimated $d$ axis after the location of the magnetic axis had been estimated. The pulse aligned with the north magnetic pole increases the magnetization of the stator core and leads to a smaller $L_d$. The other voltage pulse aligned with the south pole decreases the magnetization of the stator core and results in a larger $L_d$. As shown in Figure 3.8, if a pair of dual voltage pulses with the same magnitude and inverse directions ($V_{pul}^{pos} = V_{pul}^{neg}$) is injected in estimated $d$ axis, the difference between peak current values of the resulting currents can be employed for determining the magnetic polarity. The direction of the voltage pulse with higher current response indicates the direction of the magnetic north pole (Gong and Zhu, 2013). In Figure 3.8, if the positive direction of the estimated $d$ axis aligns with the north magnetic pole, $I_{peak}^{pos}$ should be larger than $I_{peak}^{neg}$. Otherwise the positive direction of the estimated $d$ axis aligns with the south magnetic pole and the compensation of 180° is needed. The framework of the dual voltage injection based polarity detection method is illustrated in Figure 3.9. Since this inductance variation is also reflected in the phase inductances, the magnetic polarity can be detected by observing the phase currents as well (Boussak, 2005; Khlaief *et al.*, 2012).

## 3.6 Conclusions

This chapter reviews the existing speed and position estimation algorithms at stand-still, low speed and high speed conditions. The pulsating voltage injection based method, the extended EMF based method and their combination are explained in detail at running state. Those above mentioned methods were implemented in the

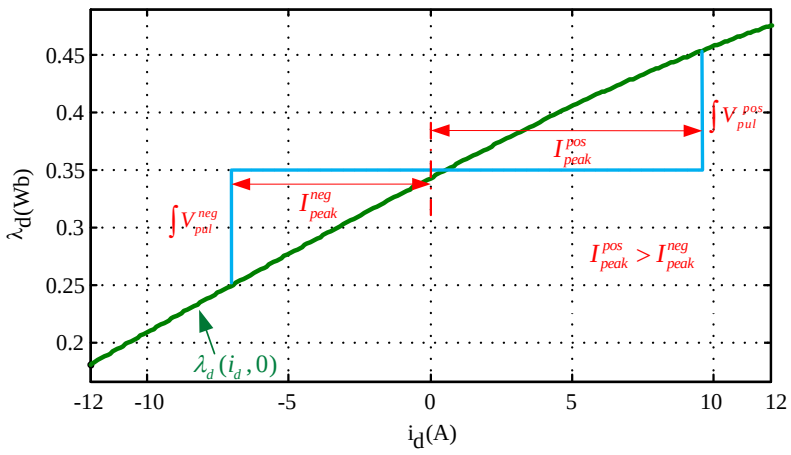


Figure 3.8: Dual voltage injection based method for magnetic polarity detection.

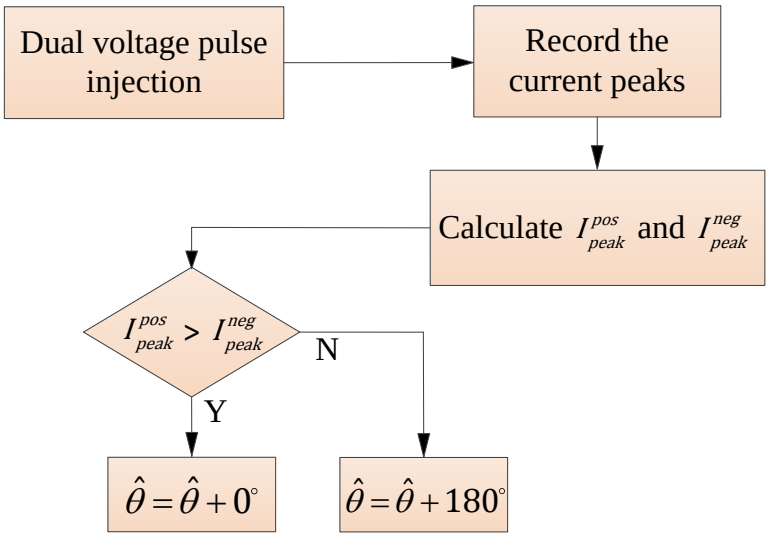


Figure 3.9: Framework of the dual voltage pulse injection based method

prototype IPMSM drive system as benchmark reference of the proposed optimization based sensorless algorithms. For initial position estimation, both the sinusoidal injection and short pulse injection can be utilized. Since the machine saliency performs two periods in one electrical cycle, the magnetic polarity detection is indispensable for obtaining the positive direction of the magnetic axis. The existing short pulse injection based initial position estimation methods and polarity detection methods have been introduced in this chapter. The detailed comparisons between the existing methods and the proposed methods will be presented in Chapter 7.

# Chapter 4

# Novel Nonlinear IPM Motor Model

## 4.1 Introduction

Machine models are instrumental in the analysis of the performance and tuning of the parameters of position estimation algorithms prior to actual experimental validation. The typical machine model assumes constant parameters and is widely used for such purposes. However, this machine model is not suitable for position estimation especially for polarity detection, because of their inaccuracies and their inability to model nonlinearities, which are caused by the saturation and cross-saturation effects. Therefore, Look-up tables (LUTs) relating current to inductance or flux linkage are commonly employed for nonlinear machine modeling. The look-up tables of the prototype IPM machine were measured experimentally with typical motor drive components. However, the use of the derivative of flux in the machine dynamics often gives rise to oscillations and can reduce the accuracy of the transient response, when using those look-up tables. Therefore, an improved method for implementing the nonlinear machine model is introduced in this chapter and is used for investigating

Table 4.1: Parameters of Prototype IPM Motor Drives

| Parameter | Value |
|---|---|
| Rated power $P_r$ | 5 $KW$ |
| Rated speed $N_r$ | 1800 $rpm$ |
| Number of pole pairs $P$ | 5 |
| Rated voltage (L-L) $V_r$ | 460 $V$ |
| Rated current $I_r$ | 9.4 $A$ |
| Rated torque $T_r$ | 29.7 $Nm$ |
| d axis inductance $L_d$ | 10.5 $mH$ |
| q axis inductance $L_q$ | 12.9 $mH$ |
| Stator resistance $R_s$ | 400 $m\Omega$ |
| PM flux $\lambda_{pm}$ | 343.05 $mWb$ |
| Shaft friction $B$ | $1.3 \times 10^{-3}$ $Nms$ |
| Shaft inertia $J_i$ | 13 $\times 10^{-3}$ $kgm^2$ |

the performance of the proposed speed and position estimation algorithms at stand-still and running state. Additionally, the components of the prototype IPMSM drive system are also briefly introduced in this chapter.

## 4.2 Novel Nonlinear Model of the Prototype IPM Motor

### 4.2.1 Nonlinear Flux Linkage and Inductance Profiles

Typical machine model with constant $L_d$ and $L_q$ values was widely used in simulation analysis of the machine drive system. This model is based on the dynamic equations in *d-q* frame, which was shown in (3.2). The motor parameters of the prototype IPM motor provided by the manufacturer are listed in Table 4.1.

However, this linear dependent assumption is not accurate when the machine is saturated. In order to accurately model the nonlinearity of the IPM motors, the nonlinear flux linkage profiles need to be implemented. These profiles are either obtained from finite element analysis software or from experimental measurements and they are usually implemented as look-up tables in the nonlinear machine model. Dynamic equations of the nonlinear machine model are

$$\begin{aligned} u_d &= R_s i_d + \frac{d\lambda_d(i_{dq})}{dt} - \omega_e \lambda_q(i_{dq}) \\ u_q &= R_s i_q + \frac{d\lambda_q(i_{dq})}{dt} + \omega_e \lambda_d(i_{dq}), \end{aligned} \tag{4.1}$$

where $\lambda_d(i_{dq}) = \ell_d(i_{dq})$ and $\lambda_q(i_{dq}) = \ell_q(i_{dq})$ represent the flux linkage profiles in $d$-$q$ frame.

The time derivative of the flux linkage is

$$\frac{d\lambda_{dq}(t)}{dt} = \nabla_{i_{dq}} \ell_{dq}\big(i_{dq}(t)\big) \frac{di_{dq}(t)}{dt} = \begin{bmatrix} \frac{\partial \ell_d(i_{dq}(t))}{\partial i_d(t)} & \frac{\partial \ell_d(i_{dq}(t))}{\partial i_q(t)} \\ \frac{\partial \ell_q(i_{dq}(t))}{\partial i_d(t)} & \frac{\partial \ell_q(i_{dq}(t))}{\partial i_q(t)} \end{bmatrix} \frac{di_{dq}(t)}{dt}, \tag{4.2}$$

where the components $\frac{\partial \ell_d(i_{dq}(t))}{\partial i_d(t)}$ and $\frac{\partial \ell_q(i_{dq}(t))}{\partial i_q(t)}$ represent the flux saturation effect caused by the current in the same axis. The other two components $\frac{\partial \ell_d(i_{dq}(t))}{\partial i_q(t)}$ and $\frac{\partial \ell_q(i_{dq}(t))}{\partial i_d(t)}$ denote the cross magnetizing (saturation) effect which is induced by the currents in the other axis in $d$-$q$ frame (Xie and Ramshaw, 1986; El-Serafi *et al.*, 1988).

The component $\nabla_{i_{dq}}\ell_{dq}\big(i_{dq}(t)\big)$ in (4.2) is further developed as

$$\nabla_{i_{dq}}\ell_{dq}\big(i_{dq}(t)\big) = \begin{bmatrix} \frac{\partial \ell_d(i_{dq}(t))}{\partial i_d(t)} & \frac{\partial \ell_d(i_{dq}(t))}{\partial i_q(t)} \\ \frac{\partial \ell_q(i_{dq}(t))}{\partial i_d(t)} & \frac{\partial \ell_q(i_{dq}(t))}{\partial i_q(t)} \end{bmatrix} = \begin{bmatrix} \ell_{dd}\big(i_{dq}(t)\big) & \ell_{dq}\big(i_{dq}(t)\big) \\ \ell_{qd}\big(i_{dq}(t)\big) & \ell_{qq}\big(i_{dq}(t)\big) \end{bmatrix}, \tag{4.3}$$

where the $\ell_{dd}\big(i_{dq}(t)\big)$ and $\ell_{qq}\big(i_{dq}(t)\big)$ are the nonlinear differential self-inductance profiles. The $\ell_{dq}\big(i_{dq}(t)\big)$ and $\ell_{qd}\big(i_{dq}(t)\big)$ represent the nonlinear differential cross-coupling inductance profiles in *d-q* frame respectively (Štumberger *et al.*, 2003). Those nonlinear inductance profiles are used for initial position estimation mentioned in Section 7.2.

### 4.2.2 Measurements of the Nonlinear Look-up Tables

In this thesis, the nonlinear flux linkage profiles $\lambda_d(i_{dq})$ and $\lambda_q(i_{dq})$ were measured experimentally by utilizing the method mentioned in (Cintron-Rivera *et al.*, 2012). At steady state, the relationship between the flux linkages and currents in *d-q* frame is shown in

$$\begin{aligned} \lambda_d(i_{dq}) &= \frac{u_q - R_s i_q}{\omega_e} \\ \lambda_q(i_{dq}) &= -\frac{u_d - R_s i_d}{\omega_e}. \end{aligned} \tag{4.4}$$

If the motor is running at a constant speed, the flux linkages under different currents can be calculated from the steady state voltages. The relationship between the flux and current is recorded as 3D LUTs. Figure 4.1 and Figure 4.2 illustrate the experimental measured *d-q* frame nonlinear flux linkage profiles of the prototype IPM motor.

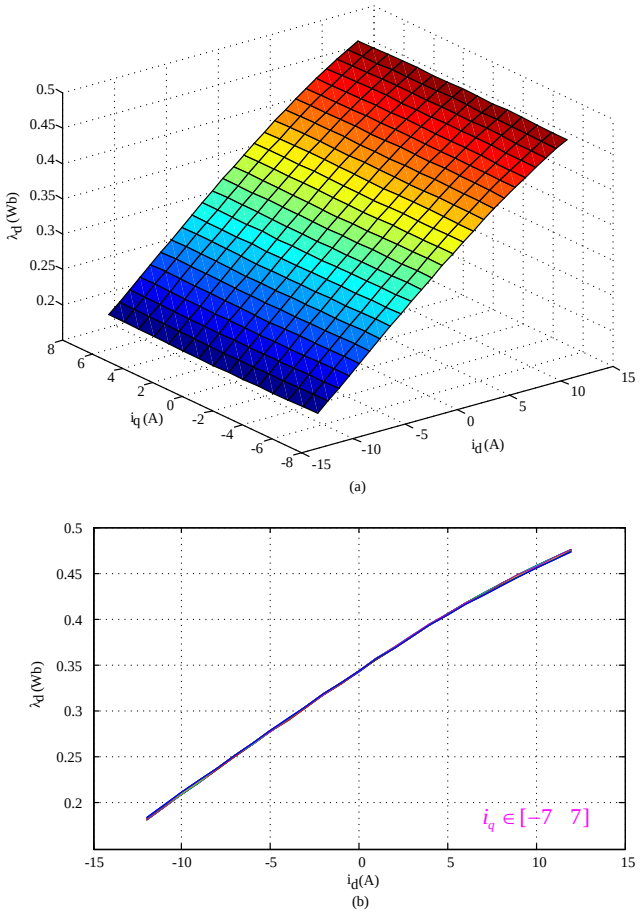


Figure 4.1: Experimental measured $d$ axis flux linkage profile $\lambda_d(i_{dq})$ under different $i_d$ and $i_q$.

### 4.2.3 Nonlinear IPM Motor Model with Inverted LUTs

As evident from the above equations, the derivatives of the flux linkage profiles are needed in the implementation of the machine model, which can introduce oscillations in the transients. If these profiles can be inverted to current profiles $i_d(\lambda_{dq})$ and $i_q(\lambda_{dq})$, only integration is needed in the implementation of the motor dynamic equations, hence avoiding numerical issues related to taking numerical derivatives. However, these inverse LUTs can not be obtained directly from experiment because currents

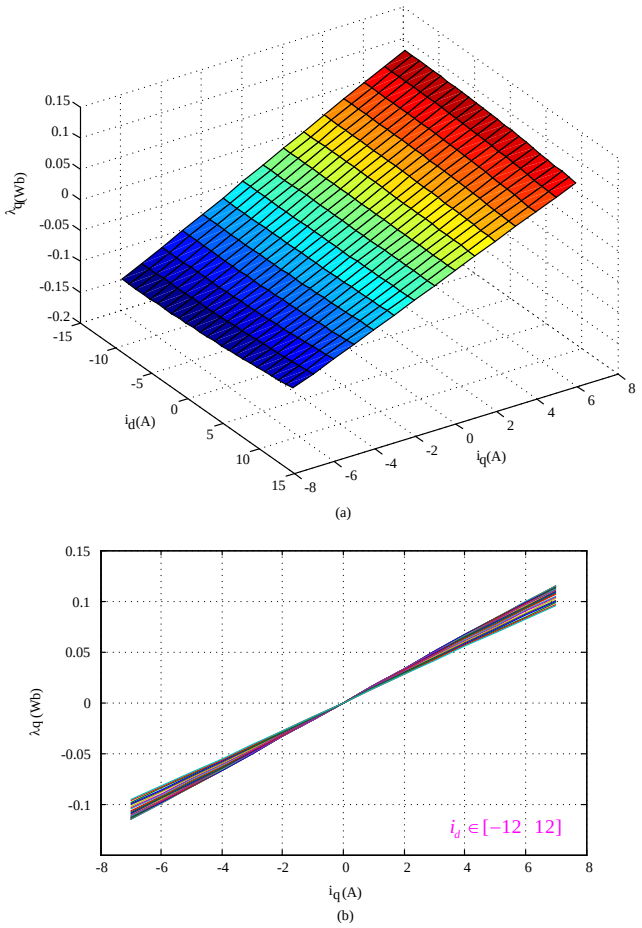


Figure 4.2: Experimental measured $q$ axis flux linkage profile $\lambda_q(i_{dq})$ under different $i_d$ and $i_q$.

are commonly applied in the motor drive system instead of flux. In order to solve this problem, a novel method of inverting look-up tables has been proposed. Figure 4.3 shows the flowchart of the proposed look-up table inversion algorithm, which involves the following steps:

1. The functions $\lambda_{dq}$=$\ell(i_{dq})$ can be obtained by interpolating the original look-up tables.

2. The obtained functions are used in calculating the inverse look-up tables. The

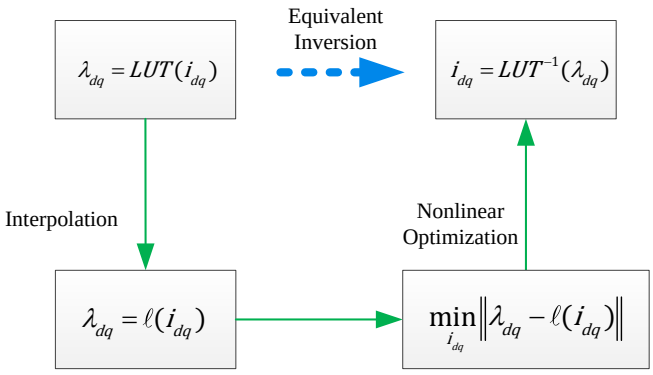


Figure 4.3: Flowchart of look-up table inversion algorithm

inversion is a least squares problem which can be solved with nonlinear numerical solvers.

3. The returned current values together with the input flux linkage values are recorded in the form of look-up tables.

By following the above procedures, the inverse look-up tables $i_{dq} = LUT^{-1}(\lambda_{dq})$ can be obtained and Figure 4.4 shows the inverse LUTs derived from nonlinear flux linkage profiles of the prototype IPM motor.

Figure 4.5 depicts the block diagram of the nonlinear motor model dynamics. The dynamic equations now can be rewritten in the discrete form as

$$\begin{bmatrix} \lambda_d(k+1) \\ \lambda_q(k+1) \end{bmatrix} = \begin{bmatrix} 1 & T_s\omega_e(k) \\ -T_s\omega_e(k) & 1 \end{bmatrix} \begin{bmatrix} \lambda_d(k) \\ \lambda_q(k) \end{bmatrix} + T_s \begin{bmatrix} u_d(k) \\ u_q(k) \end{bmatrix} - T_s R_s \begin{bmatrix} i_d(k) \\ i_q(k) \end{bmatrix}, \quad (4.5)$$

where $\lambda_{dq}(k+1)$ denotes the $d$-$q$ axes flux linkages in current sample time. The $\lambda_{dq}(k)$, $u_{dq}(k)$, $i_{dq}(k)$ and $\omega_e(k)$ represent the flux linkages, voltages, currents and electrical speed in the previous sample time. The $T_s$ represents the sampling time. The $A(\omega_e)$ matrix in Figure 4.5 is represented as $A(\omega_e) = (I - \omega_e(k)T_sY)$, where

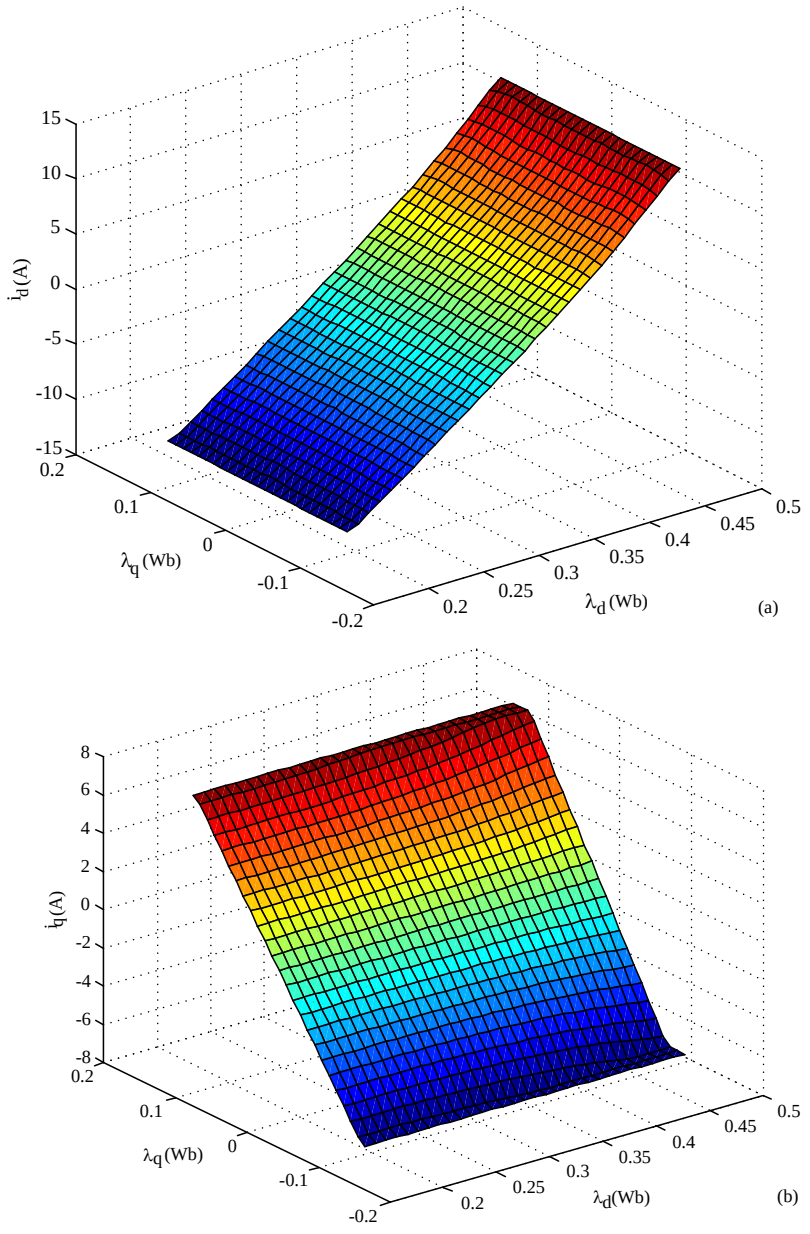


Figure 4.4: Inverted look-up tables: (a) The inverted profile $i_d(\lambda_{dq})$; (b) The inverted profile $i_q(\lambda_{dq})$.

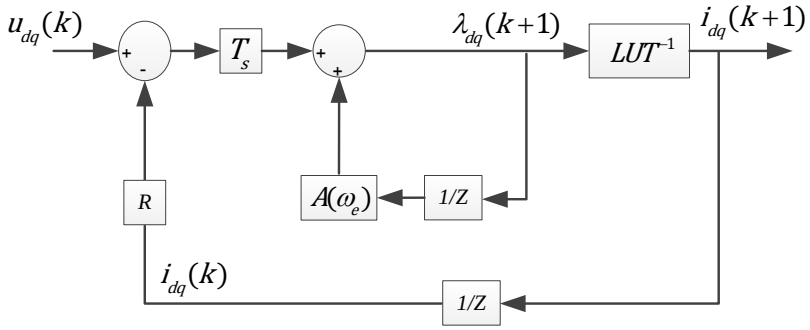


Figure 4.5: Block diagram of the nonlinear machine model dynamics with inverse LUTs.

$I$ is the identity matrix and $Y = \begin{bmatrix} 0 & -1 \\ 1 & 0 \end{bmatrix}$. The dynamic equations in (4.5) avoid numerical differentiation of the flux values and hence improve numerical behaviors.

## 4.3 Experimental Test Bench of Prototype IPM Motor Drives

In order to validate the proposed speed and position estimation algorithms in this thesis, an IPMSM drives test bench was set up in the laboratory, which is shown in Figure 4.6. The Silicon Carbide MOSFET inverter and the MicroAutoBox II are used for driving the prototype IPM motor. The YASKAWA A-1000 AC Drives is employed as the controller of the 5 KW dyno induction machine.

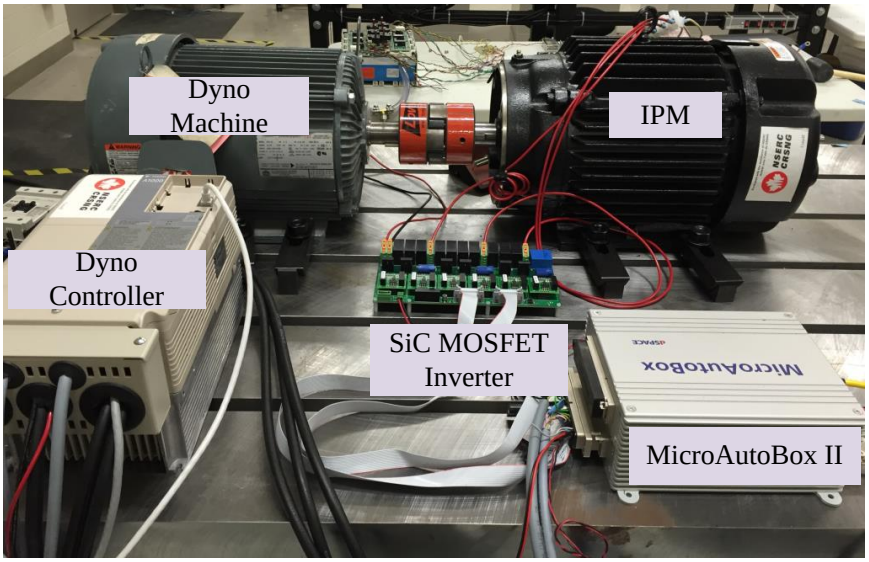


Figure 4.6: Prototype IPMSM drives test bench.

### 4.3.1 Silicon Carbide MOSFET Inverter

In recent years, the wide-bandgap semiconductors devices, such as silicon carbide (SiC), are being more considered in the AC motor drives in the automobile industry. The SiC semiconductors outperform with their fast switching capability, which reduces the interlock time. Moreover, using high frequency SiC power devices in the AC motor drives make it possible to operate the drive system with higher PWM frequency, which increases the control system bandwidth. Additionally, it reduces the values of inductors and capacitors used in the power inverter, which lead to a smaller inverter size compared with the silicon semiconductor based counterparts (Shirabe *et al.*, 2014; Zhang *et al.*, 2015).

In the prototype motor drive test bench, a 30 KW SiC MOSFET inverter shown in Figure 4.7 is utilized in the drive system. The rated DC link voltage of the inverter is 800 V and the rated output phase current is 30 A. The maximum switching frequency

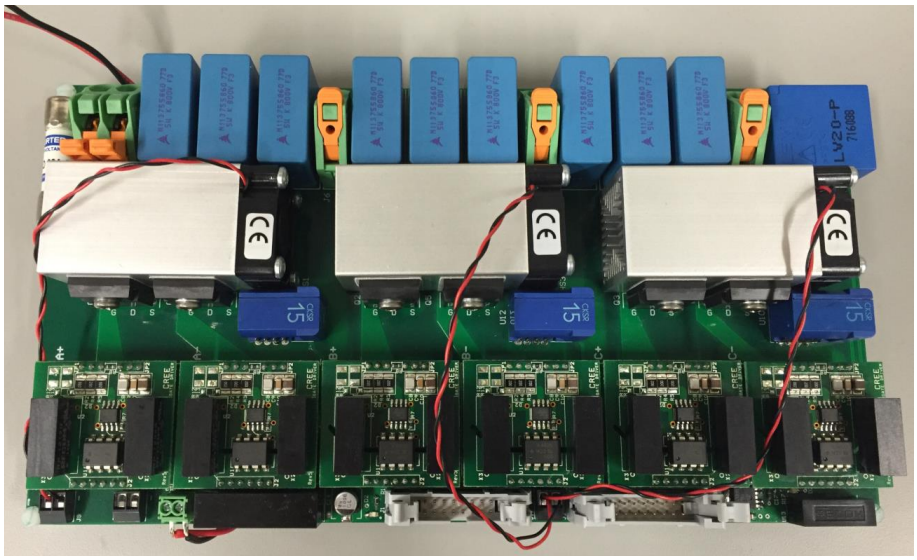

Figure 4.7: Prototype SiC MOSFET inverter.

is up to 100 KHz (Eull *et al.*, 2016).

### 4.3.2 MicroAutoBox II

MicroAutoBox II is the second generation of dSPACE's professional and robust standalone prototyping unit which provides universal development system for automobile applications and other industrial applications. It's capable of operating without user intervention (like an ECU) and can be applied for many fast response control prototyping applications such as powertrain, chassis control, body control and electric drives control, etc (dSPACE GmbH, 2013).

The MicroAutoBox II used in the prototype motor drive system consists of the DS1401 base board and I/O board 1512/1513. The built in Real Time Interface (RTI) library provides the link between MicroAutoBox II and the development software Matlab/Simulink. It provides a blockset that implements the functionality and

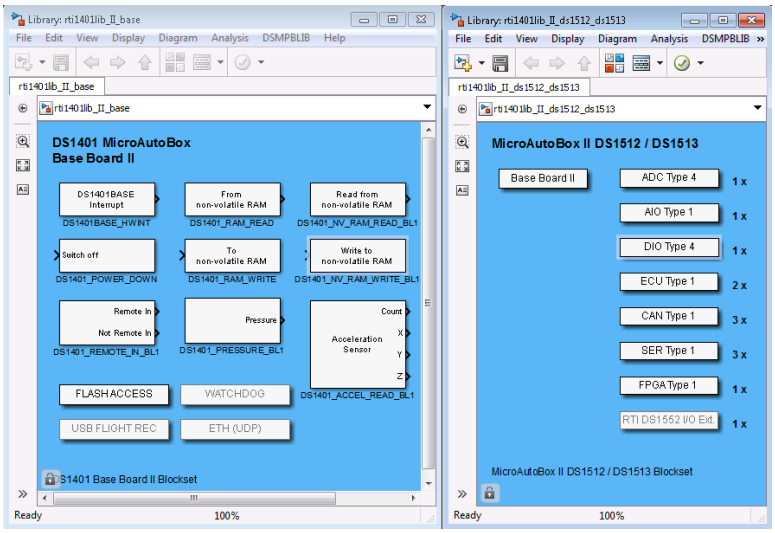


Figure 4.8: RTI Blockset in Simulink.

I/O capability of MicroAutoBox II in the Simulink model (dSPACE GmbH, 2013; dSPACE, 2014) . The RTI of DS1401/1512/1513 is shown in Figure 4.8. Figure 4.9 shows the working environment of the prototype motor control system using the experimental software ControlDesk Next Generation.

### 4.3.3 Dyno Machine Controller

The YASKAWA A-1000 Drive is utilized as the dyno induction machine controller in the prototype motor drive system. The A-1000 Drive is a full featured drive which provides close loop and open loop vector control for both permanent magnet machine and induction machine (YASKAWA, 2014). The control mode can be switched among speed control, torque control and position control easily and the control reference signals can be received via CAN, USB and analog input. In the prototype drive system, the induction machine is controlled in speed mode and the speed reference is the analog signal transmitted from MicroAutoBox II to A-1000. In this way, the


Figure 4.9: Experimental software ControlDesk Next Generation.

speed and torque references of the two motors are both provided by ControlDesk simultaneously.

### 4.3.4 High Accuracy Position Sensor

High accuracy position sensors are necessary for providing accurate measurements of the actual speed and position in validation of the sensorless methods. Hence, a fixed resolution incremental encoder with 80000 pulses per mechanical revolution is installed on the extended shaft of the prototype IPM motor. The position measurement resolution is 0.0225° electrical degree. The encoder interface is internally implemented in the MicroAutoBox II I/O board for logging the speed and position information into the control system.

## 4.4 Conclusions

In this chapter, the novel nonlinear prototype IPM motor model relying on the current-flux linkage profiles are introduced. The original flux-current profiles were measured experimentally and were inverted to current-flux profiles by employing the proposed LUTs inversion method using nonlinear optimization. The new model with inverted LUTs avoids numerical differentiation of the flux linkage hence improves the dynamic performance, which is beneficial for the simulation validation of the proposed initial position estimation method. Additionally, the overview of experimental test bench has been introduced as well. The features of the key components of the prototype drive system have been explained in detail.

# Chapter 5

# Proposed Nonlinear Optimization Based Initial Position Estimation at Startup and Standstill

## 5.1 Introduction

This chapter proposes a nonlinear optimization based method for initial position estimation. In this method, a cost function is defined based on the voltage equations in $\alpha$-$\beta$ axes. Terminal quantities (voltage and current) are employed as inputs of the cost function and the knowledge of initial rotor position is extracted by minimizing the cost function. Three steps are needed for fast and accurate initial position estimation, as shown in Figure 5.1 and Figure 5.2. In Step I, a series short pulse voltage vectors are injected in $\alpha$-$\beta$ axes and the resulting current samples are recorded. The location of the $d$ axis can be identified by searching the minimum of the cost function. Since the machine performs two periods in one electrical cycle, there are two local

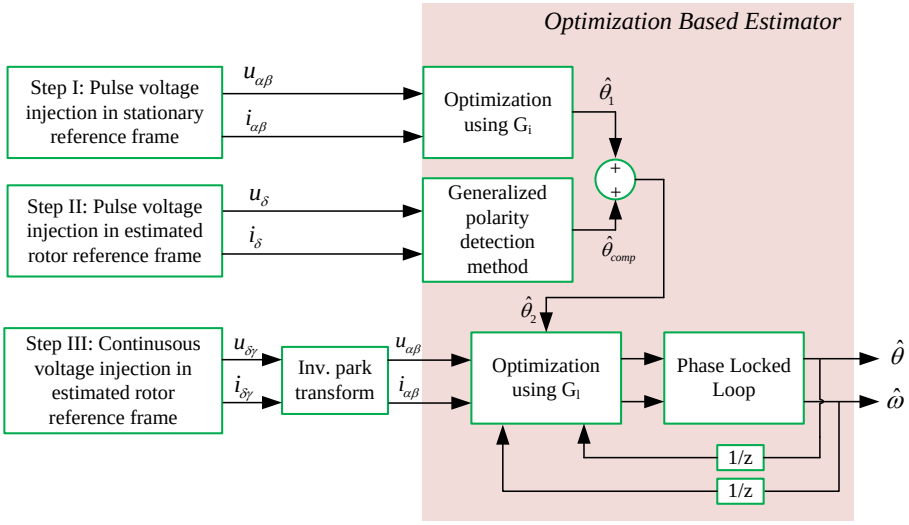


Figure 5.1: Block diagram of the proposed optimization based initial position estimator.

minimums in the cost function. In order to guarantee a robust position estimation, a generalized approach to polarity detection which exploits asymmetries in machine specific differential inductance profiles in $d$ axis is employed as Step II. This approach leads to a more robust estimation of the polarity that is less sensitive to measurement noise and can operate with lower resulting currents. After Step I and II, the expected initial position $\hat{\theta}_2$ is roughly estimated. In order to improve the estimation accuracy, continuous sinusoidal voltage is injected in estimated $d$ axis in Step III. A modified cost function is minimized based on the injected voltage and resulting current. Faster convergence is achieved compared with demodulation based method and Step III can be easily integrated with running state speed and position estimation.

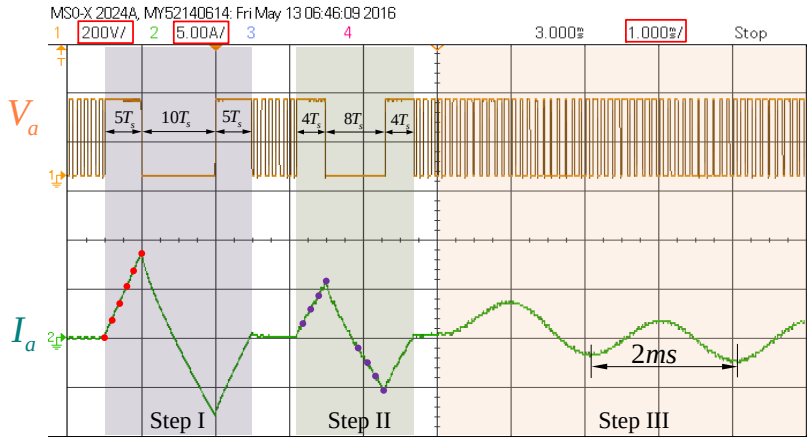


Figure 5.2: Screenshot of the scope, voltage injection procedures in initial position estimation.

## 5.2 Pulse Voltage Injection for Position Estimation

The discrete voltage equations of IPM motors in $d$-$q$ frame are

$$\begin{aligned}\begin{bmatrix}\bar{u}_d(k)\\ \bar{u}_q(k)\end{bmatrix} = \frac{1}{T_s}\begin{bmatrix}L_d & 0\\ 0 & L_q\end{bmatrix}\left(\begin{bmatrix}i_d(k+1)\\ i_q(k+1)\end{bmatrix} - \begin{bmatrix}i_d(k)\\ i_q(k)\end{bmatrix}\right)\\ - \omega_e(k)\left(\begin{bmatrix}0 & L_q\\ -L_d & 0\end{bmatrix}\begin{bmatrix}i_d(k)\\ i_q(k)\end{bmatrix} - \begin{bmatrix}0\\ \lambda_{pm}\end{bmatrix}\right),\end{aligned} \tag{5.1}$$

in which the compensated voltages that subtract the voltage drops on the phase resistance in $d$-$q$ frame are calculated by $\bar{u}_{dq} = u_{dq} - R_s i_{dq}$ (Sun *et al.*, 2015).

The machine shaft is not rotating in initial position estimation, i.e. $\omega_e = 0$. The

discrete voltage equations are simplified as

$$\begin{bmatrix} \bar{u}_d(k) \\ \bar{u}_q(k) \end{bmatrix} = \frac{1}{T_s} \begin{bmatrix} L_d & 0 \\ 0 & L_q \end{bmatrix} \left( \begin{bmatrix} i_d(k+1) \\ i_q(k+1) \end{bmatrix} - \begin{bmatrix} i_d(k) \\ i_q(k) \end{bmatrix} \right). \tag{5.2}$$

If (5.2) is transformed into $\alpha$-$\beta$ frame by actual position $\theta(k)$, then the equations are written as

$$\begin{bmatrix} \bar{u}_\alpha(k) \\ \bar{u}_\beta(k) \end{bmatrix} - \frac{L_a\big(\theta(k)\big)}{T_s} \left( \begin{bmatrix} i_\alpha(k+1) \\ i_\beta(k+1) \end{bmatrix} - \begin{bmatrix} i_\alpha(k) \\ i_\beta(k) \end{bmatrix} \right) = 0, \tag{5.3}$$

where $\bar{u}_{\alpha\beta}$ and $i_{\alpha\beta}$ represent the compensated voltages and the currents in $\alpha$-$\beta$ frame.

The inductance matrix $L_a\big(\theta(k)\big)$ in (5.3) is represented as

$$L_a\big(\theta(k)\big) = \begin{bmatrix} L_1 + L_2\cos 2\theta(k) & L_2 \sin 2\theta(k) \\ L_2 \sin 2\theta(k) & L_1 - L_2 \cos 2\theta(k) \end{bmatrix}, \tag{5.4}$$

where $L_1 = (L_d + L_q)/2$ and $L_2 = (L_d - L_q)/2$.

If the terminal quantities in $\alpha$-$\beta$ frame and the motor parameters are known, the initial rotor position can be estimated by solving the nonlinear equations in (5.3). However, the voltages and currents are both zero at standstill condition. In order to obtain the initial position, a series voltage pulses are injected in the stationary reference frame by directly applying gate signals to the voltage source inverter and the resulting current samples are recorded, as shown in Figure 5.3. The injection duration for each voltage vector can be customized for different machine drives ($5T_s$ for the prototype drive system). The equivalent injected voltages and resulting currents in $\alpha$-$\beta$ axes are illustrated in Figure 5.4. The current samples represented with red dots are utilized for initial position estimation. The voltage vector V(100) is applied for

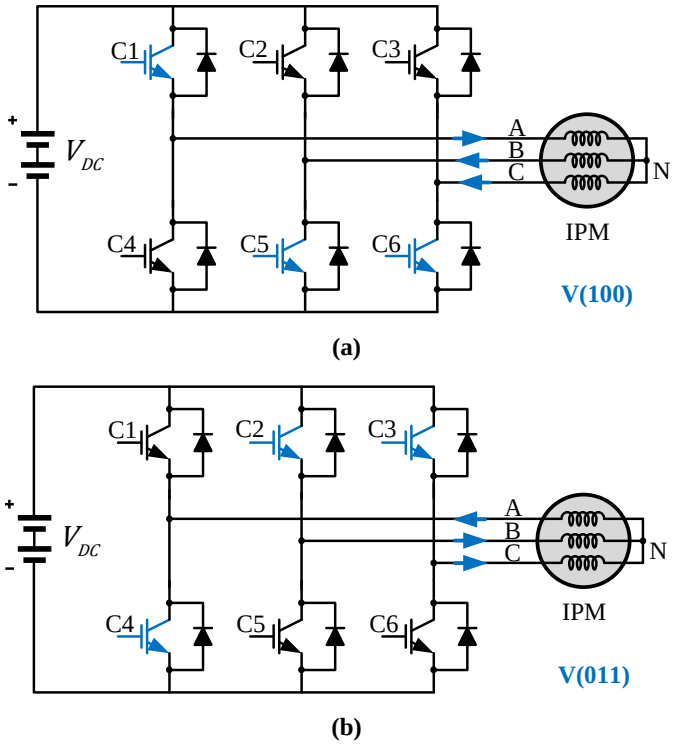


Figure 5.3: Voltage vectors applied for injection in Step I.

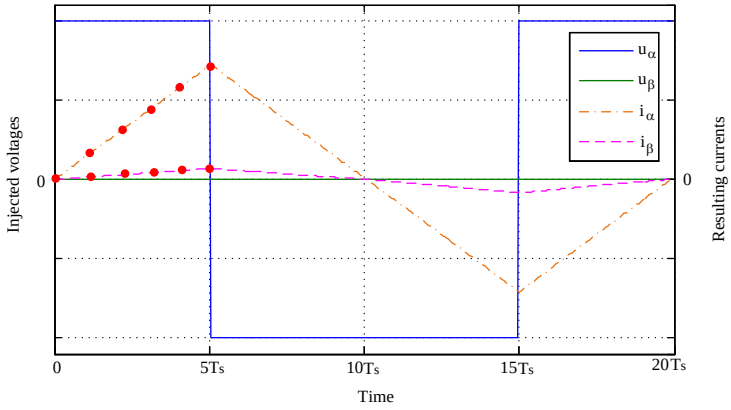


Figure 5.4: Injected voltages and resulting currents in $\alpha$-$\beta$ axes.

$5T_s$ and then the vector V(011) and V(100) are applied for $10T_s$ and $5T_s$ respectively to null the current response and balance the rotor movement (Sun *et al.*, 2015). Moreover, the proposed injection scheme is also shown in Figure 5.2 which is the screenshot of the scope in experiment. The yellow voltage $V_a$ is the voltage between phase A terminal and the negative bus bar of the inverter (voltage across the lower switch in phase A) and the green current $I_a$ is the measured phase A current. They are the direct measurements which can illustrate the injection scheme and resulting currents in $\alpha$-$\beta$ frame. The available DC link voltage $V_{DC}$ in the prototype drive system is 300 V. When the voltage vector V(100) is applied, the $V_a = 300V$ and the equivalent injected voltage in $\alpha$ axis is 200 V. The current samples used for position estimation are also marked with red dots in Figure 5.2. The current responses in the other two phases are also used for position estimation and the three phase current samples are transformed into $\alpha$-$\beta$ frame by Clark Transformation (Sun *et al.*, 2015).

If the cost function is defined in

$$\underset{\hat{\theta}}{\text{minimize}} \quad G_i(\hat{\theta}) = \sum_{k=1}^{m} \left\| \bar{u}_{\alpha\beta}(k) - \frac{L_a(\hat{\theta})}{T_s}\big(i_{\alpha\beta}(k+1) - i_{\alpha\beta}(k)\big) \right\|^2 \tag{5.5}$$

based on (5.3), then the cost is zero if the actual initial position is utilized. However, only estimated position exists in the sensorless control system. The cost will be zero if the estimated initial position is exactly the actual initial position, otherwise the cost will not be zero. The parameter $m$ indicates that the injection duration for each voltage vector lasts for $mT_s$. Since the rotor position is constant in initial position estimation, the $\hat{\theta}$ is used instead of $\hat{\theta}(k)$ for different current samples.

Figure 5.5 shows the plot of $G_i(\hat{\theta})$ versus position estimation errors at different initial positions using experimental data. Each data set refers to a certain initial

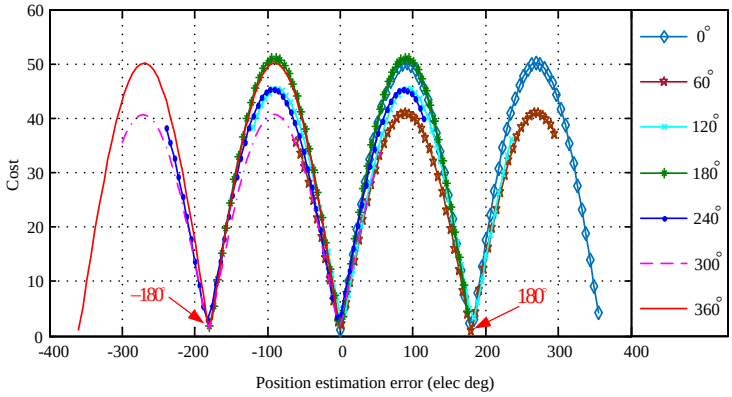


Figure 5.5: Plot of $G_i(\hat{\theta})$ versus position estimation errors at different initial positions for $m = 1$ based on experimental data.

position and is represented by a specific color and marker. From the figure, it is clear that $G_i(\hat{\theta})$ has two local minimums which locate around 0° error and 180° error in one electrical period at different initial positions. The cost function $G_i(\hat{\theta})$ decreases as the estimated position approaches to the two local minimums. The expected local minimum located at 0° position estimation error indicates that the positive direction of the estimated $d$ axis aligns with the north magnetic pole. The other local minimum located at 180° error implies that the positive direction of the estimated $d$ axis aligns with the south magnetic pole, which is unexpected. The initial position is estimated by searching the minimum of (5.5) and this nonlinear least-squares optimization can be easily solved by employing line search approaches (Luenberger and Ye, 2008).

However, the nonlinear optimization starts from an initial guess which can be closer to either the expected local minimum or the unexpected one. The failure of identifying the expected minimum will lead to the search algorithm converging to the unexpected local minimum. Hence, magnetic polarity detection is needed to guarantee the robustness of the initial position estimation.

## 5.3 Generalized Polarity Detection Method

As introduced in Section 3.5.2, existing magnetic polarity detection methods mostly rely on the magnetic saturation effect of the stator iron. The flux linkage in $d$ axis saturates under positive current, which can be observed from Figure 4.1 (b). The $d$ axis flux linkage profiles of the prototype machine were measured from experiments. In dual voltage pulses injection based method in 3.5.2, the current needed to detect reliable saturation can be close to or higher than the rated current and requires an inverter with high power rating in some machines. Moreover, checking two or three current peak values is not robust in detecting the polarity if the measurement noise and modeling inaccuracy are taken into consideration. In this thesis, in order to detect the magnetic polarity robustly, the $d$ axis flux linkage profile $\lambda_d(i_d, 0)$ was measured at different $i_d$ when $i_q = 0$ from experiment with typical motor drives components (Cintron-Rivera *et al.*, 2012). Then the $d$ axis differential inductance profile $\ell_{dd}(i_d, 0)$ is utilized, which is calculated as $\ell_{dd}(i_d, 0) = \partial\lambda_d(i_d, 0)/\partial i_d$. Figure 5.6 shows the experimental obtained $d$ axis differential inductance profile used in the generalized polarity detection method. The differential inductance profile is implemented as look-up tables in the real time experimental tests.

The calculated differential inductance $L_\delta^{diff}$ can be obtained from the injected voltages and induced currents at each sampling time in

$$L_\delta^{diff}(j) = \frac{\Delta\lambda_\delta(j)}{\Delta i_\delta(j)} = \frac{T_s\bar{u}_\delta(j-1)}{i_\delta(j) - i_\delta(j-1)} = \frac{T_s\bar{V}_{pol}}{i_\delta(j) - i_\delta(j-1)} \tag{5.6}$$

where $\bar{V}_{pol}$ denotes the magnitude of the compensated injection voltage subtracting the resistive voltage drop and $\Delta i_\delta$ represents the difference between two consecutive

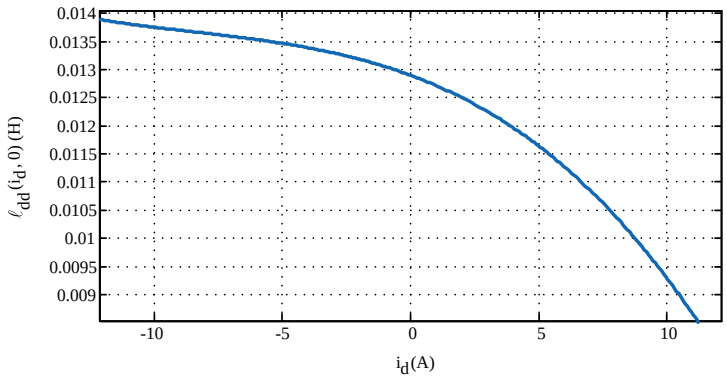


Figure 5.6: Experimental obtained $d$ axis differential inductance profile $\ell_{dd}(i_d, 0)$.

current samples. Since the voltage vectors are injected in $\delta$ axis, the current components in $\gamma$ axis are negligible. The current $i_\delta(j)$ is measured at each sample time and $L_\delta^{diff}(j)$ is calculated by (5.6) accordingly (Sun *et al.*, 2015).

The injection scheme for magnetic polarity detection is shown in Figure 5.7. Short voltage pulses are injected in $\delta$ axis with the same injection scheme in Step I. The injection magnitude is also 200 V and the injection duration is $4T_s$ for each voltage pulse. Since the voltage and current used for polarity detection are in the estimated $d$ axis, they can not be exactly reflected by the scope screenshot shown in Figure 5.2 with $V_a$ and $I_a$. But the injection scheme and the resulting current waveforms in $\delta$ axis can still be illustrated by Figure 5.2. The current samples in purple dots are used for polarity detection. In Figure 5.2, eight sets of data $(i_\delta(j), L_\delta^{diff}(j)), j = 1 \ldots 8$ are recorded. If the estimated $d$ axis aligns with the north pole, then $L_\delta^{diff}(j)$ matches with differential inductance profile $\ell_{dd}(i_\delta(j), 0)$ in Figure 5.6. If the estimated $d$ axis aligns with the south pole, $L_\delta^{diff}(j)$ matches with the profile $\ell_{dd}(-i_\delta(j), 0)$.

In general, if each voltage pulse lasts for $nT_s$, then the difference between $L_\delta^{diff}(j)$

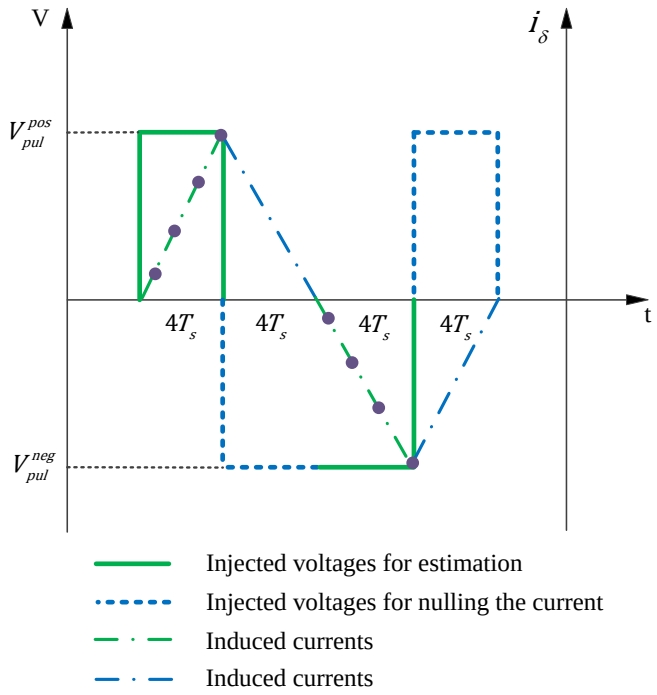


Figure 5.7: Injected voltages and resulting currents in $\delta$ axis for magnetic polarity detection.

and $\ell_{dd}(i_\delta(j), 0)$ is calculated in

$$\begin{aligned}
\Delta_1(j) &= L_\delta^{diff}(j) - \ell_{dd}(i_\delta(j), 0) \qquad j = 1 \ldots 2n \\
\Delta_2(j) &= L_\delta^{diff}(j) - \ell_{dd}(-i_\delta(j), 0) \qquad j = 1 \ldots 2n \\
c_1 &= \left\| \Delta_1(1)^2 + \Delta_1(2)^2 + \ldots + \Delta_1(2n)^2 \right\| \\
c_2 &= \left\| \Delta_2(1)^2 + \Delta_2(2)^2 + \ldots + \Delta_2(2n)^2 \right\| .
\end{aligned} \tag{5.7}$$

Figure 5.8 shows the framework of the proposed polarity detection algorithm. The costs $c_1$ and $c_2$ are calculated in (5.7) based on the injected voltages and resulting currents. If $c_1$ is smaller than $c_2$, the positive direction of $\delta$ axis aligns with the north

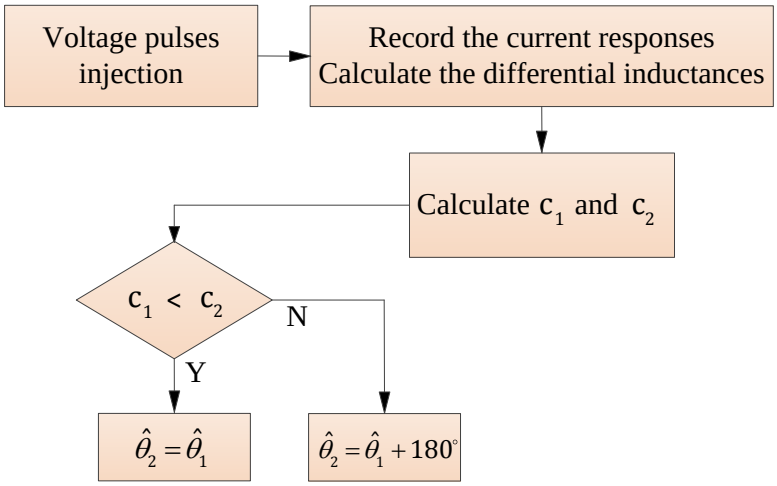


Figure 5.8: Framework of the proposed polarity detection method.

pole and the estimated position $\hat{\theta}_1$ from Step I is correct. While if $c_1$ is larger than $c_2$, the positive direction of $\delta$ axis aligns with the south pole and $\hat{\theta}_1$ has to be added by 180° (Sun *et al.*, 2015).

In Figure 5.2, the selected magnitude and duration of each injected voltage vector in Step I and II are customized for the prototype IPM motor drive system. Generally, the magnitude of the resulting current due to injected voltage is determined by the available DC link voltage, sampling time and motor parameters. In Step I, the resulting current peak changes with respect to the initial position because the equivalent inductances in $\alpha$-$\beta$ axes are position dependent. The maximum current peak in $\alpha$ axis happens when $\alpha$ axis aligns with $d$ axis. The current peak will be smaller at other initial positions, i.e. the current peak is smaller when $\alpha$ axis aligns with $q$ axis due to the larger $L_q$. Hence, the resulting current peak $I_{peak}$ in Step I and II can be

estimated by

$$I_{peak} \leq \frac{mT_s V_{eq}}{L_d}, \tag{5.8}$$

where $m$ and $V_{eq}$ denote the injection duration of each voltage vector and the equivalent injected voltage in $\alpha$ axis or $\delta$ axis. The $L_d$ value used in (5.8) comes from the experimental obtained $d$ axis differential inductance profile mentioned above. Theoretically, the estimation method in Step I should work when $m \geq 1$. In practice, the injection duration needs to be increased to achieve robust initial position estimation. A reasonable first estimate of $I_{peak}$ can be 50% of the rated current and the calculated $m$ can be adjusted in simulation and experimental tests based on this initial estimate. The injection duration $m \in [3\ 6]$ in Step I for the prototype drive system. If $m < 3$, robust estimation can not be guaranteed. If $m \geq 6$, the $I_{peak}$ is close to and larger than the rated current. The $5T_s$ injection duration is selected by considering both the estimation accuracy and the $I_{peak}$ value. In Step II, the robust detection of polarity can be achieved when $m \geq 4$. Since the polarity detection is to make a decision whether compensating 180° or not, no further accuracy issue needs to be considered. Therefore, the injection duration for polarity detection is chosen as $4T_s$. Hence, the proposed methods in Step I and II are generalized for different IPMSM drives but the optimal injection scheme needs to be determined distinctly for a specific drive system based on the strategy mentioned above.

## 5.4 Continuous Sinusoidal Voltage Injection for Position Estimation

After Step I and II, the initial position with polarity correction has already been obtained, which is $\hat{\theta}_2$ in Figure 5.1. The benefits of the pulse injection based method is its fast estimation capability. However, the assumption that the injected voltage magnitudes are kept constant regardless of the injection direction can't be guaranteed due to the inverter nonlinearities. Using calculated voltages instead of directly measured ones will affect the estimation accuracy (Antonello *et al.*, 2015). Moreover, the position needs to be continuously estimated at standstill condition besides machine startup, i.e. rotor is locked mechanically. Hence, a continuous voltage injection based method using nonlinear optimization is proposed for position estimation at standstill condition and for easier integration with the speed and position estimation at running state.

Based on (5.1), a modified cost function

$$\begin{aligned}\underset{\hat{\theta}(k),\hat{\omega}(k)}{\text{minimize}} \qquad & G_l\left(\hat{\theta}(k),\hat{\omega}_e(k)\right) = \left\| \bar{u}_{\alpha\beta}(k) - \frac{L_a\big(\hat{\theta}(k)\big)}{T_s}\Big(T\big(\Delta\hat{\theta}(k)\big)i_{\alpha\beta}(k+1) - i_{\alpha\beta}(k)\Big) \right. \\ & \left. + \hat{\omega}_e(k)\left(L_b\big(\hat{\theta}(k)\big)i_{\alpha\beta}(k) + \lambda_{pm}\begin{bmatrix}\sin\hat{\theta}(k)\\ -\cos\hat{\theta}(k)\end{bmatrix}\right)\right\|^2 + K_1\left(\hat{\theta}(k) - \hat{\theta}(k-1)\right)^2 \\ & + K_2\Big(\hat{\omega}_e(k) - \hat{\omega}_e(k-1)\Big)^2\end{aligned} \tag{5.9}$$

is derived by utilizing the similar idea in deducing the cost function (5.5). The position difference between two consecutive sample times is calculated as $\Delta\hat{\theta}(k) = T_s\hat{\omega}_e(k)$. In initial position estimation, $\hat{\omega}_e(k)$ equals to zero. The transformation $T(\Delta\hat{\theta}(k))$ is

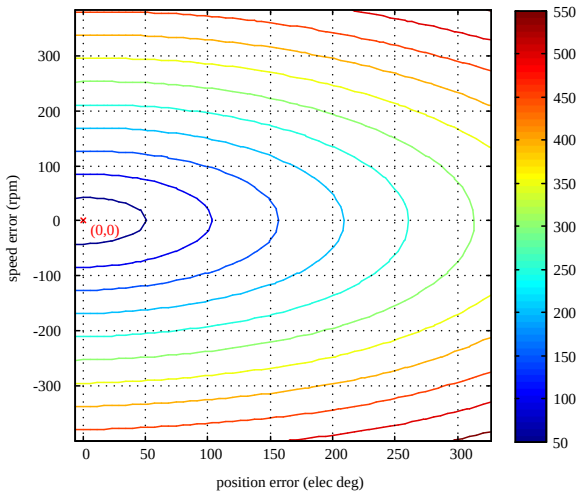


Figure 5.9: Contour plot of the cost function (5.9) at standstill condition.

represented in

$$T\left(\Delta\hat{\theta}(k)\right) = \begin{bmatrix} \cos\left(\Delta\hat{\theta}(k)\right) & \sin\left(\Delta\hat{\theta}(k)\right) \\ -\sin\left(\Delta\hat{\theta}(k)\right) & \cos\left(\Delta\hat{\theta}(k)\right) \end{bmatrix}. \tag{5.10}$$

At standstill condition, continuous sinusoidal voltages are injected in estimated $d$ axis, which is shown as Step III in Figure 5.2. The voltage and current information are used for estimation in each sample time. The previous estimated speed and position are used as starting points for the next optimization. The contour plot of (5.9) is depicted in Figure 5.9.

In Figure 5.9, only one minimum in the origin is obtained in one electrical period, which indicates the correct speed and position estimation. Therefore, the speed and position estimation becomes an online nonlinear optimization problem with two decision variables and the estimation can be achieved by minimizing the cost function (5.9). If the previous estimation is known in (5.9), the optimization will finally reach to the expected minimum with finite iterations. In this way, the speed and position

are continuously estimated in Step III. A PLL is implemented in series with the optimization based position estimator in Step III as a filter. More analysis of the cost function (5.9), and the nonlinear optimization based speed and position estimation at running state will be illustrated in Chapter 6.

## 5.5 Simulation Verifications

The proposed initial position estimation algorithms were modeled and simulated in MATLAB/SIMULINK before experimental verification. The novel nonlinear machine model introduced in Chapter 4 is employed for accurately simulating the initial position estimation performance. The switching frequency and sampling frequency were both set to 10 kHz and the DC link voltage was 300 V. The injection scheme used in Step I and II is identical with Figure 5.2. For the continuous injection in Step III, the magnitude of the sinusoidal voltage was 70 V and the injection frequency was 500 Hz.

Figure 5.10 illustrates the simulation results of the initial position estimation when the actual position was 41.5° electrical degree. The green shade represents Step I and Step II which last for 4.1 ms in total. After position estimation and polarity detection, the estimation error is 10°. This error comes from the mismatch between the constant parameter estimation model and real nonlinear machine model. Then the continuous sinusoidal voltage is injected in Step III and the final position estimation error is $-0.5°$ electrical degree, as shown in Figure 5.10 (b). In this test, the compensation of the polarity detection is 0° because $c_1$ is smaller than $c_2$, which is illustrated in Figure 5.10 (c).

Figure 5.11 shows the position estimation results when the actual position was

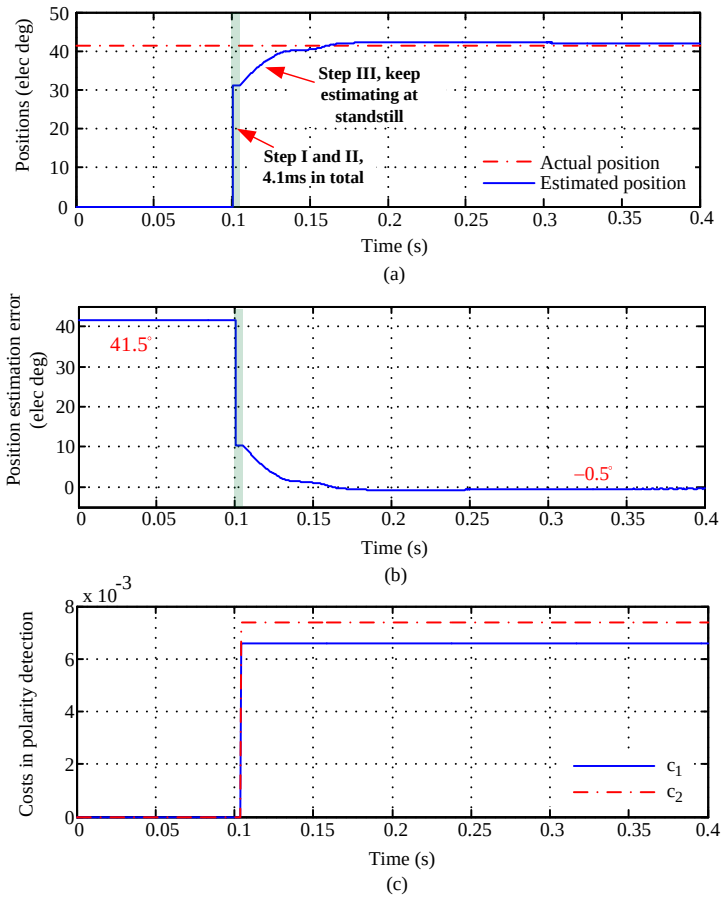


Figure 5.10: Simulation results on initial position estimation at 41.5°: (a) actual and estimated positions; (b) position estimation error; (c) $c_1$ and $c_2$ in polarity detection.

250°. After position estimation there exists 180° error in the estimation results, which can be reflected by the fact that $c_1$ is larger than $c_2$. This error is compensated by the proposed polarity detection algorithm and Figure 5.11 (a) illustrates the position estimation results. The position estimation error in this case is 0.8° electrical degree after Step III.

In Step III, the continuous voltage injection is used and the modified cost function (5.9) is employed in position estimation. Since both speed and position are decision variables in the optimization, the same idea can be extended to speed and position

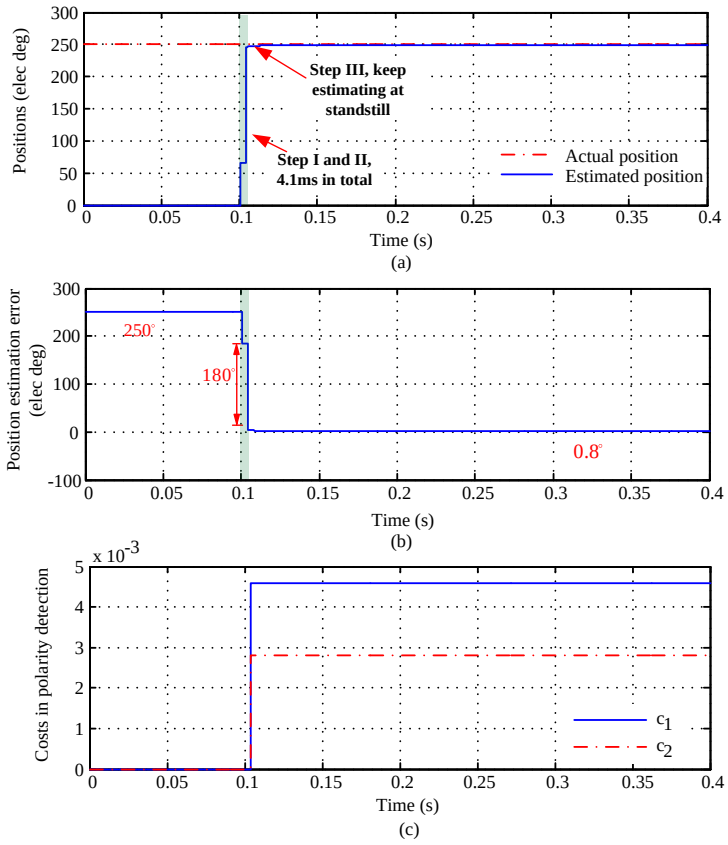


Figure 5.11: Simulation results on initial position estimation at 250°: (a) actual and estimated positions; (b) position estimation error; (c) $c_1$ and $c_2$ in polarity detection.

estimation at low speed conditions. Figure 5.12 illustrates the speed and position estimation from standstill condition to low speed operations. The speed and position estimation both works well at standstill condition and low speed.

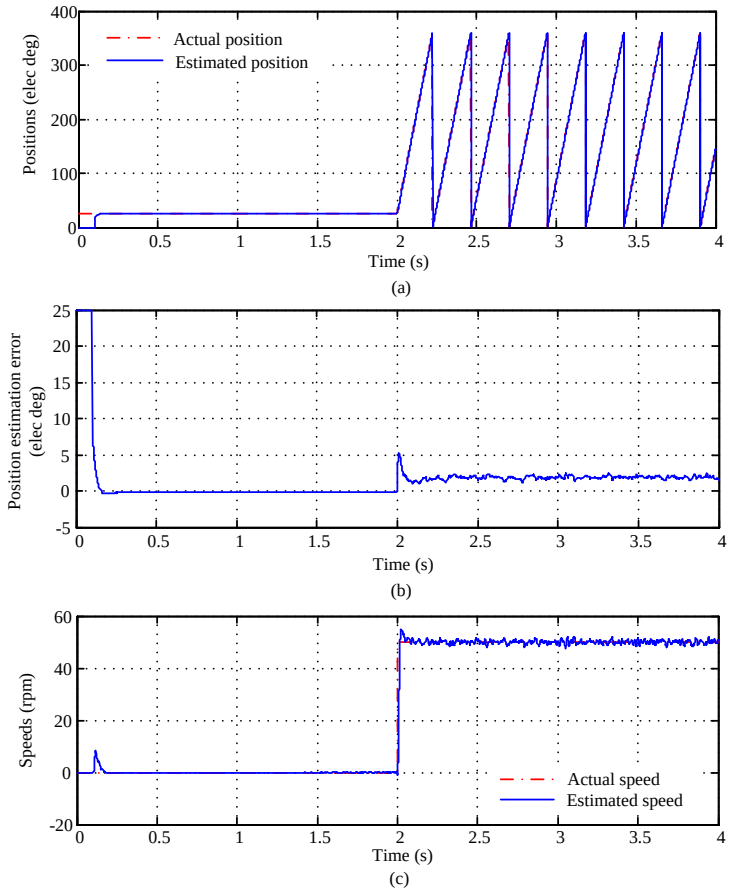


Figure 5.12: Simulation results on integration of speed and position estimation at standstill and low speed: (a) actual and estimated positions; (b) position estimation error; (c) actual and estimated speeds.

## 5.6 Experimental Verifications

### 5.6.1 Experimental Results on Initial Position Estimation

The proposed initial position estimation approach was tested with the experimental test bench shown in Figure 4.6. The IPMSM drives parameters and injection scheme are identical with simulation test conditions shown in Section 5.5.

Figure 5.13 illustrates the estimation results when the real measured position was

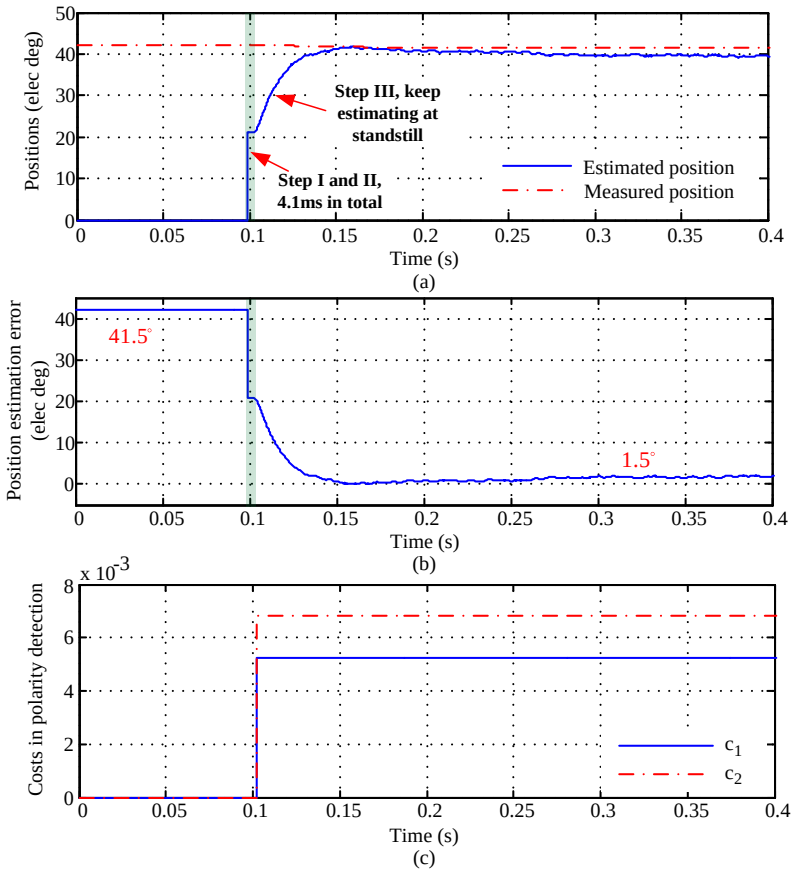


Figure 5.13: Experimental results on initial position estimation at 41.5°: (a) measured and estimated positions; (b) position estimation error; (c) $c_1$ and $c_2$ in polarity detection.

41.5° electrical degree. The green shade represents Step I and Step II which last for 4.1 ms in total. After position estimation and polarity detection, the estimation error is 20°. This error is larger compared with simulation. This is due to the involvement of measurement noise and inverter nonlinearities. Then the continuous sinusoidal voltage is injected and the final position estimation error is 1.5° electrical degree, as shown in Figure 5.13 (b). In this test, the compensation of the polarity detection is 0° because $c_1$ is smaller than $c_2$, which is illustrated in Figure 5.13 (c). The experimental

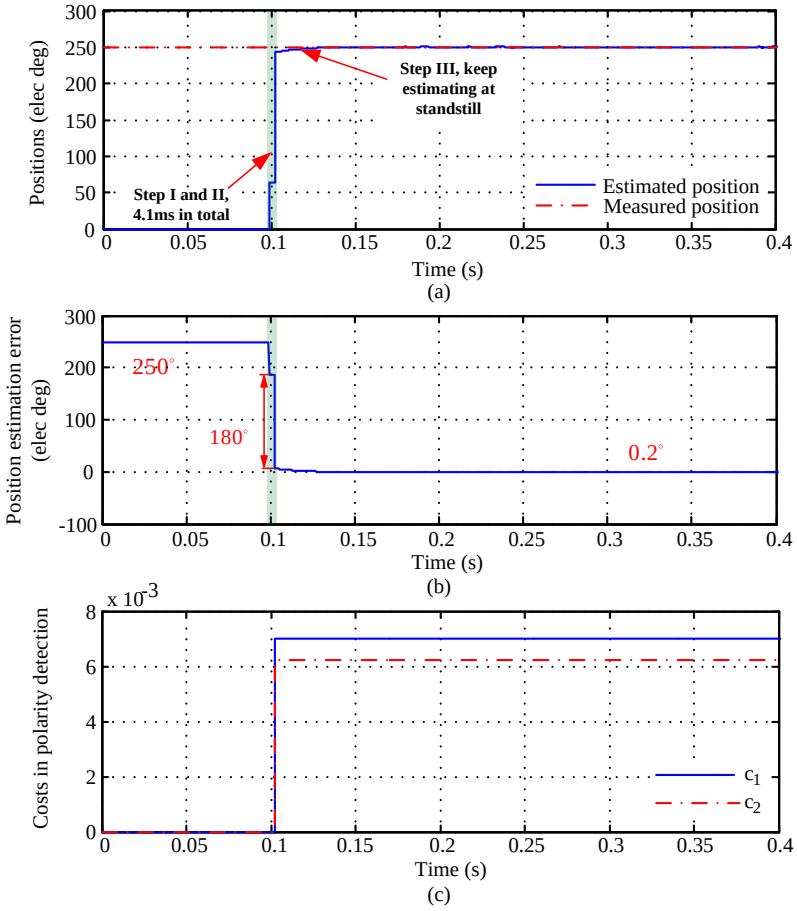


Figure 5.14: Experimental results on initial position estimation at 250°: (a) measured and estimated positions; (b) position estimation error; (c) $c_1$ and $c_2$ in polarity detection.

results match with the simulation very well.

Figure 5.14 shows the position estimation results when the real position was 250°. After Step I there exists 180° error in the estimation results, which can be reflected by the fact that $c_1$ is larger than $c_2$. This error is compensated by the proposed polarity detection algorithm and Figure 5.14 (a) illustrates the position estimation results. The position estimation error in this case is 0.2° electrical degree after Step III, which is observed similarly in the simulation results.

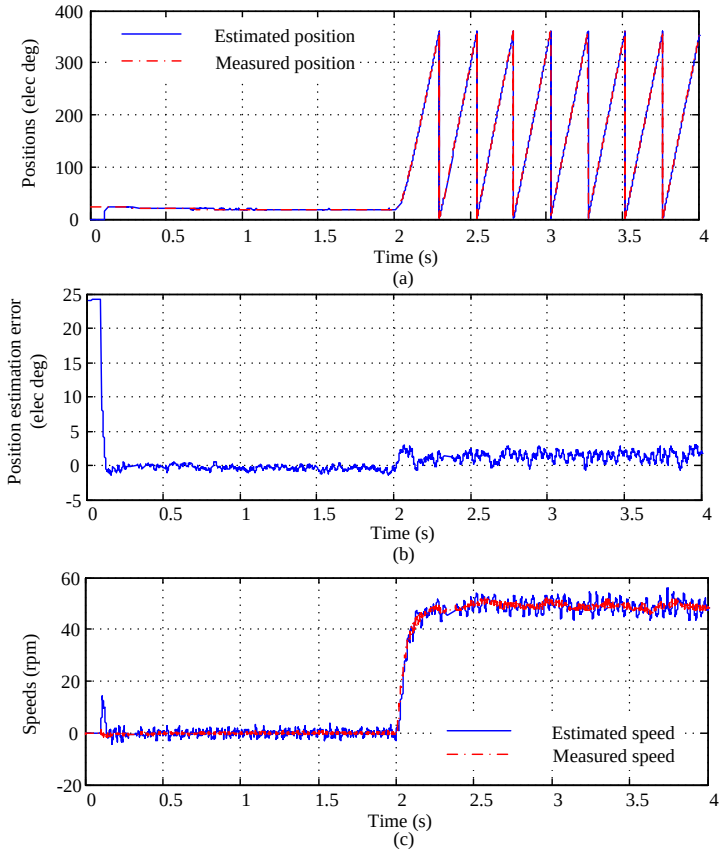


Figure 5.15: Experimental results on integration of speed and position estimation at standstill and running state: (a) measured and estimated positions; (b) position estimation error; (c) measured and estimated speeds.

Similarly in Figure 5.12, the integration of standstill estimation and low speed estimation was tested in experiments. The experimental results are shown in Figure 5.15. It is concluded that the optimization based method is unified at standstill condition as well as low speed operations. More details about running state estimation will be shown in Chapter 6.

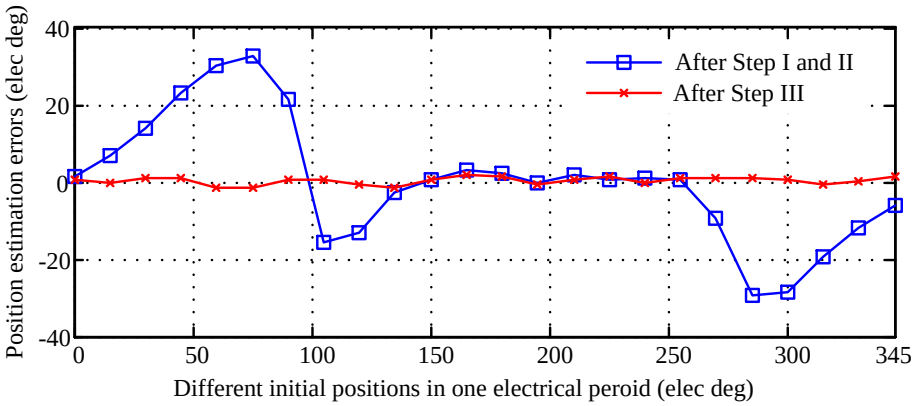


Figure 5.16: Experimental results, position estimation errors of pulse voltage injection and continuous sinusoidal voltage injection.

### 5.6.2 Accuracy Comparison Between Pulse Voltage Injection and Continuous Sinusoidal Injection

The benefit of the pulse voltage injection based initial position estimation is its fast response. In the experimental tests illustrated above, the initial position was roughly achieved with only 4.1 ms. However, the estimation accuracy can't be guaranteed due to the machine and inverter nonlinearities, as mentioned in Section 5.4. Figure 5.16 shows the comparison of the estimation accuracies between pulse injection and continuous injection. The average estimation error of the pulse injection is 11.52° while the final average estimation error decreases to 0.91° electrical degree after the sinusoidal injection and the PLL are involved in Step III.

## 5.7 Conclusions

In this chapter, an optimization based initial position estimation algorithm is proposed. A cost function is defined and the position can be estimated by searching

the minimum of the cost function. Three steps which employ different voltage injections are utilized in the fast and accurate estimation of initial position. The pulse voltage injection for position estimation benefits from its fast response, but polarity detection and accuracy improvements are needed. The proposed polarity detection method generalizes the polarity detection techniques for different IPM motor drives. The polarity can be detected once the differential inductance profile is known. Compared with methods relying solely on saturation, the proposed method requires lower currents to reliably determine the polarity. The continuous voltage injection is used for position estimation at standstill condition after the initial position is roughly obtained. The involvement of continuous injection in Step III improves the estimation accuracy and proposes a unified solution for integrating the speed and position estimation at standstill condition and running state.

The feasibility of the proposed initial position estimation method has been investigated and validated with both simulation and experimental tests. The initial position can be identified within 50 milliseconds and the position estimation accuracy is less than 1° electrical degree.

# Chapter 6

# Proposed Nonlinear Optimization Based Speed and Position Estimation at Running State

## 6.1 Introduction

This chapter proposes a nonlinear optimization based position and speed estimation algorithm for wide speed range operations. A cost function based on voltage equations in the stationary reference frame is employed for speed and position estimation. The speed and position are both involved in the cost function and they are decision variables for this nonlinear optimization problem. The speed and position can be estimated by minimizing the proposed cost function based on measurements of stator voltages and currents. Since the voltage information is less significant at low speed and unable to be observed at standstill condition, extra high frequency sinusoidal voltages are injected in estimated magnetic axis. Extra regularization terms

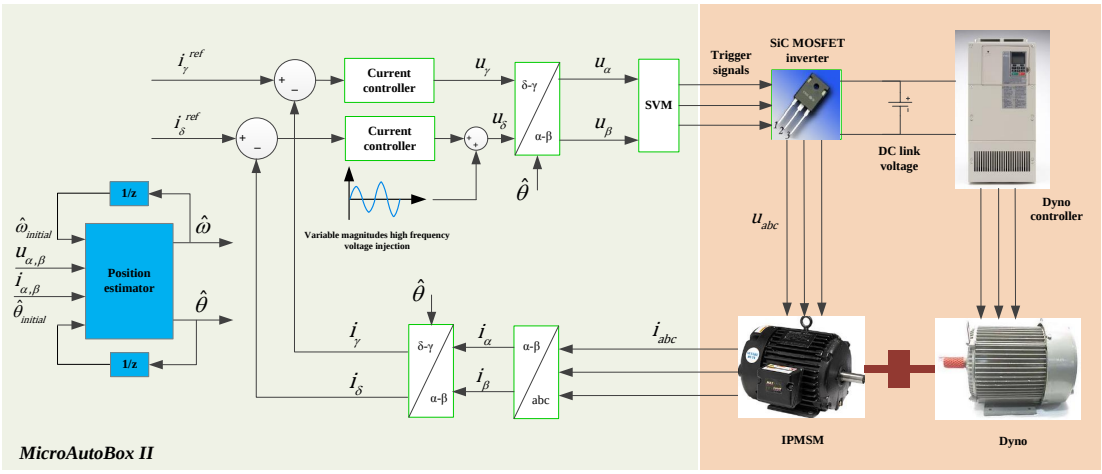


Figure 6.1: Block diagram of the proposed nonlinear optimization based sensorless control system.

are added in the cost function at low speed to improve speed and position estimation quality. A PLL is involved at the output of the position estimator serving as a filter. In this way, a unified position and speed estimation method is proposed for wide speed range operation without switching between different position estimation algorithms at wide speed range. The system block diagram is shown in Figure 6.1. Analysis on the cost function and convexity under different speeds and positions are also shown in this chapter. The feasibility of the proposed estimation algorithm is validated with the prototype IPM motor drive system. Additionally, the parameter sensitivity analysis of the proposed method is also illustrated both with theoretical analysis and experimental tests.

## 6.2 Optimization Based Sensorless Algorithm for Medium and High Speed Operation

In IPMSM drives, if the discrete voltage equation (5.1) in $d$-$q$ frame is transformed into $\alpha$-$\beta$ frame by actual position $\theta(k)$, then the equations are written as

$$\begin{bmatrix} \bar{u}_\alpha(k) \\ \bar{u}_\beta(k) \end{bmatrix} - \frac{L_a\big(\theta(k)\big)}{T_s}\left(T\big(\Delta\theta(k)\big)\begin{bmatrix} i_\alpha(k+1) \\ i_\beta(k+1) \end{bmatrix} - \begin{bmatrix} i_\alpha(k) \\ i_\beta(k) \end{bmatrix}\right) \tag{6.1}$$
$$+\,\omega_e(k)\left(L_b\big(\theta(k)\big)\begin{bmatrix} i_\alpha(k) \\ i_\beta(k) \end{bmatrix} + \lambda_{pm}\begin{bmatrix} \sin\theta(k) \\ -\cos\theta(k) \end{bmatrix}\right) = 0.$$

The position dependent matrices $L_{ab}\big(\theta(k)\big)$ are calculated as

$$L_a\big(\theta(k)\big) = \begin{bmatrix} L_1 + L_2\cos 2\theta(k) & L_2\sin 2\theta(k) \\ L_2\sin 2\theta(k) & L_1 - L_2\cos 2\theta(k) \end{bmatrix} \tag{6.2}$$

$$L_b\big(\theta(k)\big) = \begin{bmatrix} L_2\sin 2\theta(k) & L_1 - L_2\cos 2\theta(k) \\ -L_1 - L_2\cos 2\theta(k) & -L_2\sin 2\theta(k) \end{bmatrix} \tag{6.3}$$

If the terminal quantities in $\alpha$-$\beta$ frame and the motor parameters are known, the speed and position can be extracted by solving the nonlinear equations in (6.1). If a cost function is defined in (6.4) based on (6.1), then the cost is zero if actual position and speed are used. Since only estimated position and speed exist in the sensorless control system, the cost will be zero if the estimated speed and position are exactly

the actual ones (Sun *et al.*, 2016).

$$\underset{\hat{\theta}(k),\hat{\omega}(k)}{\text{minimize}} \qquad G_r\left(\hat{\theta}(k),\hat{\omega}_e(k)\right) = \left\| \bar{u}_{\alpha\beta}(k) - \frac{L_a\big(\hat{\theta}(k)\big)}{T_s}\Big(T\big(\Delta\hat{\theta}(k)\big)i_{\alpha\beta}(k+1) - i_{\alpha\beta}(k)\Big) \right. \tag{6.4}$$
$$\left. + \hat{\omega}_e(k)\left(L_b\big(\hat{\theta}(k)\big)i_{\alpha\beta}(k) + \lambda_{pm}\begin{bmatrix}\sin\hat{\theta}(k)\\ -\cos\hat{\theta}(k)\end{bmatrix}\right)\right\|^2$$

Figure 6.2 shows the contour plots of the cost function at different speed and position conditions. The horizontal axis is position estimation error and the vertical axis is speed estimation error. From the contour plots, it is clear that the cost decreases as the estimated speed and position approach to the actual speed and position. The cost function has two local minimums in one electrical period. If the machine is running at $N$ rpm, the first local minimum locates at the origin. The speed and position errors are both zero, which indicates the correct estimation. The second local minimum's coordinate is (180°, -2$N$ rpm) which corresponds to the negative direction of the magnetic axis. Therefore, the speed and position estimation at running state becomes an online nonlinear optimization problem with two decision variables and the estimation can be achieved by minimizing the cost function (6.4).

If the cost function is locally convex and if the initial value of each estimation is around the expected local minimum, the optimization is able to reach to the expected local minimum with finite iterations. A cost function is said to be convex if the second derivative (Hessian) is positive semi-definite in a convex region (Boyd and Vandenberghe, 2004). However, the analytical demonstration is challenging due to the complexity of the Hessian of the proposed cost function. A real symmetric matrix is said to be positive semi-definite if all its eigenvalues are non-negative. In the

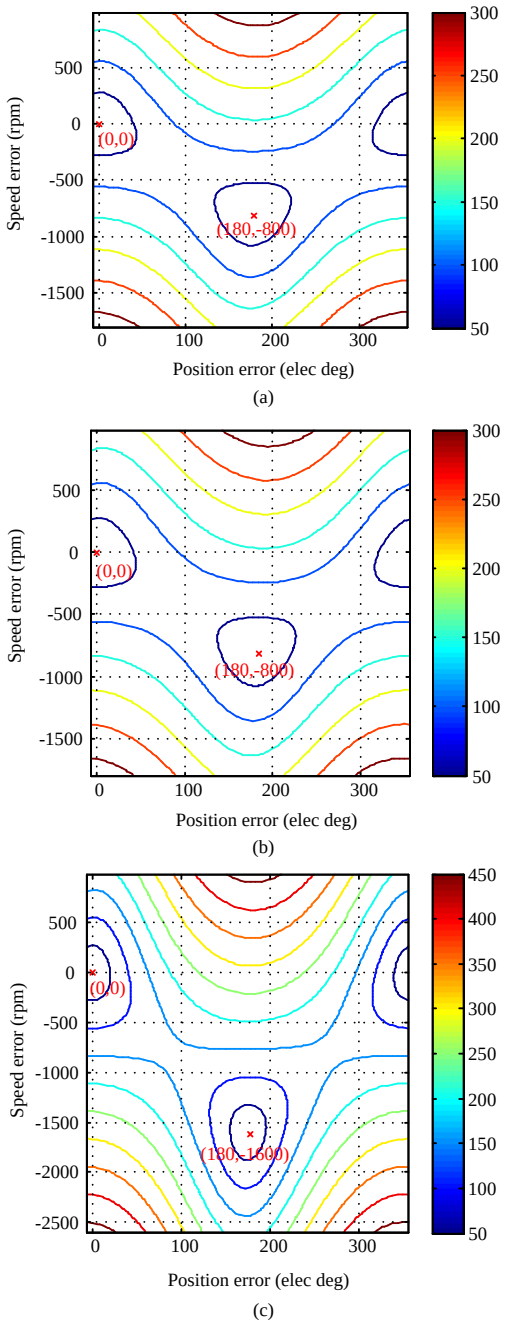


Figure 6.2: Contour plots of the cost function (6.4): (a) 400 rpm and $i_{phase}^{peak} = 0$; (b) 400 rpm and $i_{phase}^{peak} = 4$; (c) 800 rpm and $i_{phase}^{peak} = 0$.

proposed cost function, the Hessian is a $2 \times 2$ real symmetric matrix and has two eigenvalues. The local convexity of the cost function around the two local minimums is illustrated by plotting the region in which all the eigenvalues of the Hessian are non-negative. The procedures are: (a) The eigenvalues of the Hessian are calculated at different speeds and positions with $0.4^\circ$ degree and 10 rpm intervals; (b) If the two eigenvalues are both non-negative, the point is recorded and plotted on top of the contour plot of the cost function; (3) The convex regions then are depicted in Figure 6.3 and Figure 6.4. The plots were also depicted with the position and speed intervals as small as $0.1^\circ$ degree and 1 rpm and the convex regions have the same envelops with Figure 6.3 and Figure 6.4 but with more points included. The idea of illustrating the observer convergence with plots or system trajectories has already been used in literature (Nahid-Mobarakeh *et al.*, 2004, 2007). In Figure 6.3 (b) and Figure 6.4 (b), the zoomed in convex regions around the expected local minimum are shown. The convergence of the proposed position estimator is guaranteed if the speed and position errors are within those regions. Outside these regions, no convergence guarantees can be issued (Sun *et al.*, 2016).

## 6.3 Modification of the Cost Function at Low Speed Operation

Since the back-emf is proportional to the machine speed, the voltage magnitudes in (6.4) is more significant at higher speed. The size of the local convex region increases at higher speed due to the increase of the voltages, as illustrated in Figure 6.3 and Figure 6.4. At very low speed including standstill condition, the cost function $G_r$ in

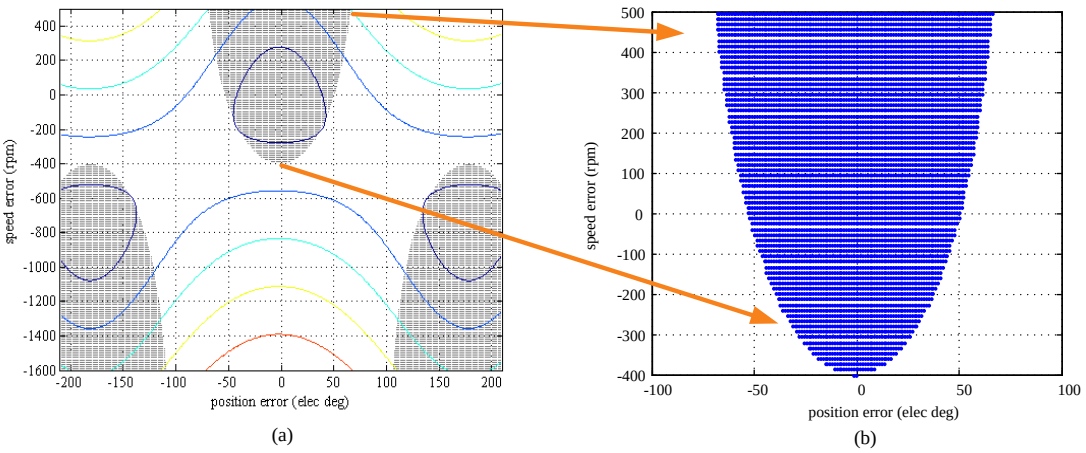


Figure 6.3: Convex region of the cost function at 400 rpm: (a) convex regions on the contour plot; (b) zoomed in convex region around the expected local minimum.

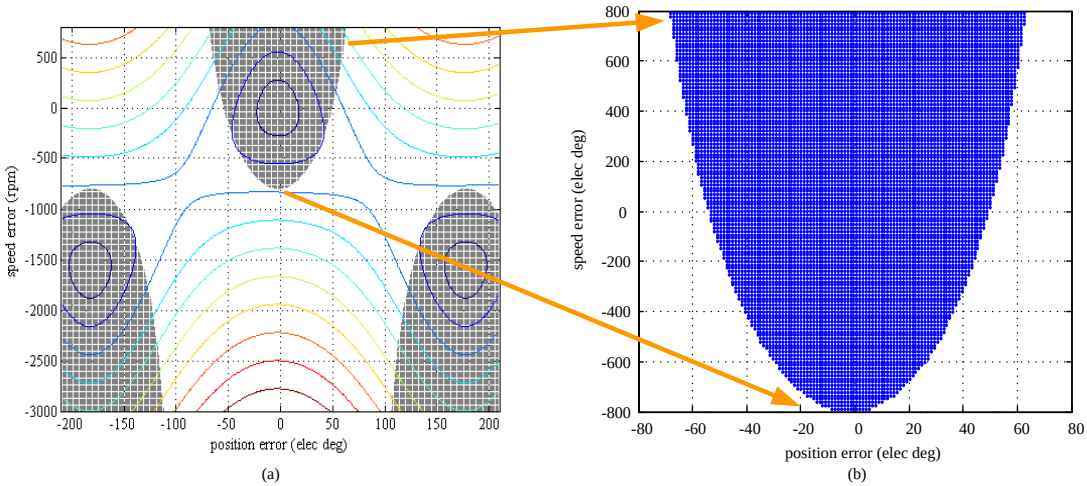


Figure 6.4: Convex region of the cost function at 800 rpm: (a) convex regions on the contour plot; (b) zoomed in convex region around the expected local minimum.

(6.4) is not convex as shown in Figure 6.5 (a) and Figure 6.6 (a). In order to estimate the speed and position at low speed, high frequency sinusoidal voltages are injected in $\delta$ axis and $G_r$ is modified in

$$\underset{\hat{\theta}(k),\hat{\omega}(k)}{\text{minimize}} \quad G_l(\hat{\theta}(k),\hat{\omega}_e(k)) = G_r\left(\hat{\theta}(k),\hat{\omega}_e(k)\right) + K_1\left(\hat{\theta}(k)-\hat{\theta}(k-1)\right)^2 + K_2\left(\hat{\omega}_e(k)-\hat{\omega}_e(k-1)\right)^2. \tag{6.5}$$

Equation (6.5) is the same with the cost function introduced in (5.9) in Chapter 5. The extra regularization terms $K_1\left(\hat{\theta}(k)-\hat{\theta}(k-1)\right)^2$ and $K_2\left(\hat{\omega}_e(k)-\hat{\omega}_e(k-1)\right)^2$ are added in the cost function as a filter. Improvements of the cost function can be found in the comparison between Figure 6.5 (a), (b) and Figure 6.6 (a), (b). The $\hat{\omega}_e(k-1)$ and $\hat{\theta}(k-1)$ are assumed to be actual speed and position in plotting Figure 6.5 (b) and Figure 6.6 (b). With modification of the cost function and involvement of the voltage injection, the plot of the cost function (6.5) become convex and has only one minimum at origin in one electrical period. The convex regions of the modified cost function at 0 rpm and 50 rpm are shown in Figure 6.7. The $K_1$ and $K_2$ are both set to zero at high speed conditions (Sun *et al.*, 2016).

## 6.4 Variable Magnitudes Sinusoidal Voltage Injection

In the unified sensorless control algorithm, a variable magnitudes high frequency voltage injection method is employed at low speed. The high frequency sinusoidal voltage is injected in $\delta$ axis and superimposed on the fundamental frequency voltages.

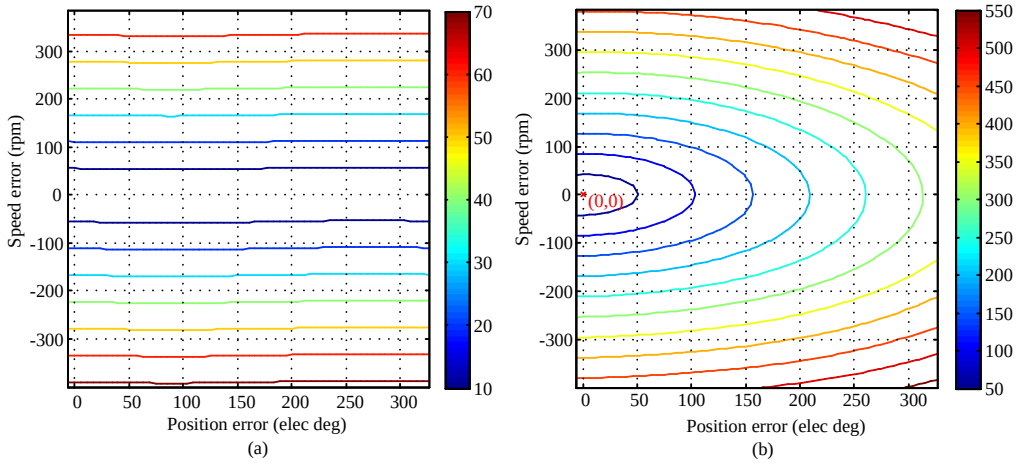


Figure 6.5: Contour plots of the cost function: (a) cost function $G_r$ at 0 rpm without injection; (b) cost function $G_l$ at 0 rpm with injection.

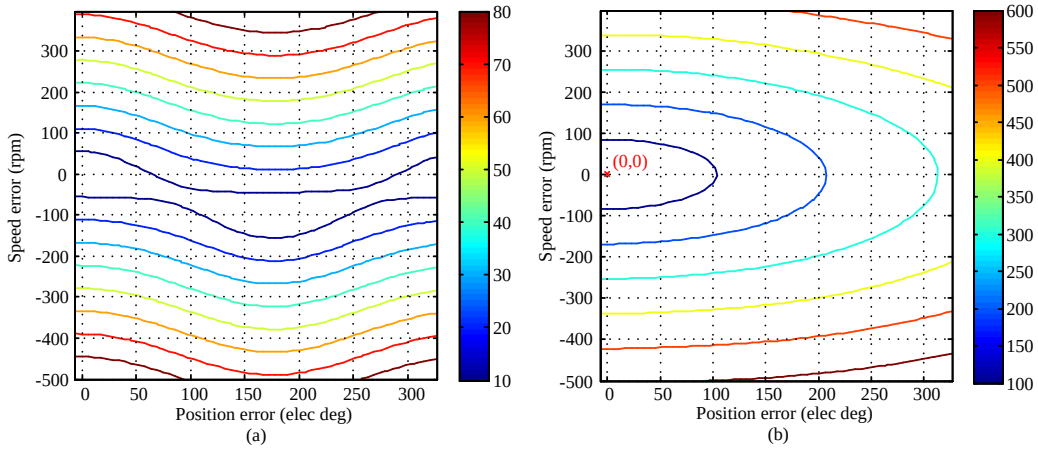


Figure 6.6: Contour plots of the cost function: (a) cost function $G_r$ at 50 rpm without injection; (b) cost function $G_l$ at 50 rpm with injection.

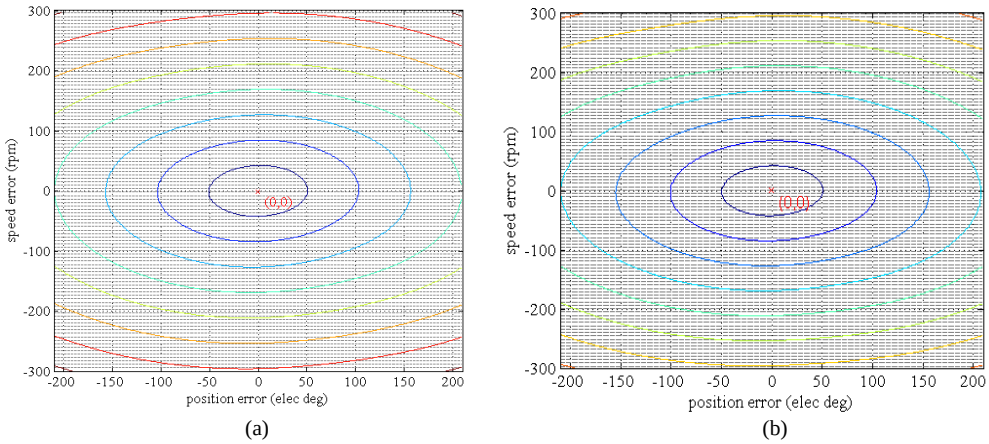


Figure 6.7: Convex regions of the modified cost function $G_l$: (a) convex region at 0 rpm; (b) convex region at 50 rpm.

The injection scheme is shown in

$$V_{inj} = \begin{cases} \frac{N_1 - \left|\hat{N}\right|}{N_1} V_1 & \left|\hat{N}\right| \leq N_1 \\ 0 & \left|\hat{N}\right| > N_1 \end{cases} \tag{6.6}$$

as well as Figure 6.8. In this way, the injected voltage is adjusted according to the estimated speed and extra loss is reduced. In summary, the original cost function (6.4) is utilized for estimation without injection when the motor speed is higher than $N_1$. The variable magnitudes high frequency voltage injection and the modified cost function (6.5) are employed when the motor speed is lower than $N_1$. The values of $K_1$ and $K_2$ were tuned heuristically in simulation and experimental tests. The switch from (6.5) to (6.4) is achieved by setting $K_1$ and $K_2$ to zero. Hence, the algorithm for speed and position estimation at low speed and high speed is unified instead of combining different estimation methods in (Silva *et al.*, 2006; Bisheimer *et al.*, 2010; Andreescu *et al.*, 2008; Wang *et al.*, 2013a; Ma *et al.*, 2013; Bolognani *et al.*, 2012).

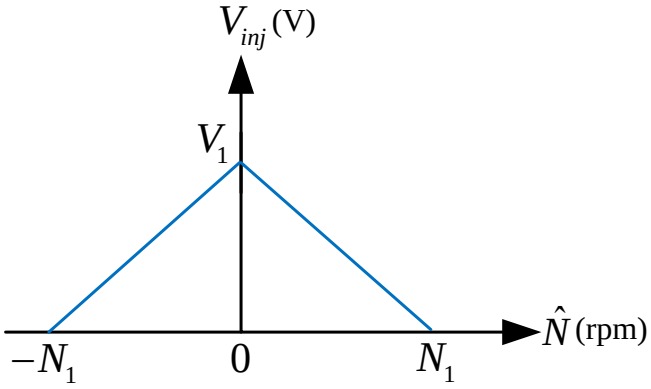


Figure 6.8: Variable magnitudes voltage injection scheme.

## 6.5 Observer Implementation

In the real time implementation, the modified Newton's method is employed for minimizing the cost function shown in (6.4) and (6.5) numerically. The compensated voltages $\bar{u}_{\alpha\beta}$ and the measured currents $i_{\alpha\beta}$ are employed for estimation at the sampling frequency. First of all, estimated speed and position in the previous sample time are set as the initial values for the optimization. Then the search direction is computed by calculating the partial derivatives $J$ ($2 \times 1$ matrix) and Hessian matrix $H$ of the cost function. The step size $\xi$ is searched for minimizing the cost by using the line search method. At the end of each estimation, the new decision variables $\hat{\theta}(k+1)$ and $\hat{\omega}(k+1)$ are updated with

$$\begin{bmatrix} \hat{\theta}(k+1) \\ \hat{\omega}(k+1) \end{bmatrix} = \begin{bmatrix} \hat{\theta}(k) \\ \hat{\omega}(k) \end{bmatrix} - \xi H^{-1} J. \tag{6.7}$$

The newly updated $\hat{\theta}(k+1)$ and $\hat{\omega}(k+1)$ are utilized as initial values for the

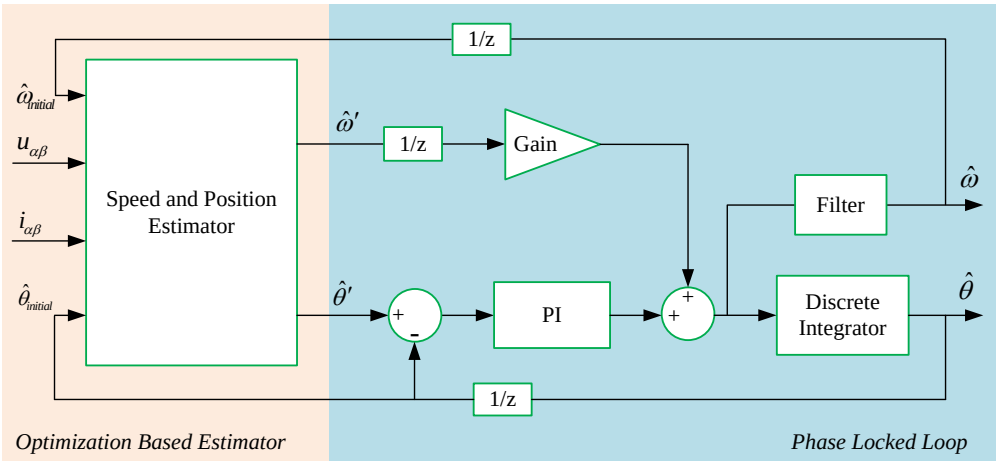


Figure 6.9: Nonlinear optimization based position estimator.

next estimation. The structure of the observer is depicted in the left side of Figure 6.9. Since the estimator issues position and speed estimation based on instantaneous values, current sensor noises directly affect the estimation quality. In order to filter high frequency noises, a PLL is implemented in series with the proposed estimator, as shown in the right side of Figure 6.9. The proposed PLL consists of a PI regulator, a discrete integrator, a speed feed-forward term and a digital filter. The basic theory of the PLL has been introduced in Section 3.2. In the proposed PLL, the speed feed-forward term is used for accelerating the dynamic response and the digital filter is employed for speed ripple reduction. The PLL parameters were tuned empirically by balancing the estimation bandwidth and noise attenuation in experimental tests (Jeong *et al.*, 2005; Jang *et al.*, 2004; Al-nabi *et al.*, 2013). The filtered estimated speed and position are utilized for motor control.

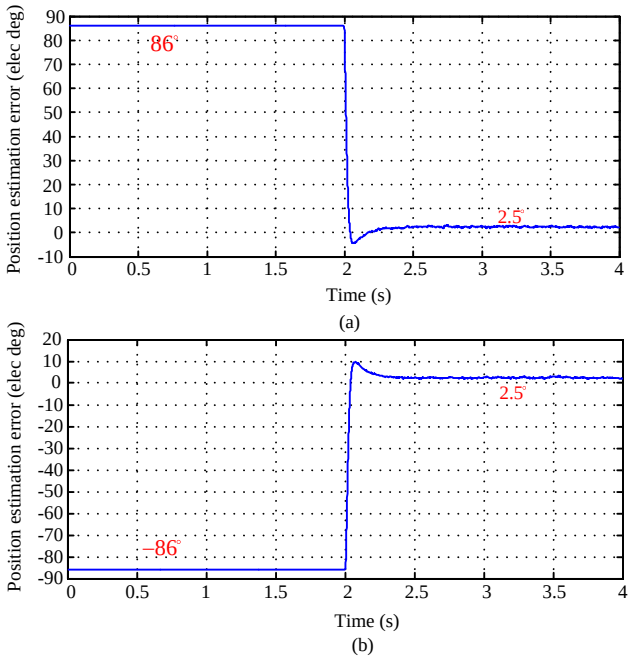


Figure 6.10: Experimental results, convergence tests at standstill condition: (a) positive initial error; (b) negative initial error.

## 6.6 Experimental Verifications

The proposed unified speed and position estimation algorithm was also tested in the prototype experimental test bench. Speed control was implemented in the dyno machine and the prototype IPM motor was under torque control. The $i_\delta$ was controlled to be zero and the $i_\gamma$ was controlled for electromagnetic torque generation. The injection voltage magnitude $V_1$ was 70 V and the speed $N_1$ was set to 400 rpm. The frequency of the injected sinusoidal voltage was 500 Hz.

The position estimation error $\tilde{\theta}$ may increase during the speed or torque transients. The inaccurate initial position estimation method may also lead to a large position estimation error. The robustness of position estimators is reflected in the capability

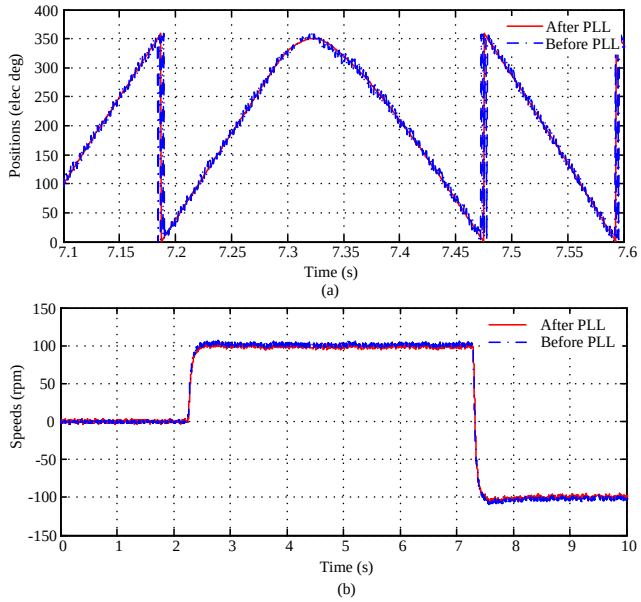


Figure 6.11: Experimental results, speed and position estimation before and after PLL: (a) position estimation at transients; (b) speed estimation.

of converging to the correct estimation from a certain initial estimation error. Figure 6.10 shows the convergence range of the proposed position estimator at standstill condition. With ±86° initial error, the 10%-90% rise time $t_r$ of the estimator was 28 ms for both conditions. The practical bandwidth $f_{bw}$ (Preindl and Bolognani, 2012) is calculated in

$$f_{bw} = \frac{0.34}{t_r}, \tag{6.8}$$

which is 12.14 Hz. The 2% settling time is 0.3 s for both cases. In this chapter, all the tests were under the assumption that the initial position had already been obtained by the proposed method in Chapter 5.

Figure 6.11 shows the speed and position estimations before and after PLL. Figure 6.11 (a) depicts the position estimation when the speed changed from 100 rpm to

-100 rpm. From this figure, it is concluded that the speed and position are able to be estimated by the optimization based estimator without PLL. However, the involvement of PLL reduces the noises especially in the position estimation and improves the estimation quality.

Figure 6.12 depicts the speed and position estimation with a 50 rpm speed step change. The motor was at standstill condition and then the speed reference increased to 50 rpm and then reduced to -50 rpm. Figure 6.12 (a), (b) and (c) illustrate the position estimation error, the position estimation at speed transients and the speed estimation respectively. Without extra load torque, the steady state position estimation error is within 3° in electrical degree.

The test in Figure 6.12 was repeated with 20% and 40% rated torque applied by the IPM motor respectively. As shown in Figure 6.13 (a) and Figure 6.14 (a), the maximum average steady state estimation errors increase to $-5°$ with 20% rated torque and $-10°$ with 40% rated torque. At low speed, the proposed position estimator relies more on the position information contained in $L_a\big(\theta(k)\big)$, which employs constant inductance values. When the torque related $\gamma$ axis current is increased in Figure 6.13 and Figure 6.14, the position estimation errors increase due to the cross-saturation effect (Guglielmi *et al.*, 2006). This torque related error can be compensated by involving a current dependent correction term mentioned in (Li *et al.*, 2009).

In Figure 6.15, the 40% rated torque was added on the shaft and the motor was tested with 100 rpm speed transients. In Figure 6.14 and Figure 6.15, the steady state position estimation errors at 0 rpm, 50 rpm and 100 rpm with same electromagnetic torque are $-10°$, $-8.5°$ and $-1.5°$. Since the back-emf components become more

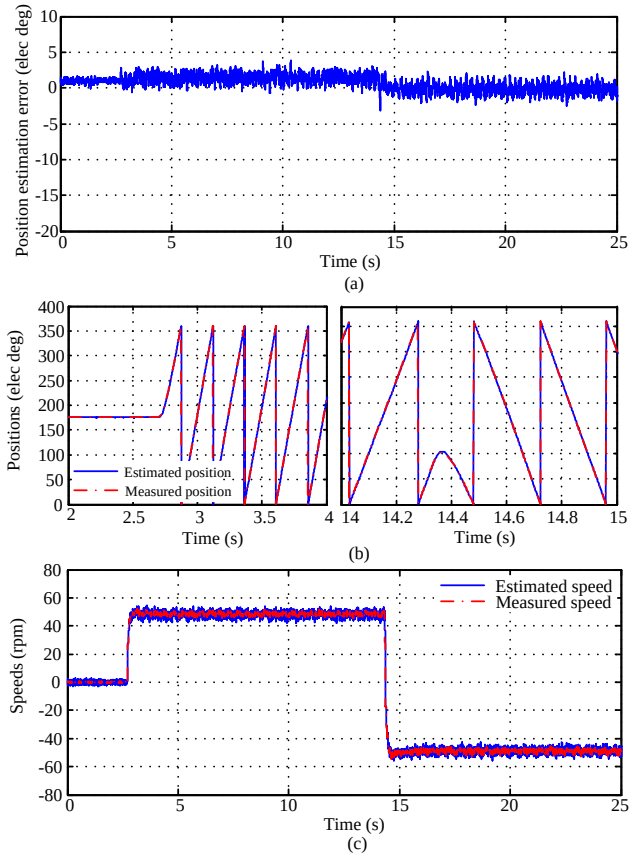


Figure 6.12: Experimental results, speed step change without load, 50 rpm: (a) position estimation error; (b) position estimation at transients; (c) speed estimation.

significant as the speed increases, the position estimation error is reduced at higher speeds with the same torque applied on the shaft.

In Figure 6.16, the motor was running at 300 rpm. The electromagnetic torque changed from 76% rated torque to $-76\%$ rated torque. The torque change is reflected from the change in $i_\gamma$. The maximum transient estimation error is within 15° electrical degree and the steady state estimation error is within 2.5°. Compared with Figure 6.14 and Figure 6.15, the transient and steady state position estimation errors are smaller with heavier torque. This is due to the increase of the back-emf which is

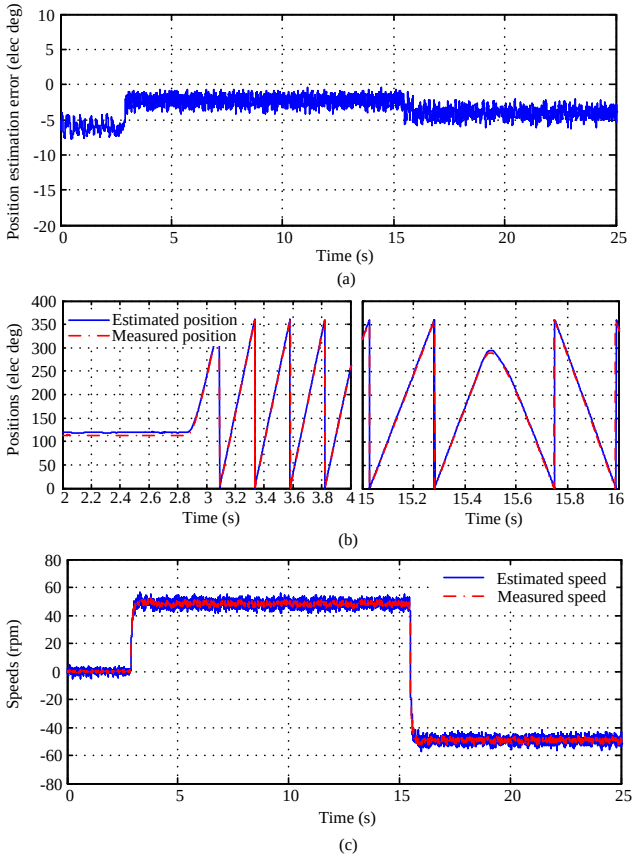


Figure 6.13: Experimental results, speed step change with 20% rated torque, 50 rpm: (a) position estimation error; (b) position estimation at transients; (c) speed estimation

proportional to the motor speed.

Figure 6.17 illustrates the capability of sensorless operation at wide speed range. The motor speeds changed between different positive and negative values. The transitions between low speed (with injection and modified cost function (6.5)) and high speed (without injection and with original cost function (6.4)) are smooth. The steady state position estimation error is within $\pm 5^\circ$ electrical degree.

Figure 6.18 shows the speed and position estimation at wide speed range including standstill. The initial position error was $160^\circ$ before estimation. After the initial

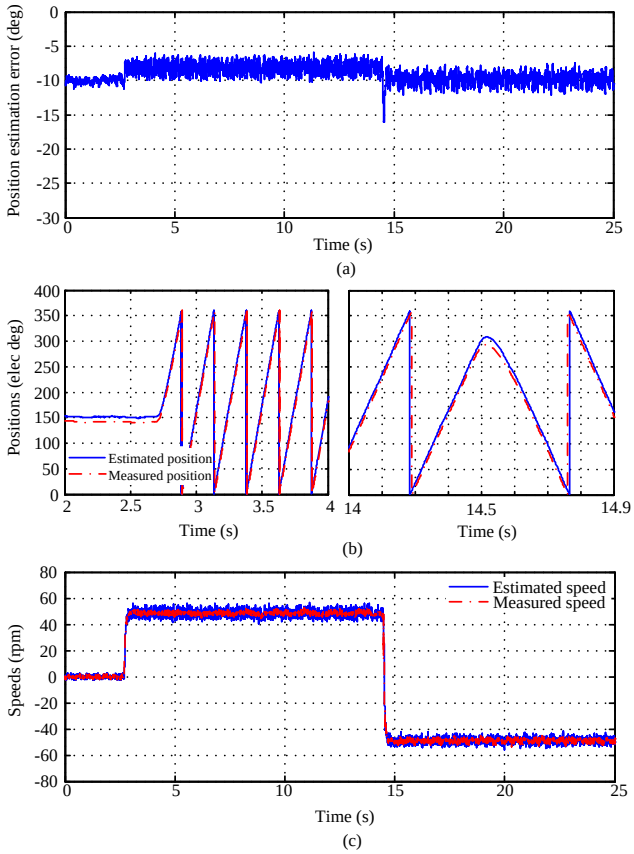


Figure 6.14: Experimental results, speed step change with 40% rated torque, 50 rpm: (a) position estimation error; (b) position estimation at transients; (c) speed estimation

position estimation, the steady state estimation error is 1.5°. The machine speed increased to 100 rpm and then 500 rpm. 76% of the rated torque was applied to the machine shaft when the motor was running at 500 rpm. The steady state position estimation error is less than 3° and the maximum transient position estimation error is less than 20° as shown in Figure 6.18 (a). Figure 6.18 (b), (c) and (d) illustrates the position estimation at transients, $i_\gamma$ and speed estimation respectively. Sensorless control works well in the wide speed range including standstill conditions.

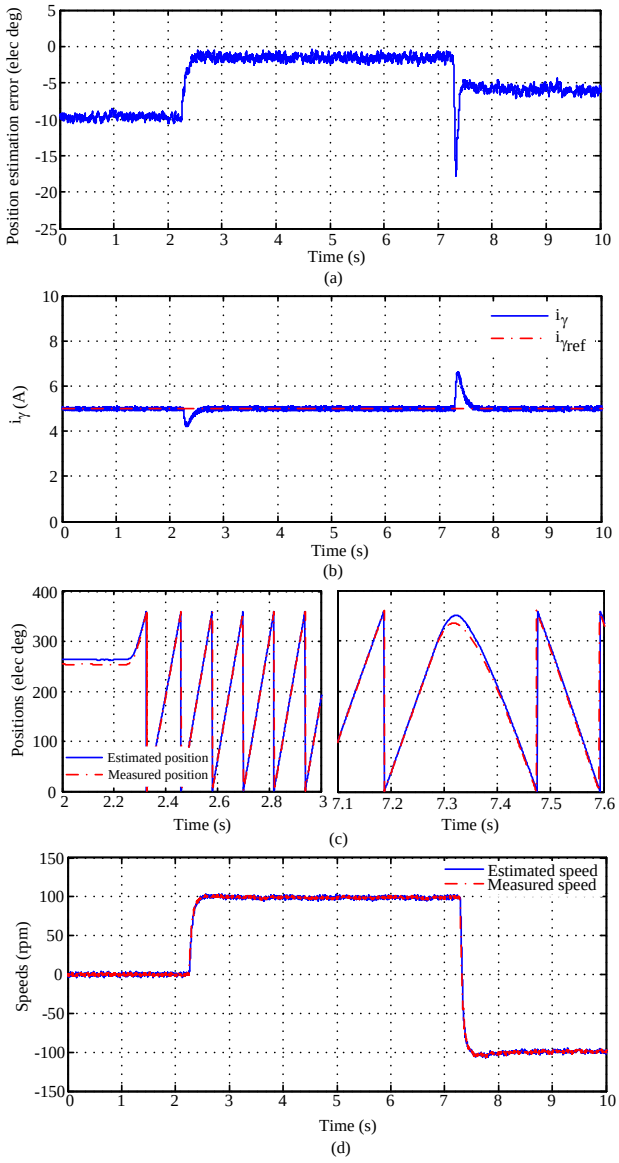


Figure 6.15: Experimental results, speed step change with 40% rated torque, 100 rpm: (a) position estimation error; (b) current in $\gamma$ axis; (c) position estimation at transients; (d) speed estimation.

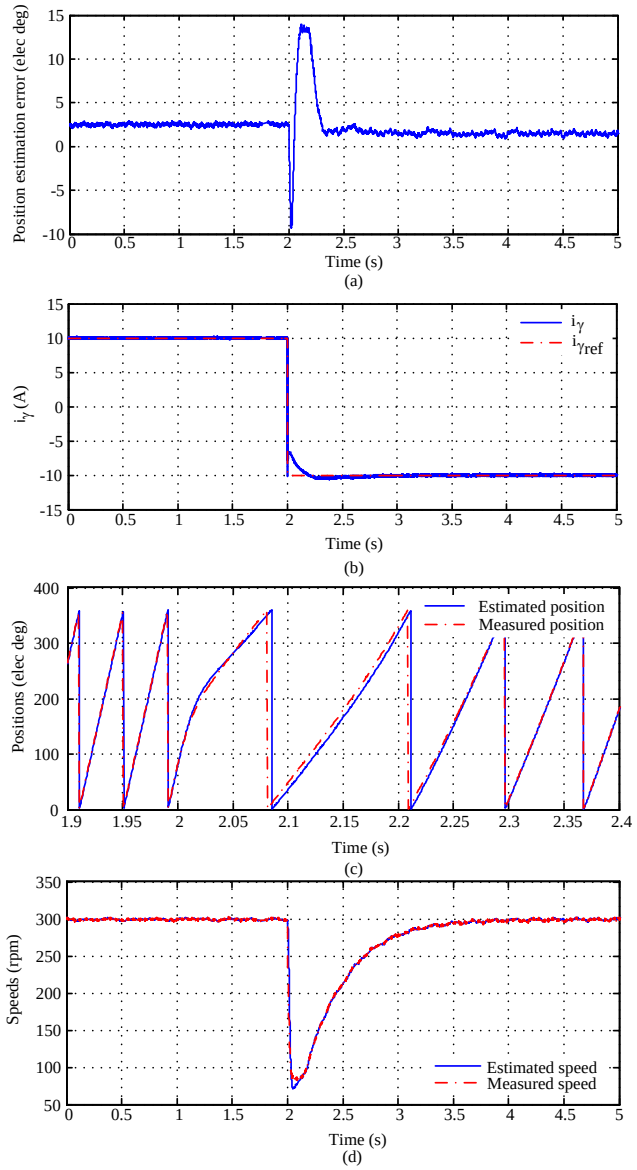


Figure 6.16: Experimental results, torque step change at constant speed, 300 rpm: (a) position estimation error; (b) current in $\gamma$ axis; (c) position estimation at transients; (d) speed estimation.

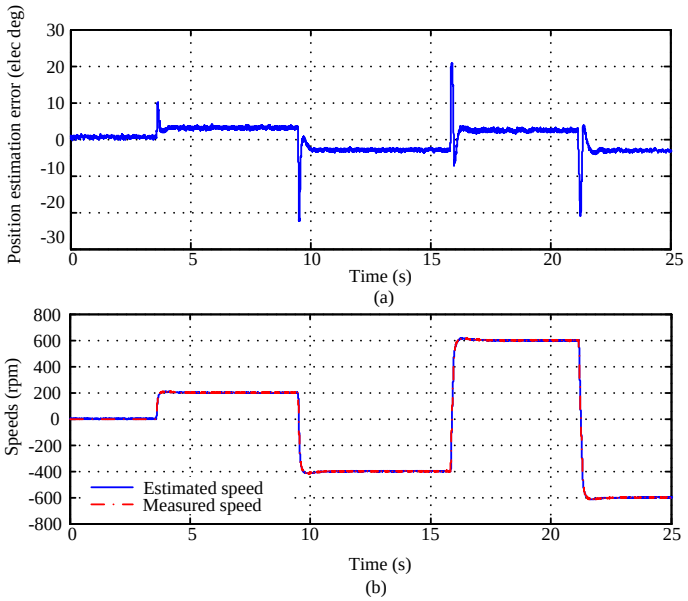


Figure 6.17: Experimental results, wide speed range operation: (a) position estimation error; (b) speed estimation.

## 6.7 Parameter Sensitivity Analysis

In order to better evaluate the robustness of the proposed estimation method, the sensitivity of the motor parameters is analyzed with contour plots in Figure 6.19 and experimental testing results in Figure 6.20. In Figure 6.19, the position estimation errors are analyzed with 50% resistance variation, 50% permanent magnet flux variation and 50% inductance variation (saliency ratio is kept constant) assuming the motor is running at 300 rpm with 40% rated torque. The position estimation errors under those parameter variations are 0°, 0° and 5.7° respectively. In the experimental tests shown in Figure 6.20, the motor was running at 300 rpm and the electromagnetic torque changed from 40% rated torque to −40% rated torque. The position estimation errors due to 50% resistance variation, 50% permanent magnet flux variation and 50% inductance variation with 40% rated torque are 1.5°, 0.5° and 8.5°. Under the

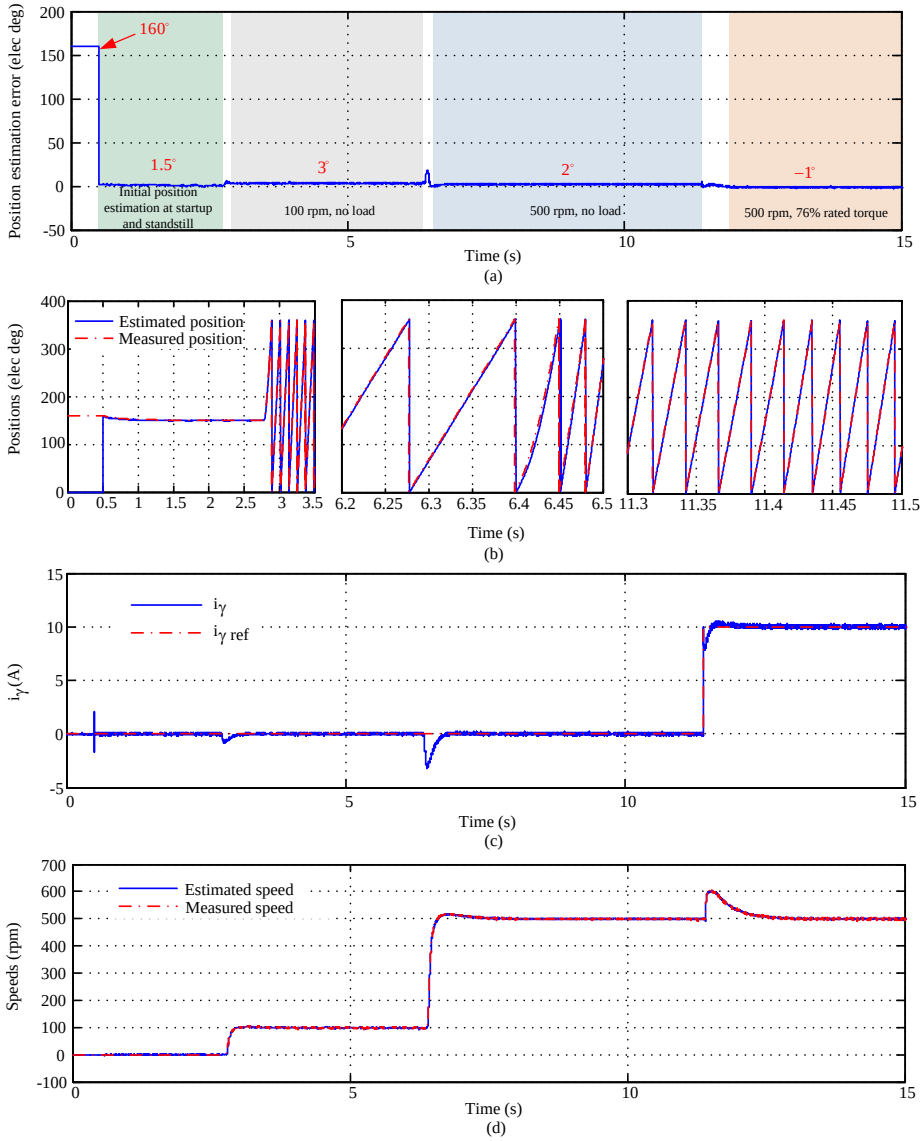


Figure 6.18: Experimental results, speed and position estimation at wide speed range including standstill: (a) position estimation error; (b) position estimation at transients; (c) current in $\gamma$ axis; (d) speed estimation.

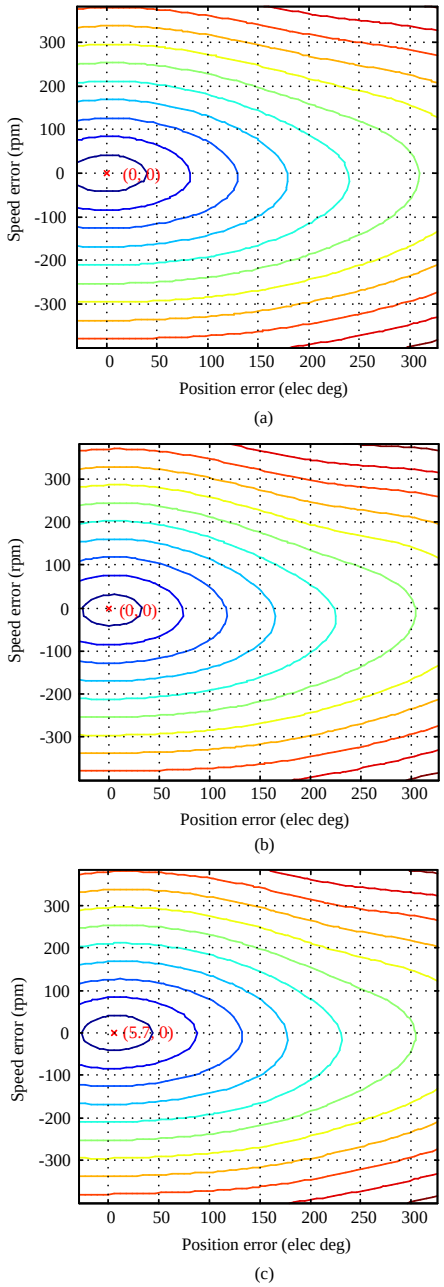


Figure 6.19: Parameter sensitivity contour plot analysis at 300 rpm with 40% rated torque: (a) 50% resistance variation; (b) 50% permanent magnet flux variation; (c) 50% *d*-*q* axes inductances variation.

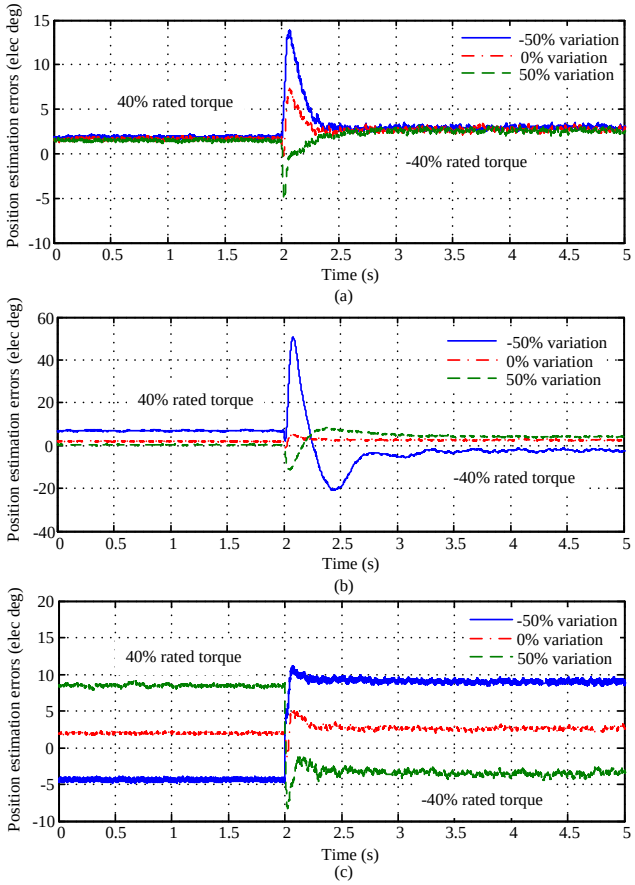


Figure 6.20: Parameter sensitivity experimental test results: (a) ±50% resistance variation; (b) ±50% PM flux variation; (c) ±50% *d*-*q* axes inductances variation.

same test condition, the position estimation errors observed in experiment are larger than those in the theoretical contour plot analysis due to the measurement noise and model mismatch. Besides the 300 rpm and 40% rated torque test condition with 50% parameter variations, the results shown in Figure 6.20 also illustrate the performance of the proposed method at torque transients, −40% rated torque condition and −50% parameter variations. From the results, it is clear that the position estimation errors during the torque transients are larger with ±50% parameter variations than with the

original values. Regarding the steady state estimation accuracy, the proposed estimation method is less affected by the resistance and permanent magnet flux variations. However, the steady state position estimation errors change by around 7° electrical degree with ±50% inductance variations (Sun *et al.*, 2016).

## 6.8 Conclusions

In this chapter, the feasibility of a novel unified nonlinear optimization based speed and position estimation algorithm has been proposed. A cost function is defined based on the voltage equations in the stationary reference frame and the speed and position information can be obtained by minimizing the cost function. At low speed, the cost function is modified and extra high frequency voltage is injected to prevent the singularity at zero speed. Since the position estimator structure remains the same from standstill condition to high speed, a unified speed and position estimator is proposed for the IPM motor drives at wide speed range. The effectiveness of the cost functions has been validated with contour plot analysis and convexity analysis.

The real time implementation of the proposed observer has been introduced and the feasibility of the proposed method has been validated with the prototype IPM motor drive system. The convergence range, performance with different speed and torque transients and the parameter sensitivity analysis have been presented in this chapter. The experimental results demonstrate that the proposed method is capable of estimating the speed and position robustly with high accuracy and fast convergence at wide speed range.

# Chapter 7

# Comparative Assessment of the Proposed Sensorless Approach

## 7.1 Introduction

In pulsating sinusoidal voltage injection (PSVI) based method, the speed and position estimator relies on the BPF, LPF and PLL, which have limited bandwidths respectively. Moreover, the calculation of extended EMF also relies on the previous estimation information in the extended EMF (EEMF) based method. However, each estimation is an independent process in the proposed unified nonlinear optimization (UNOP) based method. Even though the previous estimation information is needed, it just provides the starting point for the optimization but is not involved in the real estimation process at medium and high speed. In the benchmark reference methods, the inputs of the PLL are position estimation errors $f(\tilde{\theta})$. The PLL structure used in the PSVI method and EEMF method in the prototype drive system is modified in Figure 7.1. In the UNOP method, the inputs are the estimated speed and position

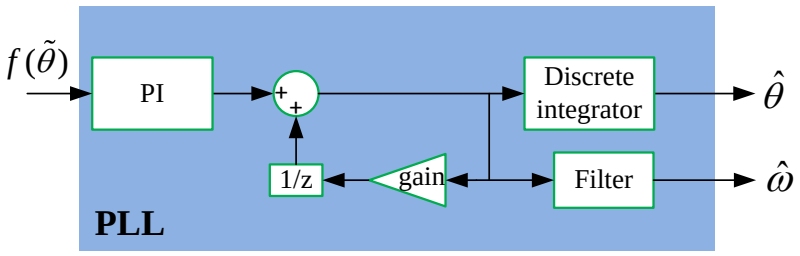


Figure 7.1: The modified PLL used in PSVI and EEMF methods.

instead and the PLL is working as a filter instead of being part of the position estimation. In this way, the transient behavior is faster with the proposed method since it is equivalent to open loop estimation. In order to validate this point, the performance of the proposed unified sensorless method is compared with benchmark reference methods at wide speed range including standstill condition in this chapter. The comparisons were undertaken under same test conditions and with the same experimental test bench. Additionally, the proposed cost functions are capable of involving machine nonlinearity, dealing with multiple voltage injection types and achieving estimation with low sampling frequency, which is also validated in this chapter. At last, the computational burden of the proposed method is compared with the benchmark reference methods for validating its availability of real time implementation with general micro-controllers.

## 7.2 Improvements in Initial Position Estimation

In this section, the proposed initial position estimation and polarity detection methods are compared with the conventional estimation methods. The capability of involving nonlinear motor parameters in the proposed initial position estimation method is

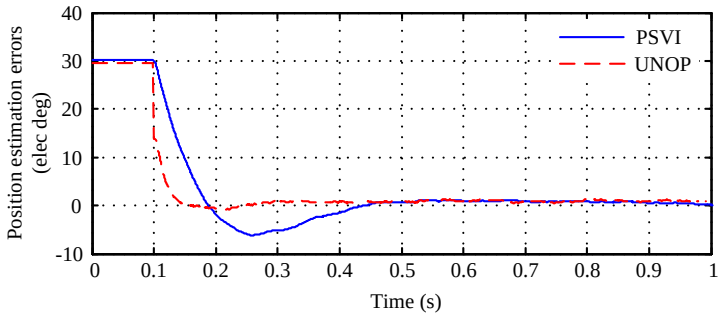


Figure 7.2: Experimental comparison on convergence speed between PSVI method and UNOP method.

also introduced.

### 7.2.1 Dynamic Performance in Initial Position Estimation

In this test, the proposed estimator and the demodulation based estimator used in PSVI method both started from the same initial position error, which was 30° electrical degree. The injected voltage magnitude, the injection frequency and the PLL parameters are identical in the two methods. The position estimation errors are shown in Figure 7.2. The 2% settling time and the 10%-90% rise time of the PSVI method are 0.4 s and 0.07 s. While in UNOP method they are only 0.18 s and 0.03 s respectively.

Figure 7.3 depicts the position estimation performances of the UNOP method and the PSVI method during torque transients. In Figure 7.3 (a), the $i_\gamma$ was controlled to generate 20% rated torque. The steady state position estimation errors are similar in the two methods. However, the PSVI method has a much worse dynamic performance with maximum 22° error and 2 s settling time in Figure 7.3 (a). The similar situation is also obtained in Figure 7.3 (b) when 40% rated torque was applied. The above

tests demonstrate that the proposed position estimator has faster dynamic estimation performance than the demodulation based estimator at standstill. The BPF and LPF in the PSVI method limit the bandwidth of demodulation based position estimator.

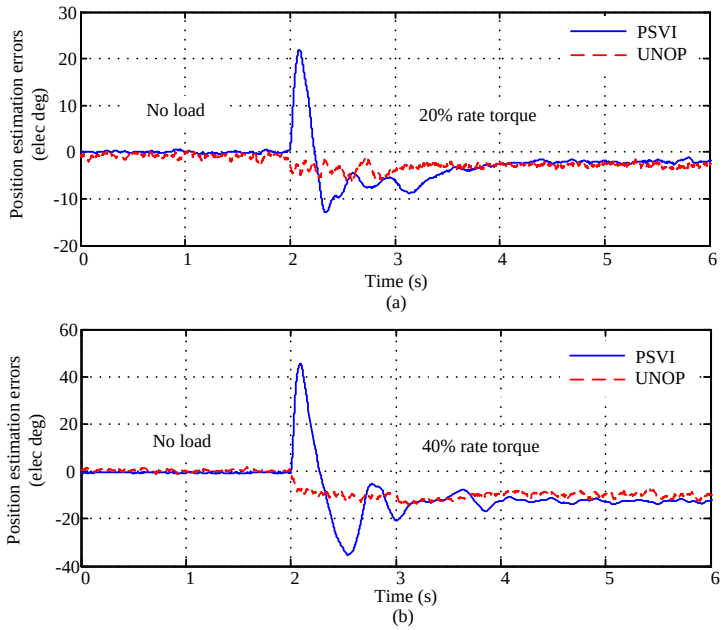


Figure 7.3: Experimental comparison on torque transient performance between PSVI method and UNOP method: (a) 20% rated torque change; (b) 40% rated torque change.

### 7.2.2 Magnetic Polarity Detection

As stated in Section 3.5.2, the conventional dual voltage injection (DVI) based polarity detection method relies on the detection of the current peak difference induced by the positive and negative voltage pulses. This method was also implemented in the prototype motor drives. Figure 7.4 depicts the required resulting currents for robustly detecting the polarity with the proposed method and the DVI method. The injection duration of each voltage vector is $4T_s$ in the proposed method and is $6T_s$ in the DVI

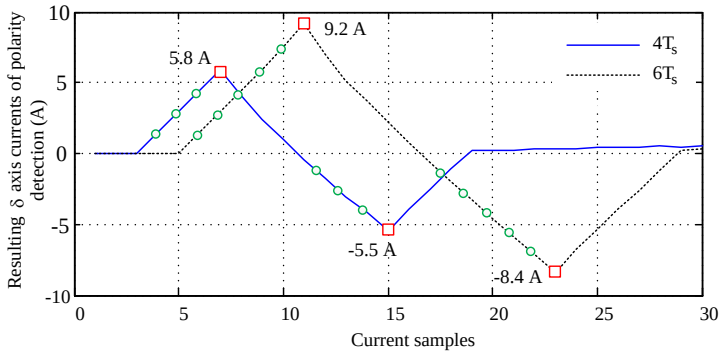


Figure 7.4: Resulting $\delta$ axis currents due to the injection in magnetic polarity detection.

method. In the proposed method, the current difference between the positive peak and negative peak is only 0.3 A. The DVI method couldn't work robustly with this current difference level due to its sensitivity to the measurement noise. The current peak difference becomes larger when the injection duration increases to $6T_s$, with which the DVI method can detect the polarity reliably. However, 0.8 A difference is still not significant enough for many drive systems with larger measurement noise. In order to obtain significant current peak difference, the resulting currents need to be further increased by increasing the injected voltage magnitude or injection duration, which leads to the utilization of higher power rating inverters. Instead of only taking the peak currents in the red squares into account, the proposed polarity detection method involves more current samples (green bubbles), which concern the shape of the current responses. Since the shape of the resulting currents reflects the nonlinear properties of the machine, the proposed polarity detection method can detect the polarity with lower currents and the robustness is enhanced compared with the DVI method.

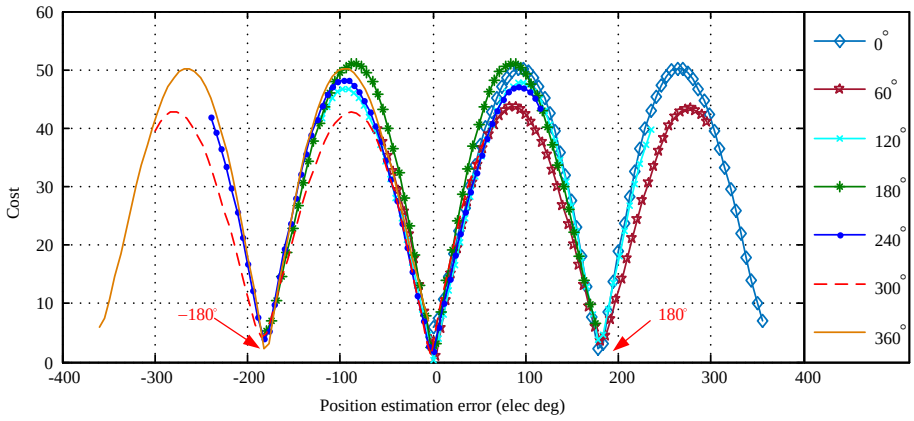


Figure 7.5: Plot of $\bar{G}_i(\hat{\theta})$ versus position estimation errors at different initial positions for $m = 1$ using experimental data.

### 7.2.3 Involvement of Machine Nonlinearity in Initial Position Estimation

In Section 4.3, the flux linkage profiles in $d$-$q$ axes were measured from experiment. The derived nonlinear inductance profiles in (4.3) can also be used in initial position estimation. If the constant $L_{dq}$ are replaced by those nonlinear inductance profiles, the cost function (5.5) is rewritten as

$$\begin{aligned} \underset{\hat{\theta}}{\text{minimize}} \quad \bar{G}_i(\hat{\theta}) = \sum_{k=1}^{m} \Big\| & T_{dq}(\hat{\theta})\bar{u}_{\alpha\beta}(k) \\ & - \frac{1}{T_s}\nabla_{i_{dq}}\ell_{dq}\big(T_{dq}(\hat{\theta})i_{\alpha\beta}(k+1)\big)T_{dq}(\hat{\theta})\big(i_{\alpha\beta}(k+1) - i_{\alpha\beta}(k)\big)\Big\|^2. \end{aligned} \tag{7.1}$$

A similar plot of the cost function (7.1) as Figure 5.5 is shown in Figure 7.5. With nonlinear inductance profiles involved, the cost function also has two local minimums which locate around 0° error and 180° error in one electrical period. The initial position can be estimated by the line search approach utilized in Chapter 5. Even

though the costs are smaller at 0° error than those at 180° error, the difference is not significant if the measurement noises are taken into account in the real time implementation. Hence, the magnetic polarity detection is still necessary if (7.1) is employed for position estimation in Step I. Moreover, the nonlinear inductance profiles are not used in Step III in initial position estimation and running state estimation due to the increased computation burden caused by the interpolation of look-up tables in the real time implementation with 10 KHz sampling frequency.

As stated in Chapter 5, the maximum magnitude of the injected voltages for both position estimation and polarity detection was 200 V due to the restriction of the DC link voltage. When the magnitude of the injection voltage is fixed, the injection duration can be adjusted to achieve higher resulting currents. The position estimation accuracy by linear method (using constant parameters in cost function (5.5)) and nonlinear method (using nonlinear inductance profiles in cost function (7.1)) were tested when $m \in [3\ 5]$ at different initial positions in one electrical period. The results are shown in Figure 7.6 and Figure 7.7. From the comparison of the two figures, it is clear to see that the position estimation accuracy improves as the increase of the injection duration. The improvement of the estimation accuracy with the linear method is not as significant as the accuracy improvement with the nonlinear method.

Additionally, estimation accuracies of the linear and nonlinear methods are also compared with the same injection duration ($5T_s$) in Figure 7.8. In the figure, the peak error and average error in the nonlinear method are 15° and 7.15° respectively. Both the peak error and average error in the linear method are larger, which are 28.8° and 10.77°. Moreover, the estimation accuracies of the nonlinear method are also higher than those of linear method with other injection durations ($3T_s$ and $4T_s$), which are

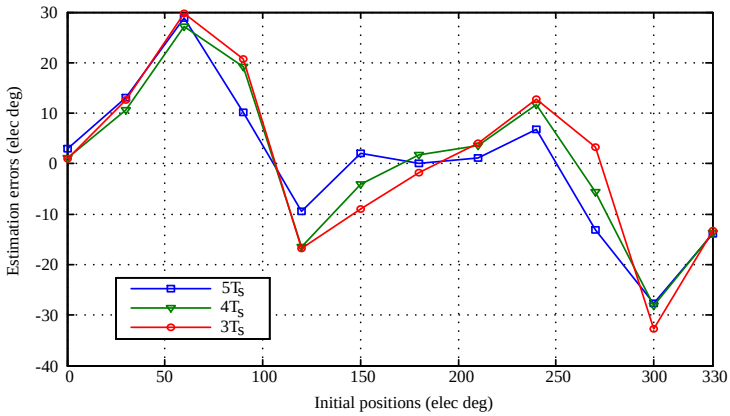


Figure 7.6: Position estimation errors of the linear method at different initial positions with different injection durations.

summarized in Table 7.1.

The nonlinear method mentioned in this section can be used for initial position estimation in Step I when the nonlinear flux linkage profiles are available. So this method is heavier parameter dependent and needs more computation source compared with the linear method. Moreover, even though the estimation accuracy is improved by involving machine nonlinearities, the estimation accuracy is still large compared with the accuracy after Step III in Chapter 5 due to the inverter nonlinearity. So the linear method is chosen as the proposed initial position estimation

Table 7.1: Position Estimation Accuracy Comparison

| Injection durations for each voltage vector (ms) | 0.3 | 0.4 | 0.5 |
|---|---|---|---|
| Average estimation error of linear method (elec deg) | 13.14° | 11.92° | 10.77° |
| Average estimation error of nonlinear method (elec deg) | 12.5° | 10.27° | 7.15° |
| Peak value of current pulse in per unit value | 0.39 | 0.52 | 0.69 |

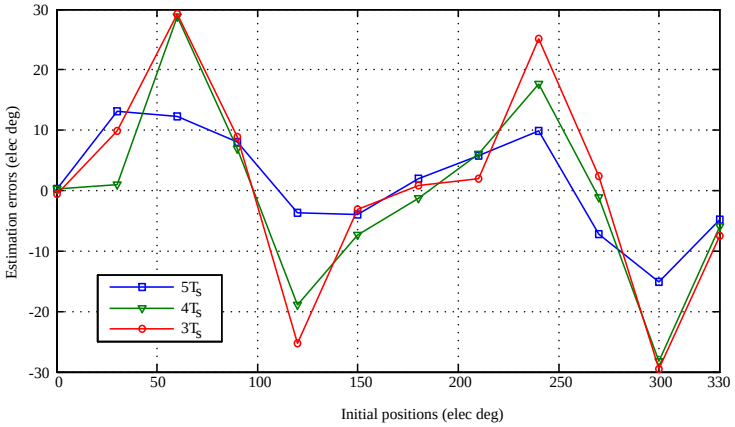


Figure 7.7: Position estimation errors of the nonlinear method at different initial positions with different injection durations.

method in this thesis. However, the nonlinear method still demonstrates its capability of involving nonlinear motor parameters in the cost functions for improving the estimation accuracy.

## 7.3 Improvements in Speed and Position Estimation at Running State

### 7.3.1 Dynamic Performance at Low Speed

In order to benchmark the proposed speed and position estimation algorithm at low speed, the same test in Figure 6.14 was duplicated by the PVSI method. The bandwidth of the PLL used in PSVI method was tuned to be 36 times larger than that of the PLL used in proposed position estimator, in order to achieve similar bandwidths with the proposed method in speed and current responses. The variable magnitude

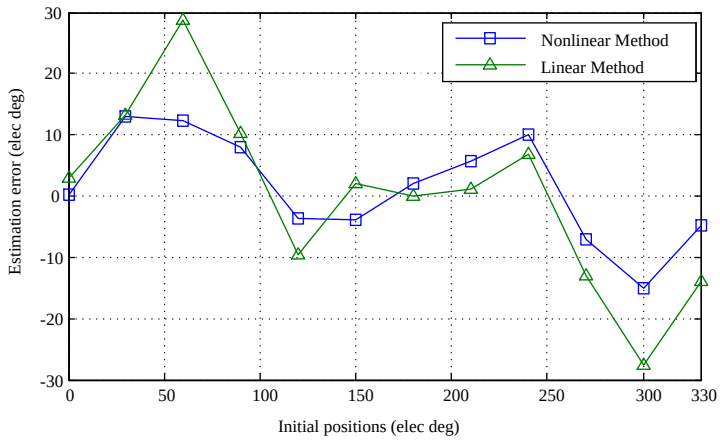


Figure 7.8: Estimation accuracy comparison between nonlinear and linear methods ($5T_s$ for each voltage pulse).

injection method can't be applied to the PSVI method due to the fact that the estimation solely relies on the injection frequency components. Reducing the injection voltage magnitude will affect the estimation since the carrier frequency current reduces accordingly. However, both the fundamental frequency components and carrier frequency components are utilized for estimation in the proposed method, so the injection voltage can be reduced as the motor speed increases. Hence, the injected voltage magnitude has to be kept constant at 70 V in the PSVI method at low speed. For the testing results of the PSVI method in Figure 7.9 (a), the 2% settling times of the speed step change from 0 to 50 rpm and from 50 rpm to negative -50 rpm are 4.3 s and 5.6 s respectively. While in the UNOP method, the settling times are only 0.1 s and 0.15 s shown in Figure 6.14 (a). The settling times of the UNOP method are 40 times shorter than those of the PSVI method. The comparison also shows that the UNOP method has lower transient and steady state position estimation error. The maximum transient error is $-26°$ with PSVI method and is $-16°$ with the UNOP method. The estimated speed ripple is smaller with the UNOP method (10 rpm peak

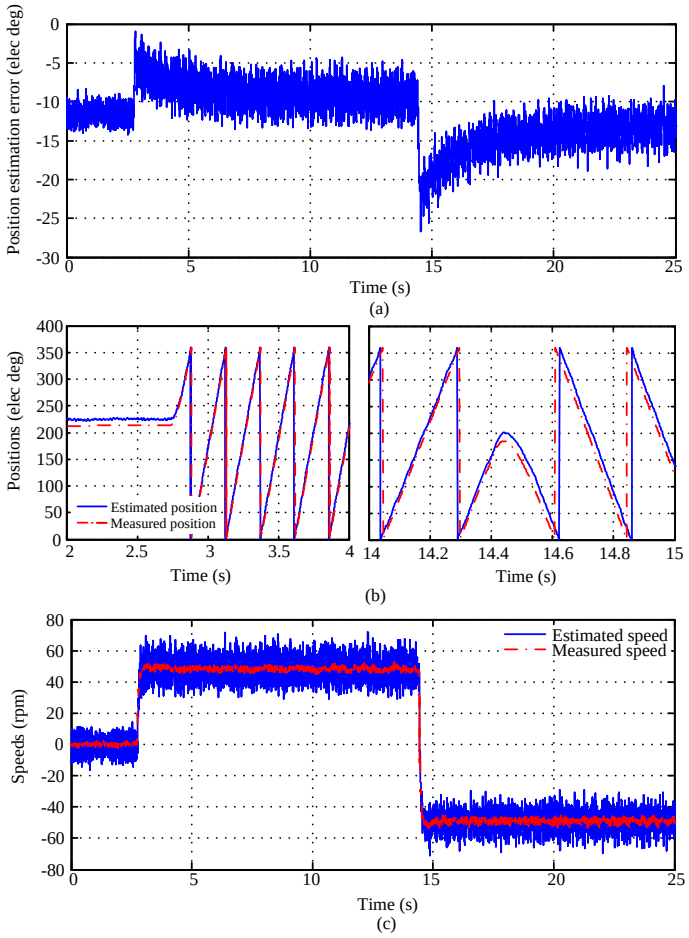


Figure 7.9: Benchmark reference, speed and position estimation with PSVI method with the same test shown in Figure 6.14: (a) position estimation error; (b) position estimation at transients; (c) speed estimation.

to peak) than that with the PSVI method (30 rpm peak to peak), which is illustrated in Figure 6.14 (c) and Figure 7.9 (c). Hence, it can be concluded that the UNOP method outperforms the PSVI method that uses demodulation for speed and position sensing at low speed.

Besides the speed transients, the estimation performance of the UNOP method and PSVI method were also compared in the torque transient tests and the results are illustrated in Figure 7.10 and Figure 7.11. In this test, the motor was running

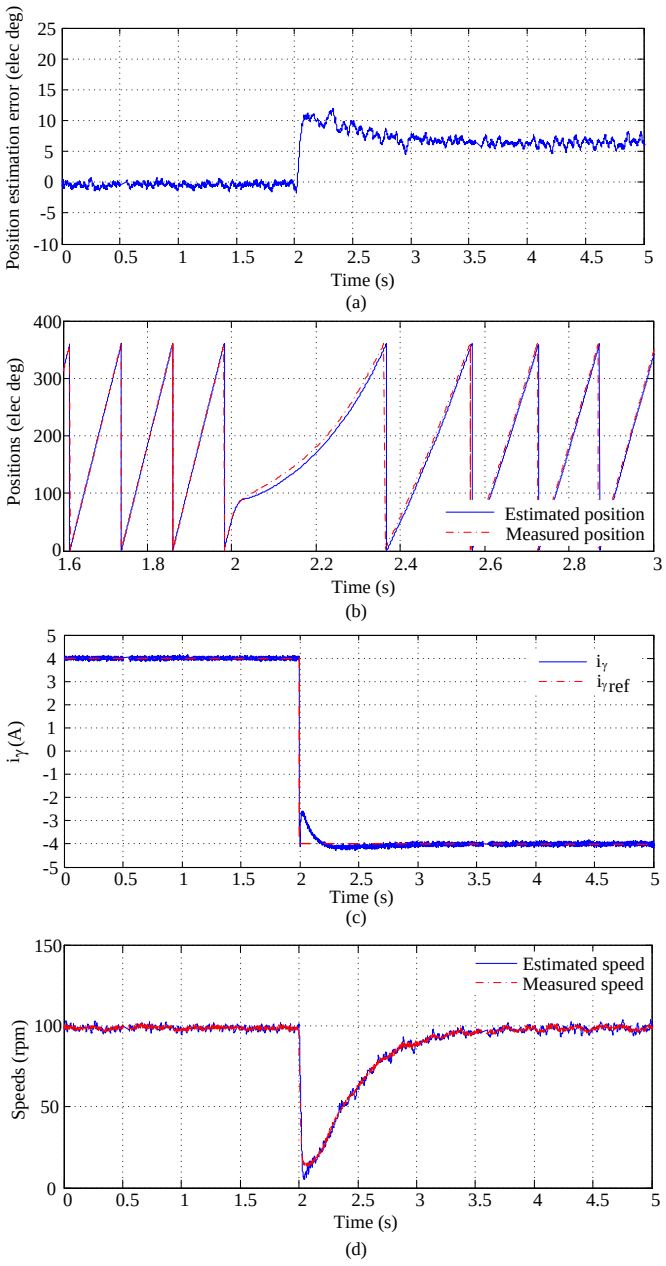


Figure 7.10: Experimental results of the UNOP method at low speed, torque step change at 100 rpm: (a) position estimation error; (b) position estimation at transients; (c) current in $\gamma$ axis (d) speed estimation.

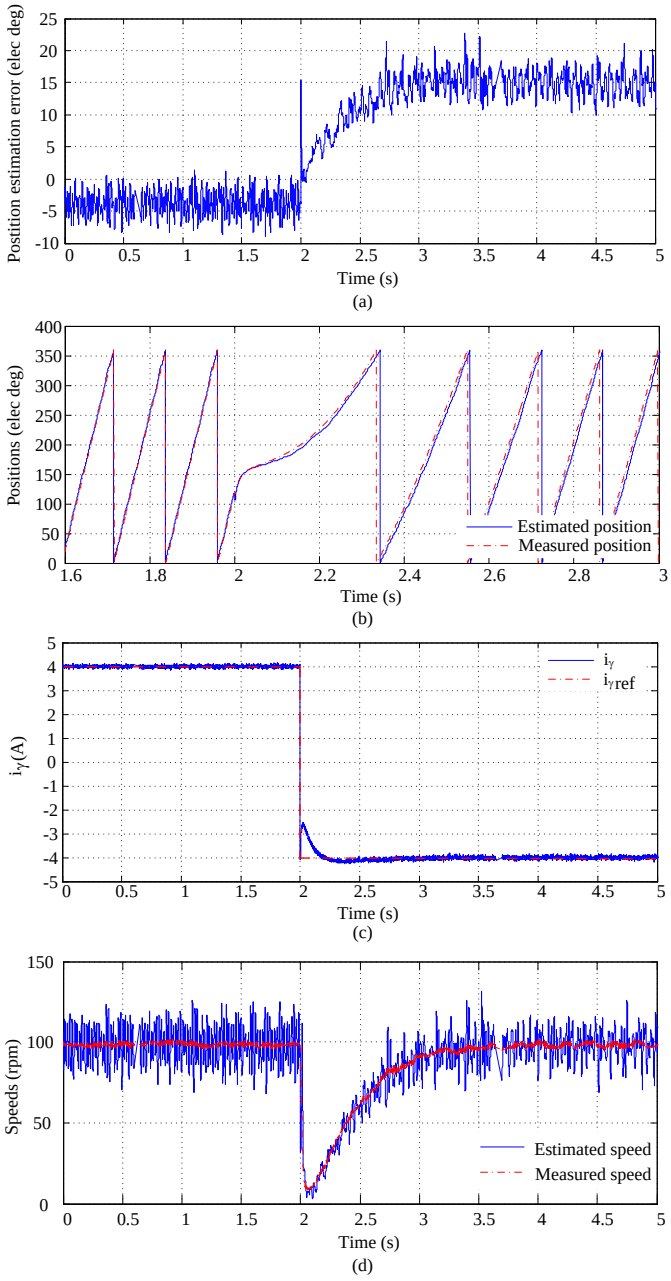


Figure 7.11: Benchmark reference, PSVI base method at low speed, torque step change at 100 rpm: (a) position estimation error; (b) position estimation at transients; (c) current in $\gamma$ axis; (d) speed estimation.

at 100 rpm and the electromagnetic torque was controlled to change from 30% rated torque to −30% rated torque. The similar tracking performance is obtained in the current and speed transients in Figure 7.10 and Figure 7.11. However, the larger position estimation ripple, the larger steady state position estimation error and the larger estimated speed ripple are obtained in the PSVI method.

### 7.3.2 Dynamic Performance at High Speed

At high speed, the estimation performance of the proposed method is compared with the EEMF method. The bandwidth of the PLL used in EEMF method was tuned to be 22 times larger than that of the PLL used in proposed position estimator, in order to achieve similar bandwidths with the proposed method in speed and current responses. Figure 7.12 and Figure 7.13 illustrate the experimental results when the motor speed increased from 400 rpm to 600 rpm with 15% rated torque. The 2% settling times for the EEMF method and the UNOP method are 5 s and 0.7 s respectively. The settling time of the proposed method is 7.1 times shorter than that of the benchmark reference in this test. The maximum transient position estimation error is 8.7° in the EEMF method and is only 2.4° in the UNOP method.

Figure 7.14 and Figure 7.15 depict the experimental results when the torque changed from 30% rated torque to −30% rated torque at 400 rpm. The 2% settling times for the EEMF method and the UNOP method are 1s and 1.2 s respectively. The maximum transient position estimation error is −4.5° in the EEMF based method and is 10° in the UNOP method. In this test, the transient error is larger in the UNOP method. However, the ripples of the estimated speed and position are much larger in EEMF method than those in the proposed method. Moreover, the UNOP

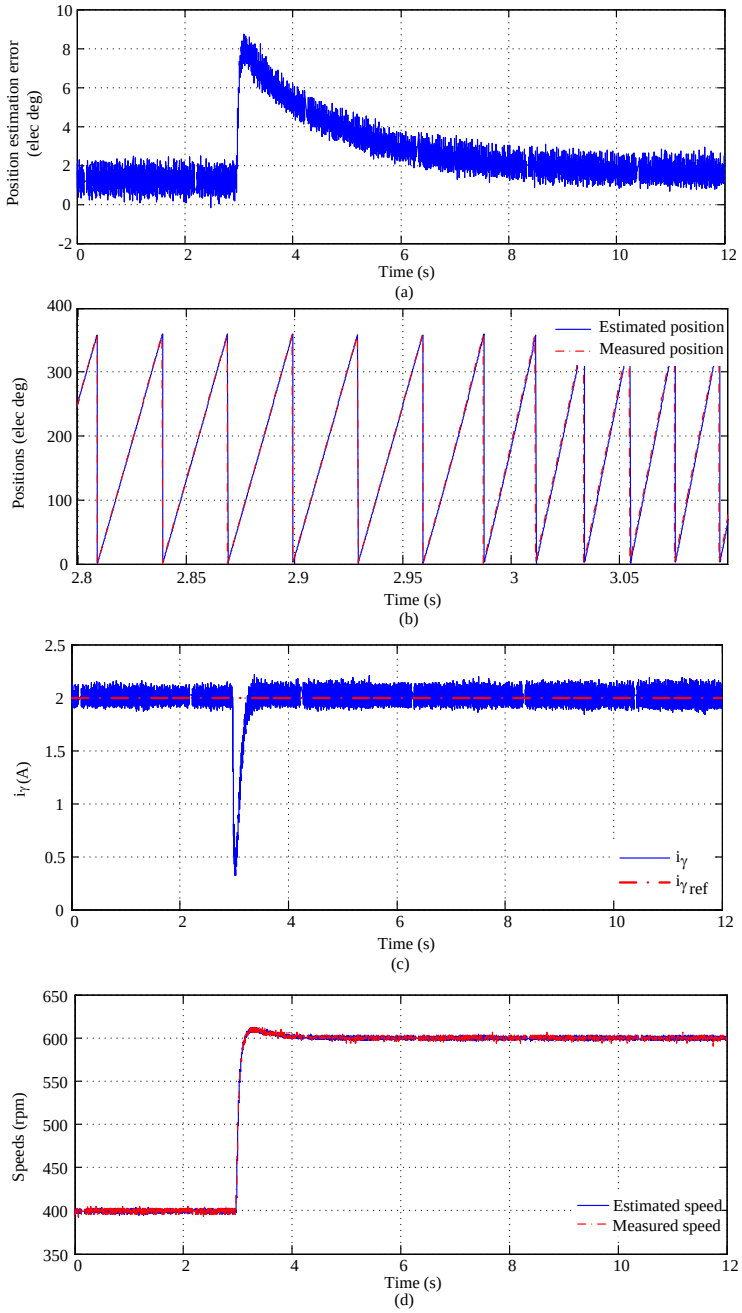


Figure 7.12: Benchmark reference, EEMF base method at high speed, speed step change with 15% rated torque: (a) position estimation error; (b) position estimation at transients; (c) current in $\gamma$ axis; (d) speed estimation.

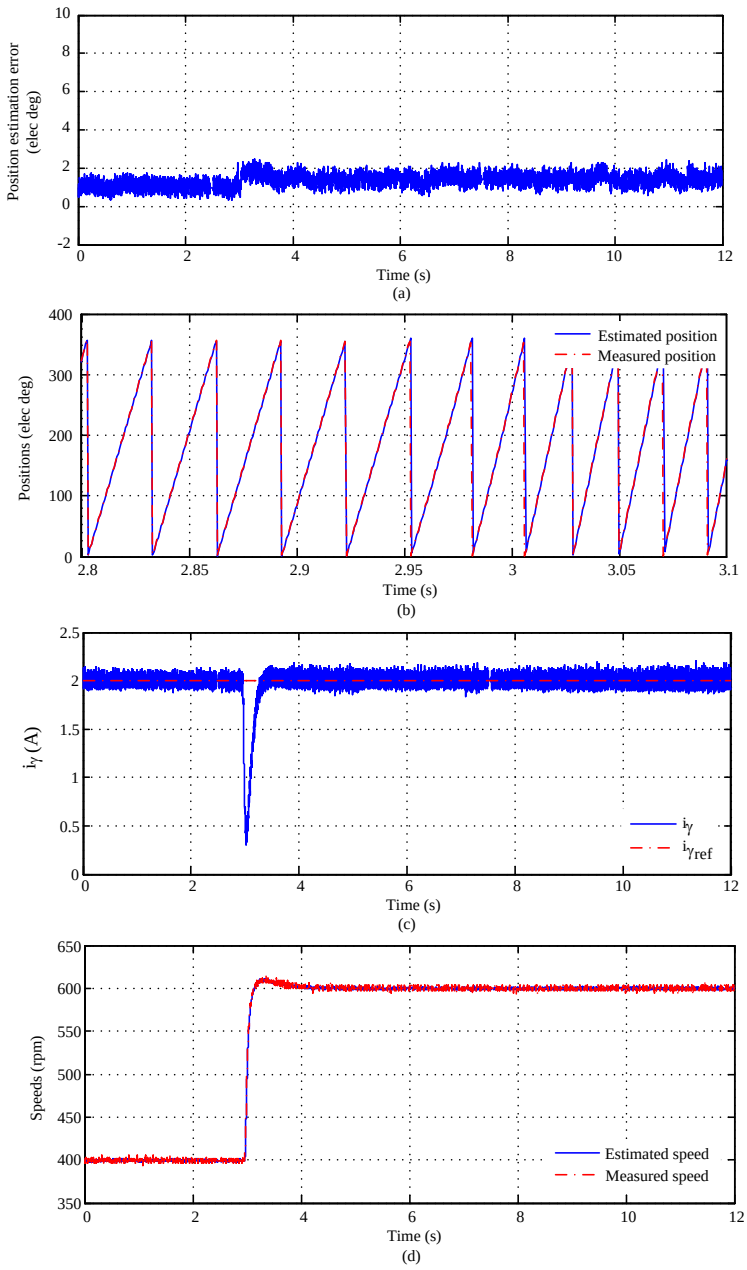


Figure 7.13: Experimental results of the UNOP method at high speed, speed step change with 15% of rated torque: (a) position estimation error; (b) position estimation at transients; (c) current in $\gamma$ axis; (d) speed estimation.

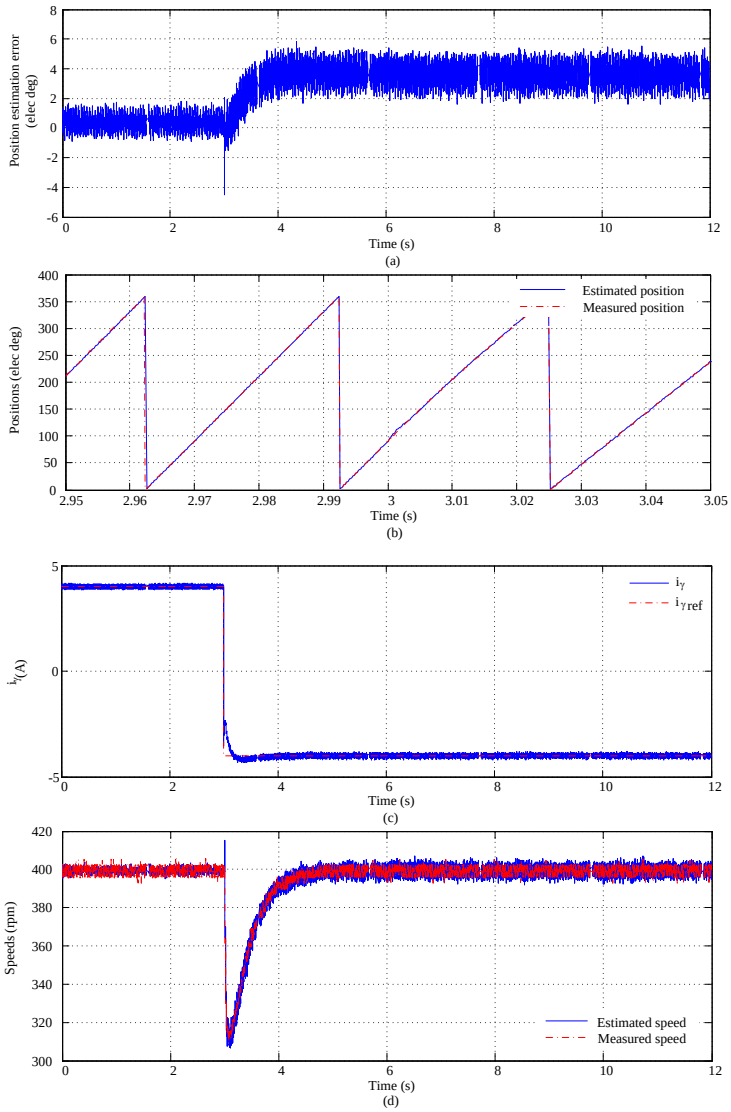


Figure 7.14: Benchmark reference, EEMF base method at high speed, torque step change at 400 rpm: (a) position estimation error; (b) position estimation at transients; (c) current in $\gamma$ axis; (d) speed estimation.

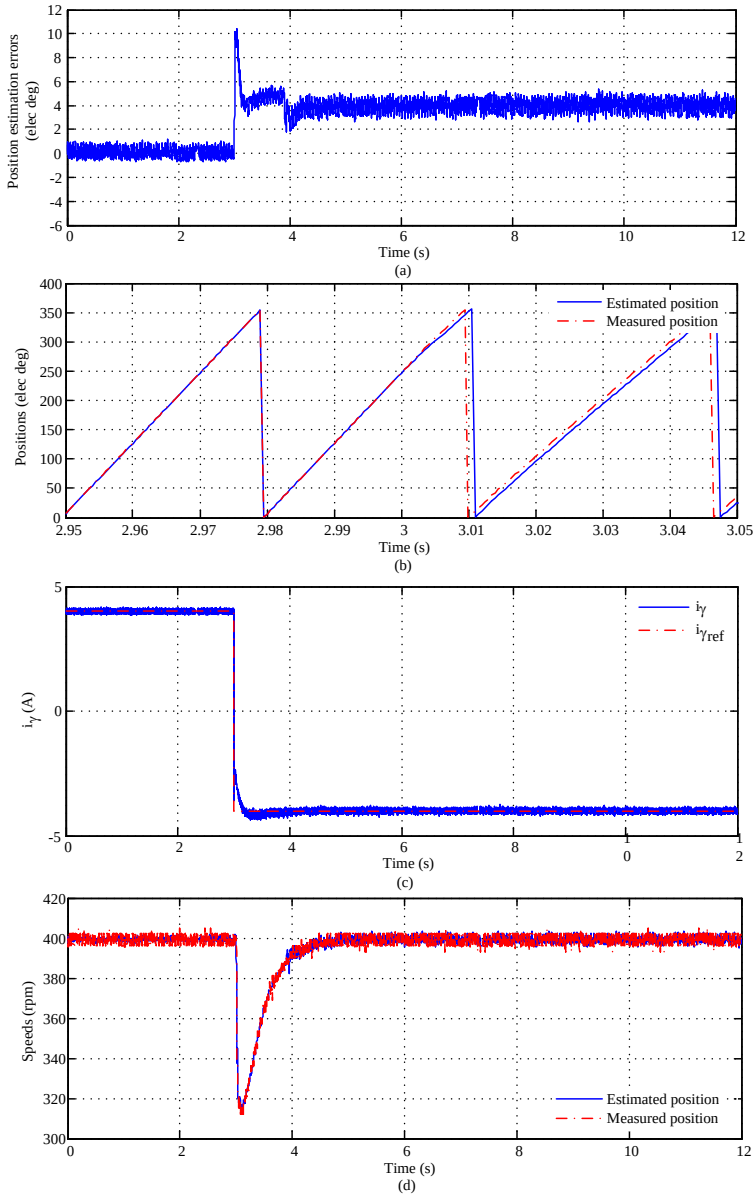


Figure 7.15: Experimental results of the UNOP method at high speed, torque step change at 400 rpm: (a) position estimation error; (b) position estimation at transients; (c) current in $\gamma$ axis; (d) speed estimation.

method is more reliable with larger torque step change. For example, the same test shown in Figure 6.16 was also implemented with the EEMF method. However, the estimation failed due to the divergence of the estimator during the torque transients.

### 7.3.3 Switch Between Low Speed and High Speed

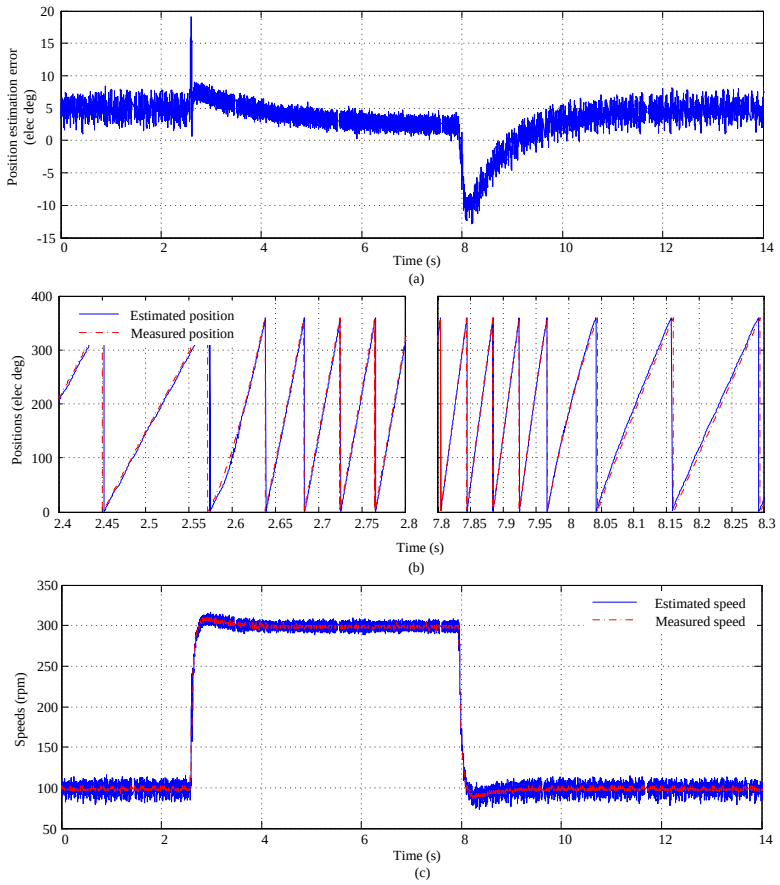


Figure 7.16: Benchmark reference, the combined method during switch process, speed step change without load: (a) position estimation error; (b) position estimation at transients; (c) speed estimation.

In Section 3.4, the wide speed range sensorless method which combines low speed

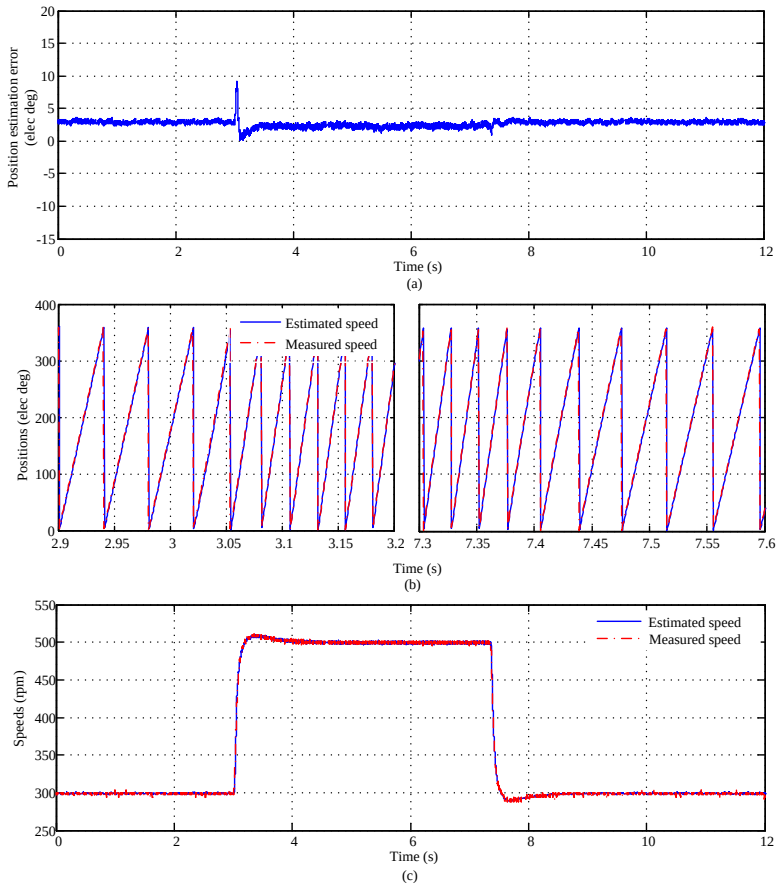


Figure 7.17: Experimental results of the proposed unified method during switch process, speed step change without load: (a) position estimation error; (b) position estimation at transients; (c) speed estimation.

and high speed estimation algorithms was introduced. In the sensorless control system shown in Figure 3.6, there are two position estimators and two PLLs with different parameters. While in the proposed sensorless control system, only one position estimator is needed. As mentioned in Section 7.3.1, the variable magnitudes high frequency voltage injection can not be applied to the PSVI method. Hence, the choice of the switch speed is different in the reference combined method and the proposed UNOP method. The $N_1$ and $N_2$ were selected as 150 rpm and 190 rpm in the reference

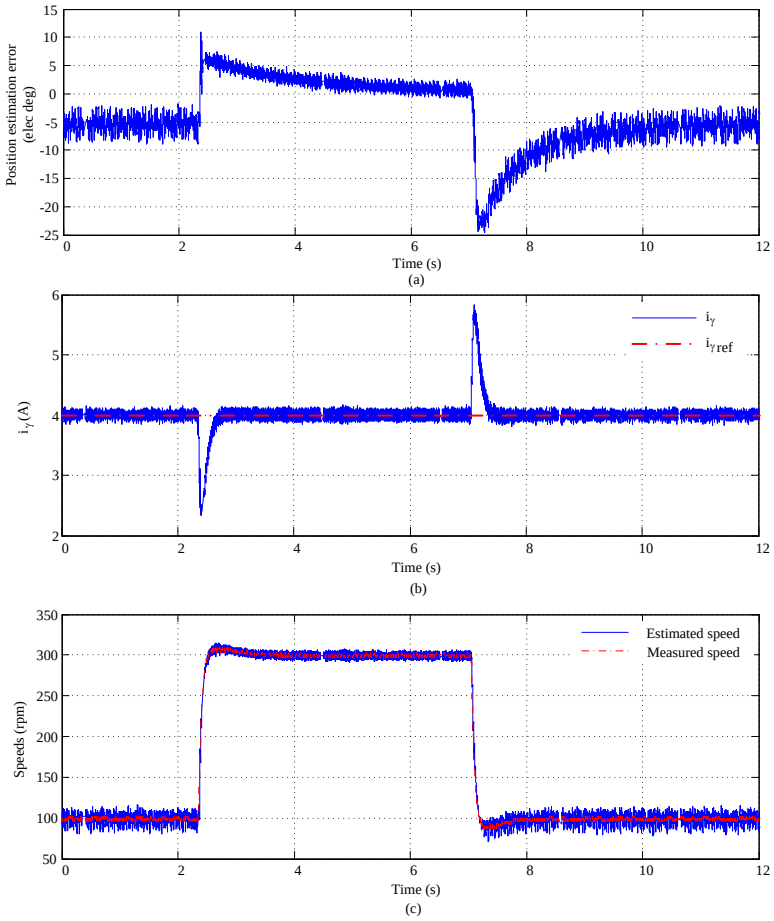


Figure 7.18: Benchmark reference, the combined method during switch process, speed step change with 30% rated torque: (a) position estimation error; (b) current in $\gamma$ axis; (c) speed estimation.

combined method while the $N_1$ in the proposed UNOP method was 400 rpm. Figure 7.16 to Figure 7.19 show the experimental results of the reference combined method and the proposed UNOP method during the switch process with 0% torque and 30% rated torque. The proposed method outperforms at faster dynamic response speed, lower average steady state position estimation error and lower maximum transient position estimation error. Moreover, the sensorless control system is greatly simplified by employing only one unified method from standstill condition to high speed

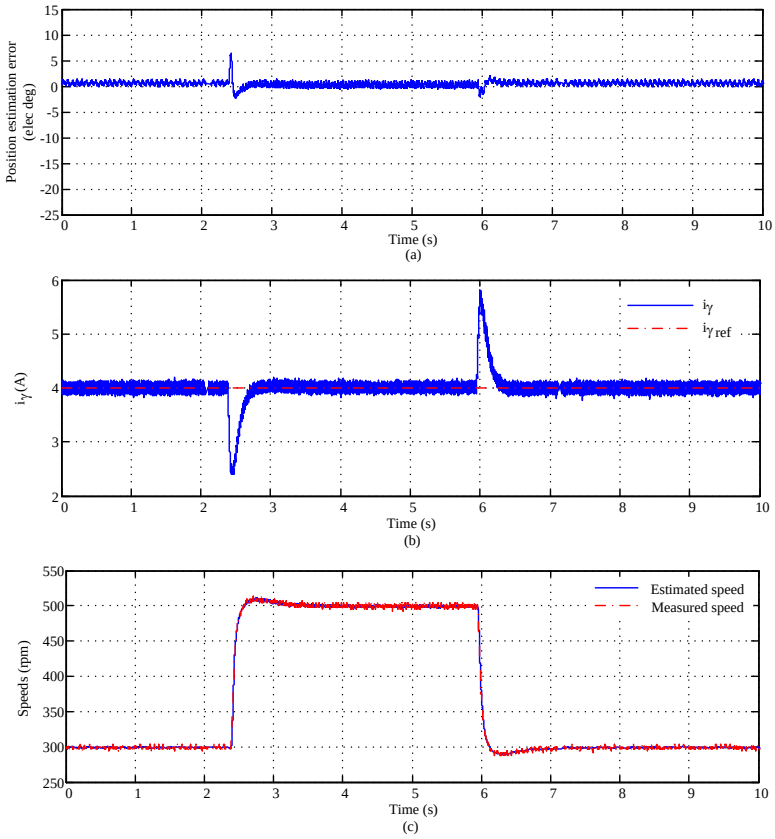


Figure 7.19: Experimental results of the proposed unified method during switch process, speed step change with 30% rated torque: (a) position estimation error; (b) current in $\gamma$ axis; (c) speed estimation.

operation instead of utilizing two different position estimators.

## 7.4 Capability of Speed and Position Estimation with Multiple Injection Types

In Step III of initial position estimation, the proposed optimization based method is capable with sinusoidal injection as well as other injection types, i.e. rectangular voltages. In (Kondo *et al.*, 1995; Jeong *et al.*, 2005; Bolognani *et al.*, 2011; Aihara

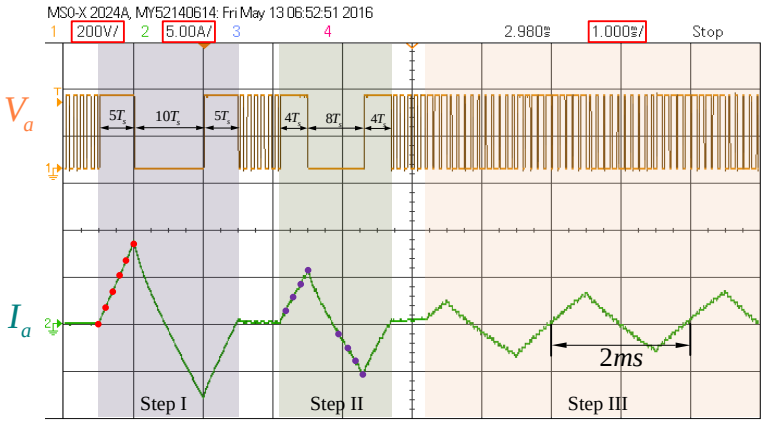


Figure 7.20: Screenshot of the scope, continuous rectangular voltage injection in Step III.

*et al.*, 1999; Foo *et al.*, 2010; Gong and Zhu, 2013; Kim *et al.*, 2012; Yoon *et al.*, 2011; Murakami *et al.*, 2012; Park and Kim, 2014; Zaim *et al.*, 2014; Huang *et al.*, 2014), the demodulation methods for sinusoidal injection and rectangular injection were different. However, a unified position estimation algorithm for different voltage injection types is achieved by using the proposed optimization based estimator. Figure 7.20 illustrates the screenshot of scope when continuous rectangular voltage was injected in Step III. The initial position estimation performances are similar in Figure 5.13 with sinusoidal injection and Figure 7.21 with rectangular injection.

Besides the initial position estimation, the rectangular voltage injection can also be employed at wide speed range operations as shown in Figure 7.22. In Figure 7.22 (a), the actual initial position was -178°. After the initial position estimation, the steady state estimation error is 2°. The machine speed increased to 100 rpm and then to 500 rpm. The 76% rated torque was applied to the machine shaft when the motor was running at 500 rpm. The steady state position estimation error is less than 2° and the maximum transient position estimation error is less than 20°. Figure

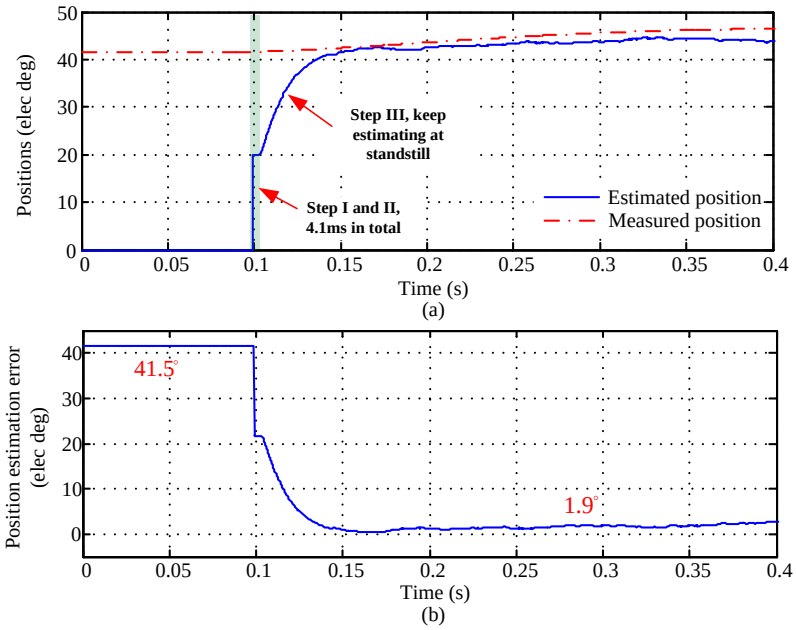


Figure 7.21: Experimental results on initial position estimation at 41.5° with rectangular voltage injection: (a) measured and estimated positions; (b) position estimation error.

7.22 (b), (c) and (d) illustrates the position estimation at transients, $i_\gamma$ and speed estimation respectively. The proposed sensorless control method proves to be valid with rectangular voltage injection at wide speed range.

## 7.5 Capability of Speed and Position Estimation with Low Sampling Frequency

Estimating speed and position with low sampling frequency is attractive for high power AC motor drives, which is challenging for the signal injection based estimation methods at low speed. These methods rely on the demodulation of the carrier

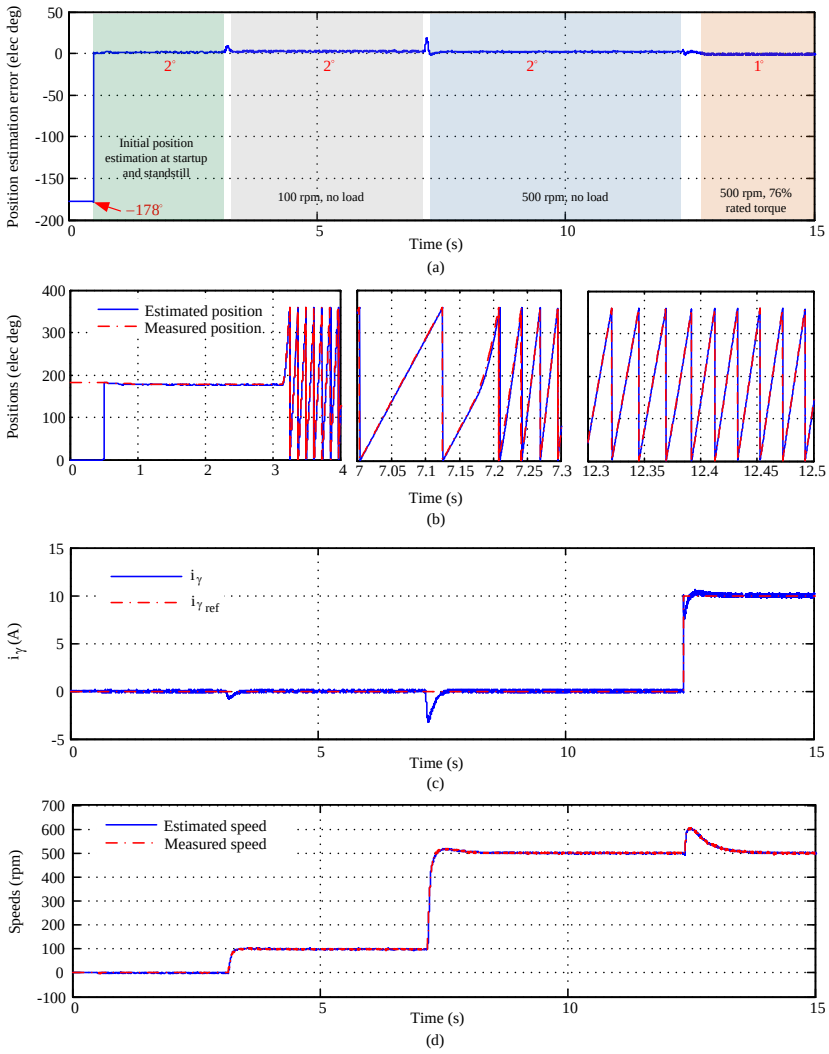


Figure 7.22: Experimental results, speed and position estimation with continuous rectangular voltage injection: (a) position estimation error; (b) position estimation at transients; (c) current in $\gamma$ axis; (d) speed estimation.

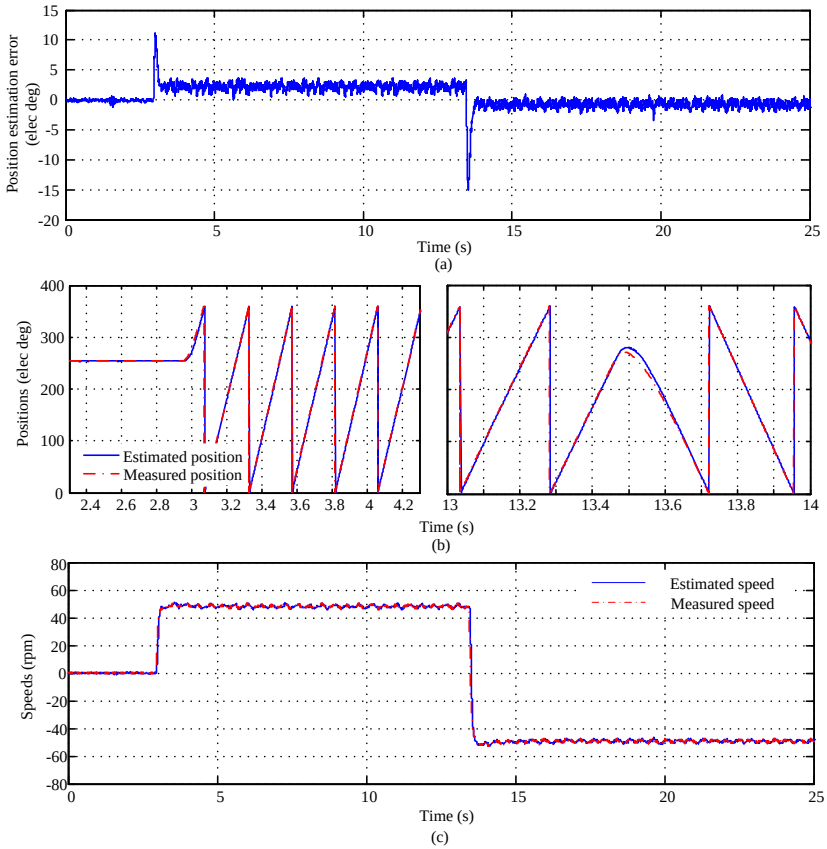


Figure 7.23: Experimental results, speed and position estimation with 2 KHz sampling frequency, no load: (a) position estimation error; (b) position estimation at transients; (c) speed estimation.

frequency components that usually have much higher frequency than the fundamental frequency components. In the benchmark PSVI method, the frequency of the injected sinusoidal voltage is 500 Hz. If the sampling frequency is 10 KHz, the sinusoidal waveform can be sampled properly. However, if the sampling frequency is reduced to 2 KHz, then there are only 4 samples in each sinusoidal period, which will affect the estimation greatly. The demodulation based method failed to extract the speed and position information in the prototype motor drive system with 2 KHz sampling frequency while the proposed method manages to deliver the estimation.

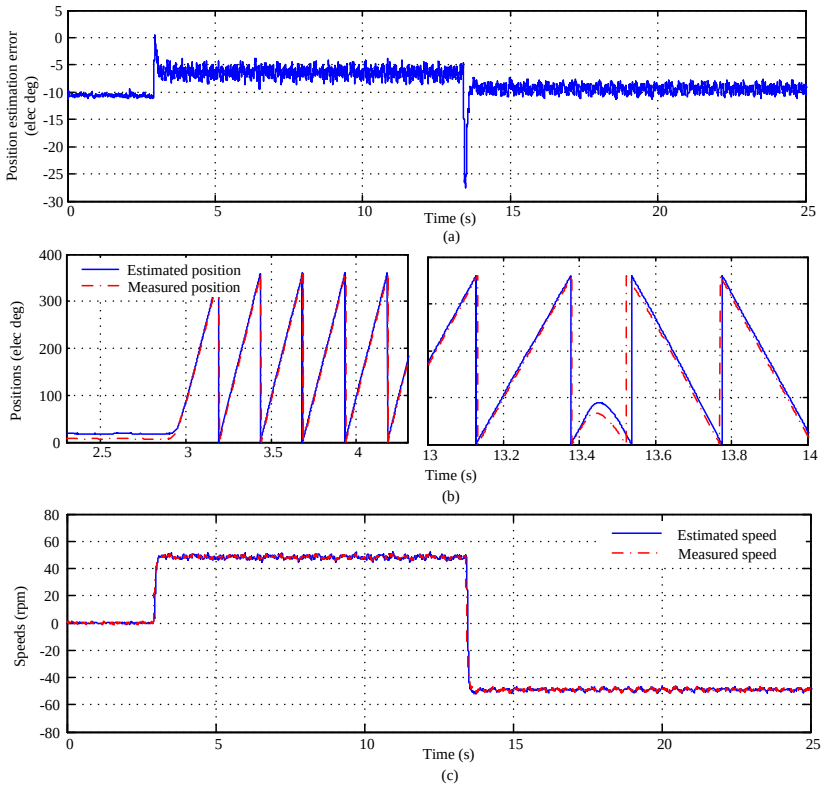


Figure 7.24: Experimental results, speed and position estimation with 2 KHz sampling frequency, with 40% rated torque: (a) position estimation error; (b) position estimation at transients; (c) speed estimation.

Figure 7.23 and Figure 7.24 depict the speed and position estimation results of the proposed method with 2 KHz sampling frequency. The testing conditions were consistent with Figure 6.12 and Figure 6.14. From the comparison, it is clear that the transient position estimation error increases with 2 KHz sampling frequency than that with 10 KHz sampling frequency. But the steady state estimation performance is similar in the two tested sampling frequencies. As mentioned in Section 7.2.3, involving nonlinear motor parameters at running state estimation with 10 KHz sampling is challenging with the micro-controller used in the prototype motor drive system. Nevertheless, reducing the sampling frequency to 2 KHz would help in utilizing the

nonlinear inductance profiles in the running state speed and position estimation.

## 7.6 Computational Burden Analysis

The online optimization technique used in the real time implementation of the proposed method was introduced in Section 6.5. A certain number of iterations are both needed in searching the optimal coefficient $\xi$ and the minimum cost in a certain decent direction in Step III and running state estimation. The maximum iterations that the MicroAutoBox II can handle with 10 KHz sampling frequency is 18 iterations and the minimum iteration number is 1. The computational burden is reflected in the turnaround time (TAT) of the control system. The TATs of the proposed method with maximum and minimum iterations are 85 $\mu s$ and 33 $\mu s$ respectively. The TAT of the benchmark reference method is 29 $\mu s$, which is close to the proposed method with minimum iteration.

The performances of the UNOP method with maximum iterations and minimum iteration were compared with the benchmark reference method at machine startup. The injected voltage magnitude, the injection frequency and the PLL parameters are identical in the proposed method and the benchmark reference. In Figure 7.25, the proposed estimator and the demodulation based estimator both started from the same initial error, which was 30° in this case. From the results, it is clear that the 10%-90% rise time and the 2% settling time are very close with maximum and minimum iterations in the proposed method, which are 0.03 s and 0.18 s respectively. The similar performance with maximum and minimum iterations is due to the execution of the online optimization in 10 KHz. The 10%-90% rise time and the 2% settling time in the benchmark reference method are 0.07 s and 0.4 s respectively.

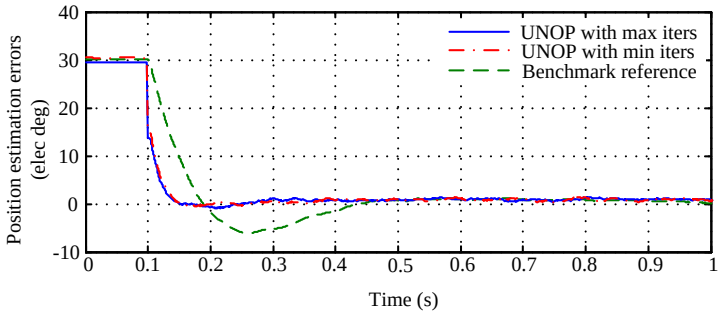


Figure 7.25: Estimation performance validation with different iterations, convergence test with 30° initial error.

The estimation performances of the proposed method with maximum and minimum iterations and the benchmark reference method during speed and torque transients are compared in Figure 7.26. The test conditions in Figure 7.26 (a) and (b) illustrate the speed and torque transients respectively. The bandwidth of the PLL used in the benchmark reference method is 36 times larger than that used in the proposed method. From the comparison, it is concluded that the proposed method with minimum iteration has similar performance with maximum iterations. Moreover, the TAT of the proposed method with minimum iteration is close to that of the benchmark reference method. But the UNOP method outperforms the benchmark reference method both in dynamic response speed and steady state estimation accuracy.

At last, the performance comparisons between the UNOP method, the EEMF method and the PSVI method are summarized in Figure 7.27 in six perspectives, which are convergence speed, reliability, computational burden, conceptual complexity, wide speed range operation capability and low sampling frequency operation capability. The UNOP method outperforms in convergence speed, reliability, capability of wide speed range operation and capability of low sampling frequency operation.

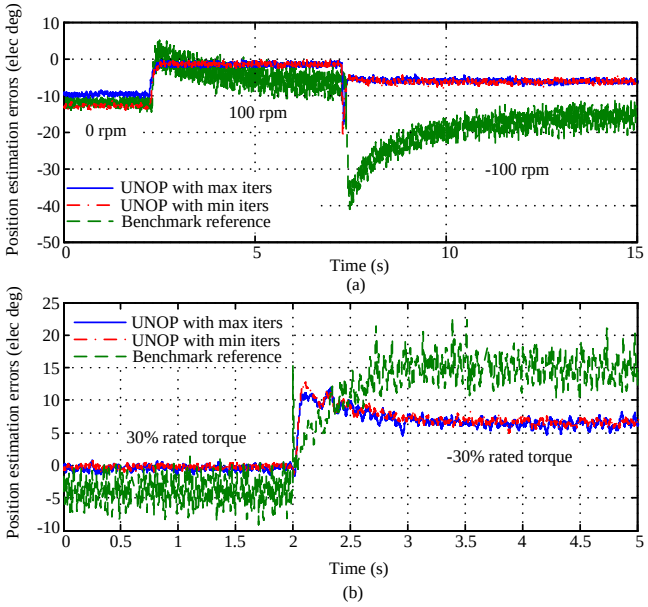


Figure 7.26: Estimation performance validation with different iterations: (a) speed transients; (b) torque transients.

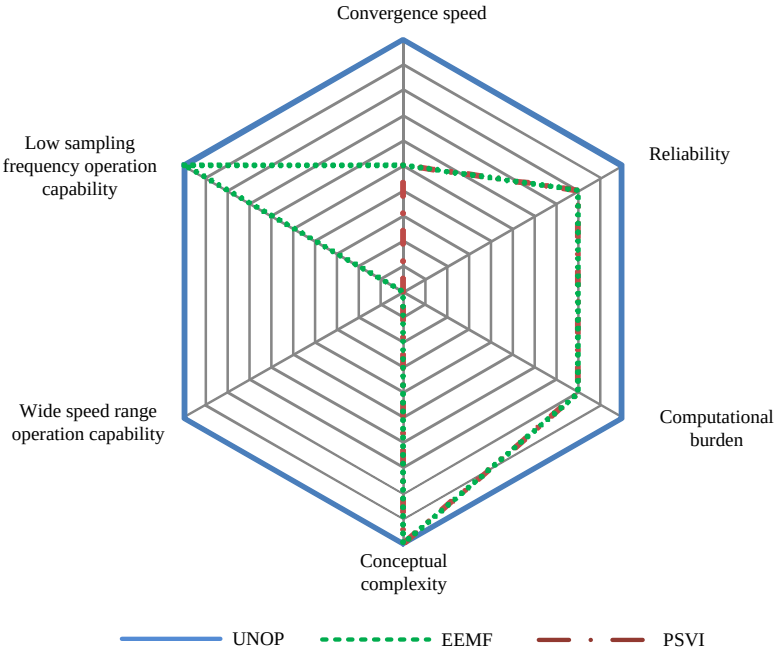


Figure 7.27: Sensorless methods comparison.

## 7.7 Conclusions

In this chapter, the proposed unified speed and position estimation method is compared with the reference combined estimation method on the same experimental test bench. Under the same test conditions, the proposed method outperforms with its excellent dynamic performance and steady state accuracy. Since the proposed method is able to employ both the fundamental frequency components and high frequency components, the sensorless control method is unified at low speed and high speed without involving two different estimators, which greatly reduces the system complexity. Moreover, the cost functions defined in the proposed method are capable of dealing with different voltage injection types and nonlinear motor parameters, which make this method more flexible under different requirements. Additionally, the capability of estimating speed and position with low sampling frequency benefits for involving machine nonlinearity at running state estimation. At last, the computational burden of the proposed method with maximum and minimum iterations is compared with the benchmark reference method. The proposed method with minimum iteration has similar TAT with the benchmark reference but outperforms both in dynamic and steady state performance.

# Chapter 8

# Conclusions and Future Work

## 8.1 Conclusions

In this thesis, a unified speed and position estimation method at wide speed range including standstill has been presented.

A novel nonlinear IPM motor model relying on the current-flux linkage profiles of the prototype machine has been introduced in Chapter 4. The original flux-current profiles were measured experimentally and were inverted to current-flux profiles by employing the proposed LUTs inversion method using nonlinear optimization. This novel model is utilized for the simulation validation of the proposed initial position estimation method and the simulation results match with the experimental results very well.

At machine startup and standstill, an optimization based initial position estimation algorithm has been proposed. A cost function is defined and the initial position can be estimated by searching the minimum of the cost function. Three steps which

employ different voltage injections are utilized. The pulse voltage injection for position estimation benefits from its fast response, but polarity detection and accuracy improvements are still needed. The proposed magnetic polarity detection method generalizes the polarity detection techniques for different IPM motor drives. The polarity can be detected once the differential inductance profile is known. Compared with methods relying solely on saturation, the proposed method requires lower currents to reliably determine the polarity. The continuous voltage injection is used for position estimation at standstill condition after the initial position is roughly obtained. The involvement of continuous injection in Step III improves the estimation accuracy and proposes a unified solution for integrating the speed and position estimation at standstill condition and running state. The feasibility of the proposed initial position estimation method has been investigated and validated with both simulation and experimental tests. The initial position can be identified within 50 milliseconds and the position estimation error is less than 1° electrical degree.

At running state, a nonlinear optimization based speed and position estimation algorithm has been presented. A cost function is defined which utilizes both speed and position as decision variables and the speed and position information can be obtained by minimizing the cost function. At low speed, the cost function is modified and extra high frequency voltage is injected but the position estimator structure remains the same. The modified cost function and the variable magnitudes injection are consistent with the method used in Step III of the proposed initial position estimation method. In this way, a unified speed and position estimator is proposed for IPM motor drives at wide speed range. The effectiveness of the cost functions has been validated with contour plots and convexity analysis at different speeds and positions. The real

time implementation of the proposed estimation observer has been introduced and the feasibility of the proposed method has been validated with the prototype IPM motor drive system. The convergence range, performance with different speed and torque transients have been presented. The experimental results demonstrate that the proposed method is capable of estimating the speed and position with high accuracy and fast dynamic performance.

In order to better evaluate the proposed estimation method, the proposed unified speed and position estimation method was compared with the reference combined estimation method on the same prototype IPMSM drives test bench. Under same test conditions, the proposed method outperforms with its excellent dynamic performance and steady state accuracy. Moreover, the cost functions defined in the proposed method is capable of dealing with different voltage injection types and nonlinear motor parameters, which make this method more flexible under different practical requirements. At last, the capability of estimating speed and position with low sampling frequency contributes in involving machine nonlinearity at running state estimation and demonstrates its potential in high power AC motor drive applications.

## 8.2 Future Work Suggested

Related research topics which can be further investigated in future developments are listed as follows:

1. Investigation on the speed and position estimation at running state by employing the cost function with nonlinear inductance profiles at low sampling frequency.

2. Investigation on the inverter nonlinearity compensation for improving the position estimation accuracy.

3. Investigation on the estimation performance with higher switching frequency.

4. Investigation on the convexity analysis of the cost functions and the sensorless control system stability.

5. Investigation on combining parameter estimation with position and speed estimation.

6. Investigation on forming an optimization over multiple sample times for integrating the filtering into the optimization formulation.

## 8.3 Publications

### 8.3.1 Journal Papers

**Yingguang Sun**, Matthias Preindl, Shahin Sirouspour and Ali Emadi, "Unified Wide-Speed Sensorless Scheme Using Nonlinear Optimization for IPMSM Drives," *IEEE Transactions on Power Electronics*, vol. PP, issue. 99, pp. 1-1, 2016.

**Yingguang Sun**, Matthias Preindl, Shahin Sirouspour and Ali Emadi, "Fast Initial Position Estimation Scheme Using Nonlinear Optimization for IPMSM Drives," submitted to *IEEE Journal of Emerging and Selected Topics in Power Electronics*.

### 8.3.2 Conference Papers

**Yingguang Sun**, Matthias Preindl, Shahin Sirouspour and Ali Emadi, "Nonlinear Modeling and Design of Initial Position Estimation and Polarity Detection of IPM drives," in *Conf. Rec. IEEE-IES (IECON'15) Annu. Meeting,* pp. 4059-4064, 2015.

# Bibliography

Aihara, T., Toba, A., Yanase, T., Mashimo, A., and Endo, K. (1999). Sensorless torque control of salient-pole synchronous motor at zero-speed operation. *IEEE Trans. Power Electron.*, **14**(1), 202–208.

Al-nabi, E., Wu, B., Zargari, N. R., and Sood, V. (2013). Sensorless control of CSC-Fed IPM machine for zero- and Low-Speed operation using pulsating hfi method. *IEEE Trans. Ind. Electron.*, **60**(5), 1711–1723.

Andreescu, G., Pitic, C. I., Blaabjerg, F., and Boldea, I. (2008). Combined flux observer with signal injection enhancement for wide speed range sensorless direct torque control of IPMSM drives. *IEEE Trans. Energy Convers.*, **23**(2), 393–402.

Antonello, R., Tinazzi, F., and Zigliotto, M. (2015). Benefits of direct phase voltage measurement in the rotor initial position detection for permanent-magnet motor drives. *IEEE Trans. Ind. Electron.*, **62**(11), 6719–6726.

Bianchi, N. and Bolognani, S. (1997). Parameter and volt-ampere ratings of a synchronous motor drive for flux-weakening applications. *IEEE Trans. Power Electron.*, **12**(5), 895–903.

Bilewski, M., Fratta, A., Giordano, L., Vagati, A., and Villata, F. (1993). Control

of high-performance interior permanent magnet synchronous drives. *IEEE Trans. Ind. Appl.*, **29**(2), 328–337.

Bilgin, B., Magne, P., Malysz, P., Yang, Y., Pantelic, V., Preindl, M., Korobkine, A., Jiang, W., Lawford, M., and Emadi, A. (2015). Making the case for electrified transportation. *IEEE Trans. Transport. Electrific.*, **1**(1), 4–17.

Bisheimer, G., Sonnaillon, M., DeAngelo, C., Solsona, J., and Garcia, G. (2010). Full speed range permanent magnet synchronous motor control without mechanical sensors. *IET Electr. Power Appl.*, **4**(1), 35–44.

Bolognani, S., Oboe, R., and Zigliotto, M. (1999). Sensorless full-digital PMSM drive with EKF estimation of speed and rotor position. *IEEE Trans. Ind. Electron.*, **46**(1), 184–191.

Bolognani, S., Calligaro, S., Petrella, R., and Tursini, M. (2011). Sensorless control of IPM motors in the low-speed range and at standstill by HF injection and DFT processing. *IEEE Trans. Ind. Appl.*, **47**(1), 96–104.

Bolognani, S., Faggion, A., Fornasiero, E., and Sgarbossa, L. (2012). Full speed range sensorless IPM motor drives. In *Conf. Rec. International Conference on Electrical Machines*, pages 2209–2215.

Boussak, M. (2005). Implementation and experimental investigation of sensorless speed control with initial rotor position estimation for interior permanent magnet synchronous motor drive. *IEEE Trans. Power Electron.*, **20**(6), 1413–1422.

Boyd, S. and Vandenberghe, L. (2004). *Convex Optimization*. Cambridge University Press, New York, NY. ISBN: 0-521-83378-7.

Byrd, D. (2014). Close-loop motor control: An introduction to rotary resolvers and encoders.

Chan, C. C. (2002). The state of the art of electric and hybrid vehicles. *Proceedings of the IEEE*, **90**(2), 247–275.

Chan, T., Wang, W., Borsje, P., Wong, Y., and Ho, S. (2008). Sensorless permanent-magnet synchronous motor drive using a reduced-order rotor flux observer. *IET Electr. Power Appl.*, **2**(2), 88–98.

Chen, Z., Tomita, M., Doki, S., and Okuma, S. (2003). An extended electromotive force model for sensorless control of interior permanent-magnet synchronous motors. *IEEE Trans. Ind. Electron.*, **50**(2), 288–295.

Cheng, B. and Tesch, T. R. (2010). Torque feedforward control technique for permanent-magnet synchronous motors. *IEEE Trans. Ind. Electron.*, **57**(3), 969–974.

Chi, S., Zhang, Z., and Xu, L. (2009). Sliding-mode sensorless control of direct-drive PM synchronous motors for washing machine applications. *IEEE Trans. Ind. Appl.*, **45**(2), 582–590.

Cintron-Rivera, J., Babel, A., Montalvo-Ortiz, E., Foster, E., and Strangas, E. (2012). A simplified characterization method including saturation effects for permanent magnet machines. In *Conf. Rec. International Conference on Electrical Machines (ICEM)*, pages 837–843.

Devices, A. (2000). Implementing space vector modulation with admcf32x.

Dorf, R. C. and Bishop, R. H. (2010). *Modern Control Systems*. Prentice Hall, Upper Saddle River, NJ. ISBN: 978-0-13-602458-3.

dSPACE (2014). MicroAutoBoxHardwareConcept_Release2014B.

dSPACE GmbH (2013). ProductBrochure_MicroAutoBox-HW_E_ebook.

El-Serafi, A. M., Abdallah, A. S., El-Sherbiny, M. K., and Badawy, E. H. (1988). Experimental study of the saturation and the cross-magnetizing phenomenon in saturated synchronous machines. *IEEE Trans. Energy Convers.*, **3**(4), 815–823.

EL-Sharkawi, M. A. (2000). *Fundamentals of Electric Drives*. Brooks/Cole Publishing Company, Pacific Grove, CA. ISBN: 0-534-95222-4.

Emadi, A. (2014). *Advanced Electric Drive Vehicles*. CRC Press, Boca Raton, FL. ISBN: 978-1-4665-9769-3.

Emadi, A., Lee, Y. J., and Rajashekara, K. (2008). Power electronics and motor drives in electric, hybrid electric, and plug-in hybrid electric vehicles. *IEEE Trans. Ind. Electron.*, **55**(6), 2237–2245.

Eull, M., Preindl, M., and Emadi, A. (2016). Analysis and design of a high efficiency, high power density three-phase silicon carbide inverter. In *Conf. Rec. IEEE Transportation Electrification Conference and Expo (ITEC)*, pages 1–6.

Europe, T. I. (1998). Field orientated control of 3-phase ac-motors.

Fahimi, B., Emadi, A., and Sepe, R. B. (2004). Position sensorless control. *IEEE Industry Applications Magazine*, **10**(1), 40–47.

Foo, G., Sayeef, S., and Rahman, M. F. (2010). Low-speed and standstill operation of a sensorless direct torque and flux controlled IPM synchronous motor drive. *IEEE Trans. Energy Convers.*, **25**(6), 25–33.

Genduso, F., Miceli, R., Rando, C., and Galluzzo, G. R. (2010). Back EMF sensorless-control algorithm for high-dynamic performance PMSM. *IEEE Trans. Ind. Electron.*, **57**(6), 2092–2100.

Gong, L. M. and Zhu, Z. Q. (2013). Robust initial rotor position estimation of permanent-magnet brushless AC machines with carrier-signal-injection-based sensorless control. *IEEE Trans. Ind. Appl.*, **49**(6), 2602–2609.

Guglielmi, P., Pastorelli, M., and Vagati, A. (2006). Cross-saturation effects in ipm motors and related impact on sensorless control. *IEEE Trans. Ind. Appl.*, **42**(6), 1516–1522.

Hart, D. W. (2010). *Power Electronics*. McGraw-Hill Education, Columbus, OH. ISBN: 978-0-07-338067-4.

Hasegawa, M. and Matsui, K. (2009). Position sensorless control for interior permanent magnet synchronous motor using adaptive flux observer with inductance identification. *IET Electr. Power Appl.*, **3**(3), 209–217.

Huang, Z., You, L., and Wang, Z. (2014). Sensorless initial rotor position identification for non-salient permanent magnet synchronous motors based on dynamic reluctance difference. *IET Power Electron.*, **7**(9), 2336–2346.

Hughes, A. (2006). *Electric Motor and Drives, Fundamentals, Types and Applications (Third Edition)*. Elsevier Ltd., Jordon Hill, Oxford. ISBN: 978-0-7506-4718-2.

Instruments, T. (2005). Low-voltage high-speed quadruple differential line receiver. [Online]. Available: http://www.ti.com/lit/ds/symlink/am26lv32.pdf.

Instruments, T. (2015). Technical reference manual of tms320f2837xd dual-core delfino microcontrollers. [Online]. Available: http://www.ti.com.cn/cn/lit/ug/spruhm8e/spruhm8e.pdf.

Jahns, T. M., Kliman, G. B., and Neumann, T. W. (1986). Interior permanent-magnet synchronous motors for adjustable-speed-drives. *IEEE Trans. Ind. Appl.*, **IA-22**(4), 738–747.

Jang, J., Ha, J., Ohto, M., Ide, K., and Sul, S. (2004). Analysis of permanent-magnet machine for sensorless control based on high-frequency signal injection. *IEEE Trans. Ind. Appl.*, **40**(6), 1595–1604.

Jeong, Y., Lorenz, R. D., Jahns, T. M., and Sul, S. (2005). Initial rotor position estimation of an interior permanent-magne synchronous machine using carrier-frequency injection methods. *IEEE Trans. Ind. Appl.*, **41**(1), 38–45.

Khlaief, A., Bendjedia, M., Boussak, M., and Gossa, M. (2012). A nonlinear observer for high-performance sensorless speed control of IPMSM drive. *IEEE Trans. Power Electron.*, **27**(6), 3028–3040.

Kim, H., Huh, K., Lorenz, R. D., and Jahns, T. M. (2004). A novel method for initial rotor position estimation for IPM synchronous machine drives. *IEEE Trans. Ind. Appl.*, **40**(5), 1369–1378.

Kim, S., Ha, J., and Sul, S. (2012). PWM switching frequency signal injection sensorless method in IPMSM. *IEEE Trans. Ind. Appl.*, **48**(5), 1576–1587.

Kim, Y. and Kook, Y. (1999). High performance IPMSM drives without rotational position sensors using reduced-order EKF. *IEEE Trans. Energy Convers.*, **14**(4), 868–873.

Kimbrell, J. (2013). Fundamentals of industrial encoder sensing technologies, motor detection theory and methods, and signal output styles.

Kondo, S., Takahashi, A., and Nishida, T. (1995). Armature current locus based estimation method of rotor position of permanent magnet synchronous motor without mechanical sensor. In *Conf. Rec. IEEE-IAS Annu. Meeting*, volume 1, pages 55–60.

Li, Y., Zhu, Z., Howe, D., Bingham, C. M., and Stone, D. A. (2009). Improved rotor-position estimation by signal injection in brushless ac motors, accounting for cross-coupling magnetic saturation. *IEEE Trans. Ind. Appl.*, **45**(5), 1843–1850.

Liu, J. M. and Zhu, Z. Q. (2014a). Improved sensorless control of permanent-magnet synchronous machine based on third-harmonic back EMF. *IEEE Trans. Ind. Appl.*, **50**(3), 1861–1870.

Liu, J. M. and Zhu, Z. Q. (2014b). Novel sensorless control strategy with injection of high-frequency pulsating carrier signal into stationary reference frame. *IEEE Trans. Ind. Appl.*, **50**(4), 2574–2583.

Luenberger, D. G. and Ye, Y. (2008). *Linear and Nonlinear Programming*. Springer, New York, NY. ISBN: 978-0-387-74502-2.

Ma, Z., Gao, J., and Kennel, R. (2013). FPGA implementation of a hybrid sensorless control of SMPMSM in the whole speed range. *IEEE Trans. Ind. Informat.*, **9**(3), 1253–1261.

Morimoto, S., Takeda, Y., Hirasa, T., and Taniguchi, K. (1990). Expansion of operating limits for permanent magnet motor by current vector control considering inverter capacity. *IEEE Trans. Ind. Appl.*, **26**(5), 866–871.

Morimoto, S., Kawamoto, K., Sanada, M., and Takeda, Y. (2002). Sensorless control strategy for salient-pole PMSM based on extended EMF in rotating reference frame. *IEEE Trans. Ind. Appl.*, **38**(4), 1054–1061.

Murakami, S., Shiota, T., Ohto, M., Ide, K., and Hisatsune, M. (2012). Encoderless servo drive with adequately designed IPMSM for pulse-voltage-injection-based position detection. *IEEE Trans. Ind. Appl.*, **48**(6), 1922–1930.

Nahid-Mobarakeh, B., Meibody-Tabar, F., and Sargos, F.-M. (2004). Mechanical sensorless control of PMSM with online estimation of stator resistance. *IEEE Trans. Ind. Appl.*, **40**(2), 457–471.

Nahid-Mobarakeh, B., Meibody-Tabar, F., and Sargos, F.-M. (2007). Back EMF estimation-based sensorless control of PMSM: Robustness with respect to measurement errors and inverter irregularities. *IEEE Trans. Ind. Appl.*, **43**(2), 485–494.

Nakashima, S., Inagaki, Y., and Miki, I. (2000). Sensorless initial rotor position estimation of surface permanent-magnet synchronous motor. *IEEE Trans. Ind. Appl.*, **36**(6), 1598–1603.

Nalakath, S., Preindl, M., Bilgin, B., Cheng, B., and Emadi, A. (2015). Modeling and analysis of AC resistance of a permanent magnet machine for online estimation purposes. In *Conf. Rec. 2015 IEEE Energy Conversion Congress and Exposition (ECCE)*, pages 5682–5688.

Noguchi, T., Yamada, K., Kondo, S., and Takahashi, I. (1998). Initial rotor position estimation method of sensorless PM synchronous motor with no sensitivity to armature resistance. *IEEE Trans. Ind. Electron.*, **45**(1), 118–125.

Park, N. and Kim, S. (2014). Simple sensorless algorithm for interior permanent magnet synchronous motors based on high-frequency voltage injection method. *IET Electr. Power Appl.*, **8**(2), 68–75.

Petrovic, V., Stankovic, A. M., and Blasko, V. (2003). Position estimation in salient PM synchronous motors based on PWM excitation transients. *IEEE Trans. Ind. Appl.*, **39**(3), 835–843.

Preindl, M. (2013). *Novel Model Predictive Control of a PM Synchronous Motor Drive*. Ph.D. thesis, Univ. of Padua.

Preindl, M. and Bolognani, S. (2012). Model predictive direct speed control with finite control set of pmsm drive systems. *IEEE Trans. Power Electron.*, **28**(2), 1007–1015.

Quang, N. P. and Dittrich, J.-A. (2008). *Vector Control of Three-Phase AC Machines, System Development in the Practice*. Springer-Verlag Berlin Heidelberg, Heidelberg, Berlin. ISBN: 978-3-540-79028-0.

Schroedl, M. (1996). Sensorless control of AC machines at low speed and standstill based on the "INFORM" method. In *Conf. Rec. IEEE IAS Annu. Meeting*, volume 1, pages 270–277.

Sensors, B. (2015). Datasheet of dho5 fixed resolution incremental encoder.

[Online]. Available: http://www.beisensors.com/pdfs/dho5-optical-incremental-encoder_en.pdf.

Shinnaka, S. (2006). New sensorless vector control using minimum-order flux state observer in a stationary reference frame for permanent-magnet synchronous motors. *IEEE Trans. Ind. Electron.*, **53**(2), 388–398.

Shirabe, K., Swamy, M. M., Kang, J. K., Hisatsune, M., Wu, Y., Kebort, D., and Honea, J. (2014). Efficiency comparison between Si-IGBT-Based drive and GaN-Based drive. *IEEE Trans. Ind. Appl.*, **50**(1), 556–572.

Silva, C., Asher, G. M., and Sumner, M. (2006). Hybrid rotor position observer for wide speed-range sensorless PM motor drives including zero speed. *IEEE Trans. Ind. Electron.*, **53**(2), 373–378.

Sun, Y., Preindl, M., Sirouspour, S., and Emadi, A. (2015). Nonlinear modeling and design of initial position estimation and polarity detection of IPM drives. In *Conf. Rec. IEEE-IES (IECON'15) Annu. Meeting*, pages 4059–4064.

Sun, Y., Preindl, M., Sirouspour, S., and Emadi, A. (2016). Unified wide-speed sensorless scheme using nonlinear optimization for IPMSM drives. *IEEE Trans. Power Electron.*, **PP**(99), 1–1.

Szymczak, J., O'Meara, S., Gealon, J. S., and Rama, C. N. D. L. (2014). Precision resolver to digital converter measures angular position and velocity.

Tamagawa (2014). Datasheet of VR type resolver. [Online]. Available: http://www.tamagawa-seiki.com/pdf/download/1570n13ej_shusei.pdf.

Tursini, M., Petrella, R., and Parasiliti, F. (2003). Initial rotor position estimation method for PM motors. *IEEE Trans. Ind. Appl.*, **39**(6), 1630–1640.

Uddin, M. N., Radwan, T. S., and Rahman, M. A. (2002). Performance of interior permanent magnet motor drive over wide speed range. *IEEE Trans. Energy Convers.*, **17**(1), 79–84.

Štumberger, B., Štumberger, G., Dolinar, D., Hamler, A., and Trlep, M. (2003). Evaluation of saturation and cross-saturation effects in interior permanent-magnet synchronous motor. *IEEE Trans. Ind. Appl.*, **39**(5), 1264–1271.

Waide, P. and Brunner, C. U. (2011). Energy-efficiency policy opportunities for electric motor-driven systems.

Wang, G., Yang, R., and Xu, D. (2013a). DSP-based control of sensorless IPMSM drives for wide-speed-range operation. *IEEE Trans. Ind. Electron.*, **60**(2), 720–727.

Wang, G., Li, Z., Zhang, G., Yu, Y., and Xiu, D. (2013b). Quadrature pll-based high-order sliding-mode observer for IPMSM sensorless control with online MTPA control strategy. *IEEE Trans. Energy Convers.*, **28**(1), 214–224.

Wang, G., Zhan, H., Zhang, G., Gui, X., and Xiu, D. (2014). Adaptive compensation method of position estimation harmonic error for EMF-based observer in sensorless IPMSM drives. *IEEE Trans. Power Electron.*, **29**(6), 3055–3064.

XENERGY, I. (1998). United States industrial electric motor systems market opportunities assessment.

Xie, G. and Ramshaw, R. S. (1986). Nonlinear model of synchronous machines with saliency. *IEEE Trans. Energy Convers.*, **EC-1**(3), 198–204.

Yang, S. (2015). Saliency-based position estimation of permanent-magnet synchronous machines using square-wave voltage injection with a single current sensor. *IEEE Trans. Ind. Appl.*, **51**(2), 1561–1571.

YASKAWA (2014). YASKAWA AC Drive-A1000 high performance vector control drive technical manual.

Yoon, Y., Sul, S., Morimoto, S., and Ide, K. (2011). High-bandwidth sensorless algorithm for AC machines based on square-wave-type voltage injection. *IEEE Trans. Ind. Appl.*, **47**(3), 1361–1370.

Zaim, S., Nahid-Mobarakeh, B., and Meibody-Tabar, F. (2014). Robust position sensorless control of nonsalient PMSM at standstill and low speed. *IEEE Trans. Emerg. Sel. Topics Power Electron.*, **2**(3), 640–650.

Zhang, Z., Wang, F., Tolbert, L. M., Blalock, B., and Costinett, D. J. (2015). Evaluation of switching performance of SiC devices in PWM Iverter-Fed induction motor drives. *IEEE Trans. Power Electron.*, **30**(10), 5701–5711.

Zhao, Y., Qiao, W., and Wu, L. (2013). An adaptive Quasi-Sliding-Mode rotor position observer-based sensorless control for interior permanent magnet synchronous machines. *IEEE Trans. Ind. Electron.*, **28**(12), 5618–5629.

Zhao, Y., Qiao, W., and Wu, L. (2015a). Dead-time effect analysis and compensation for a sliding-mode position observer-based sensorless IPMSM control system. *IEEE Trans. Ind. Appl.*, **51**(3), 2528–2535.

Zhao, Y., Zhang, Z., Qiao, W., and Wu, L. (2015b). An extended flux Model-Based

rotor position estimation for sensorless control of salient-pole permanent-magnet synchronous machines. *IEEE Trans. Power Electron.*, **30**(8), 4412–4422.

Zhu, Z. Q. and Gong, L. M. (2011). Investigation of effectiveness of sensorless operation in carrier-signal-injection-based sensorless-control methods. *IEEE Trans. Ind. Electron.*, **58**(8), 3431–3439.